Evolution of the volatile inventory of rocky exoplanets in a runaway greenhouse state with the General Circulation Model ExoFMS-SOCRATES

Ryan Boukrouche

Hertford College

University of Oxford

A thesis presented for the degree of

Doctor of Philosophy

Michaelmas 2022

I dedicate this piece to my brilliant mentors,
my parents, wing-givers, ever higher they guide,
to my younger self, wonder-filled and doomed to glide,
to my older self, shadow-veiled beacon of light,
may they all persevere and learn forevermore.

ὑπ᾽ ἀσθενείας καὶ βραδυτῆτος οὐχ οἵους τε εἶναι ἡμᾶς διεξελθεῖν ἐπ᾽ ἔσχατον τὸν ἀέρα: ἐπεί, εἴ τις αὐτοῦ ἐπ᾽ ἄκρα ἔλθοι ἢ πτηνὸς γενόμενος ἀνάπτοιτο, κατιδεῖν ἂν ἀνακύψαντα, ὥσπερ ἐνθάδε οἱ ἐκ τῆς θαλάττης ἰχθύες ἀνακύπτοντες ὁρῶσι τὰ ἐνθάδε, οὕτως ἄν τινα καὶ τὰ ἐκεῖ κατιδεῖν, καὶ εἰ ἡ φύσις ἱκανὴ εἴη ἀνασχέσθαι θεωροῦσα, γνῶναι ἂν ὅτι ἐκεῖνός ἐστιν ὁ ἀληθῶς οὐρανὸς καὶ τὸ ἀληθινὸν φῶς καὶ ἡ ὡς ἀληθῶς γῆ.

By reason of feebleness and sluggishness, we are unable to attain to the upper surface of the air; for if anyone should come to the top of the air or should get wings and fly up, he could lift his head above it and see, as fishes lift their heads out of the water and see the things in our world, so he would see things in that upper world; and, if his nature were strong enough to bear the sight, he would recognize that that is the real heaven and the real light and the real earth.

— Socrates

As recorded in Phaedo 109e-110a (Plato, 360 B.C.E.)

Acknowledgements

I would like to express a deep gratitude to the following people that made the completion of this thesis possible.

Prof. Raymond T. Pierrehumbert, for being the most illuminating, supportive, encouraging, and patient supervisor.

My father, mother, and brother, for always supporting me and wishing for me to spend six months of holidays per year at home.

Dr. Tim Lichtenberg, for spontaneously acting as a second supervisor when he did not have to, with more time on his hands than my actual supervisor, time that I shamelessly took advantage of.

Dr. Mark Hammond, for helping me out of many a deep and treacherous chasm of coding darkness.

Dr. Elspeth K. H. Lee, for generously lending me her scary expertise on all things radiative.

Dr. James Manners and Dr. David S. Amundsen, for their invaluable help with the sibylline inner workings of the SOCRATES model.

Dr. Xianyu Tan, for all his insights on the wetter aspects of atmospheric physics.

Dr. Maxence Lefevre, for his help on the cloudier aspects of atmospheric physics.

Hamish Innes, for starting his work on the Exo-FMS model earlier than I did so that I could ask him about it or wonder at its capriciousness — and sometimes, sentience — alongside him.

Katherine I. Dale, for making the COVID-19 pandemic much more bearable than it should have been.

Kyra E. T. Schulman, for uncountable, fascinating, and unending discussions that kept me from being too focused on my real work.

Declaration

I, Ryan Boukrouche, declare that this thesis has been composed solely by myself and that it has not been submitted, in whole or in part, in any previous application for a degree. Except where stated otherwise by reference or acknowledgment, the work presented is entirely my own. Parts of this work have been published in Boukrouche, Lichtenberg, and Pierrehumbert (2021).

10/12/2022

Signature

Date

Abstract

The runaway greenhouse represents the ultimate climate catastrophe for rocky, Earth-like worlds: when the incoming stellar flux cannot be balanced by radiation to space, the oceans evaporate and exacerbate heating, turning the planet into a hot wasteland with a steam atmosphere overlying a possibly molten magma surface. The equilibrium state beyond the runaway greenhouse instellation limit depends on the radiative properties of the atmosphere and its temperature structure. Here, we use 1-D and 3-D radiative-convective models of steam atmospheres to explore the transition from the tropospheric radiation limit to the post-runaway climate state. To facilitate simulations with 3-D global circulation models, a computationally efficient band-grey model is developed, which is capable of reproducing the key features of the more comprehensive calculations. We analyse two factors that determine the equilibrated surface temperature of post-runaway planets. The infrared cooling of the planet is strongly enhanced by the penetration of the dry adiabat into the optically thin upper regions of the atmosphere. In addition, thermal emission of both shortwave and near-IR fluxes from the hot lower atmospheric layers, which can radiate through window regions of the spectrum, is quantified. 3-D GCM simulations were performed, indicating that the runaway greenhouse effect necessarily ends with a thin condensing region located at the uppermost layers of the atmosphere, mostly on the nightside, while dayside condensation is prevented by heating coming from the absorption of incoming stellar radiation caused by the opacity of water vapour. Surface pressures higher than 10 bar feature non-convective regions in the deep layers, whereas the surface temperature of post-runaway atmospheres seem only weakly sensitive to instellation. Combining five secondary eclipse observations of TRAPPIST-1b with JWST/MIRI could yield a 4.5σ detection if it has an atmosphere made out of 1 bar of water vapour. The maximum confidence level in the cases explored for TRAPPIST-1d is 2σ, making it unsuitable for thermal emission observations with JWST. Astronomical surveys of rocky exoplanets in the runaway greenhouse state may discriminate some of these features using multi-wavelength observations. Further understanding of runaway greenhouse climates will come from more holistic models, more spectroscopic measurements outside Earth-like conditions, and future observatories.

Keywords— extrasolar rocky planets - exoplanet atmospheres - greenhouse gases - habitable planets

Table of Contents

List of Figures

List of Tables

List of Abbreviations

ARIEL	Atmospheric Remote-sensing Infrared Exoplanet Large-survey
ASR	Absorbed Stellar Radiation
$\mathcal{CF}_F$	Flux Contribution Function
ESPRESSO	Echelle SPectrograph for Rocky Exoplanets and Stable Spectroscopic Observations
GCM	Global Climate Model
ISR	Incoming Stellar Radiation
JWST	James Webb Space Telescope
MIRI	Mid-Infrared Instrument
MT_CKD	Mlawer, Tobin, Clough, Kneizys, Davies
NIR	Near InfraRed
NIST	National Institute of Standards and Technology
OLR	Outgoing Longwave Radiation
OPR	Outgoing Planetary Radiation
OSR	Outgoing Shortwave Radiation
PLATO	PLAnetary Transits and Oscillations of stars
SOCRATES	Suite Of Community RAdiative Transfer codes based on Edwards and Slingo
$\mathcal{SCF}_F$	Surface Flux Contribution Function

UV	UltraViolet
WTG	Weak Temperature Gradient

1 | Introduction

1.1 Motivation

Water-rich rocky planets within the inner edge of their habitable zones are expected to undergo extreme, 'runaway' greenhouse effects (Ingersoll, 1969; Kasting, Whitmire, & Reynolds, 1993; Simpson, 1927) that force their climate into a transient hothouse state culminating into a hot, uninhabitable, and desiccated surface. The transition from this transient runaway greenhouse effect to a post-runaway state involves many radiative and convective processes that have major implications for their present-day climate, atmospheric composition, and observable features. The habitability prospects of this post-runaway state are also dependent on factors including the initial water inventory of the planet. The more water the planet has accreted and stored in its surface reservoir, the more vulnerable its habitability will be, due to the powerful greenhouse effect of water vapour. Could a planet recondense its water vapour into surface water oceans before losing it all to space? This is an open question that depends on many factors. The question of whether the Earth is susceptible to a moist greenhouse or runaway greenhouse climate transition has also been studied (Goldblatt, Robinson, Zahnle, & Crisp, 2013; Ramirez, Kopparapu, Lindner, & Kasting, 2014); however the answer is still unclear, partly due to the same processes that make climate change on Earth difficult to predict, clouds chief among them.

Although early discoveries were limited to giant planets, an increasingly large number of exoplanets closer to the mass and radius of the Earth are being discovered by various methods as shown on Figure 1.1. We are currently still biased towards planets with small orbital periods, large radii, and warmer than the Earth, however future space and ground-based observatories will soon be able to focus their target list on Earth-like planets around Sun-like stars.

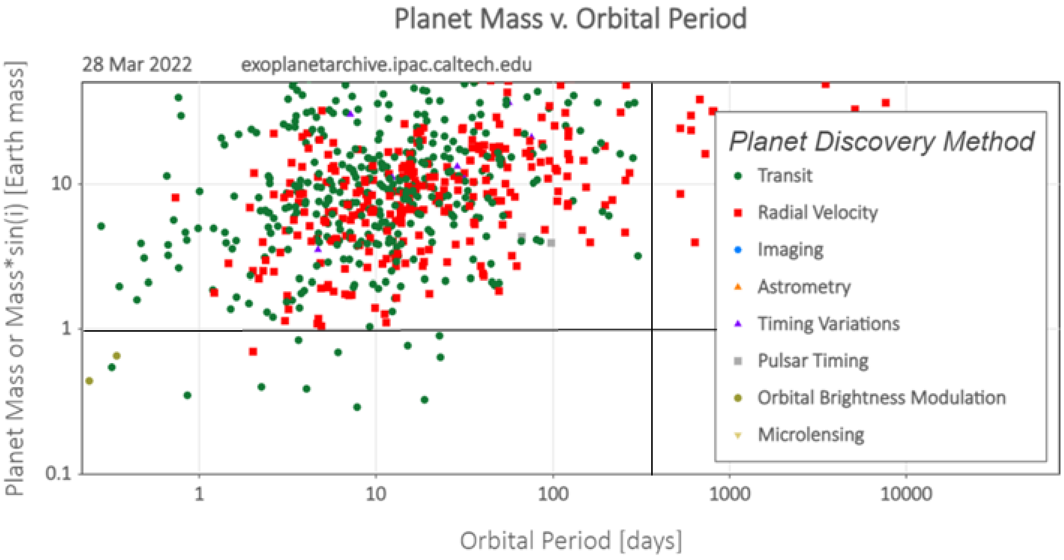

Figure 1.1: Planet mass as a function of orbital period for confirmed detections between 0.1 and 50 Earth masses. Earth is located at the intersection of the black lines.

The James Webb Space Telescope launched on December 25$^{\text{th}}$ 2021 was the start of this new era of astronomy. Its first observing cycle includes super-Earths (Brandeker et al., 2021) and terrestrial planets (Kreidberg et al., 2021; Rathcke et al., 2021). Future observatories will allow us to directly characterize Earth-like exoplanets around Sun-like stars. LIFE (Quanz et al., 2021b) is a candidate mission in the Voyage 2050 long-term plan in the ESA Science Programme which will use nulling interferometry to spatially resolve such exoplanets in the mid-infrared and discriminate their light from that of their host stars. The mission partly derived from the LUVOIR concept (Large Ultraviolet Optical Infrared Surveyor, Team et al. (2019)), if it does not deviate drastically from its original design, will be sensitive to a larger spectral range from the near-infrared to the far-ultraviolet, which will allow a much higher diagnostic power than narrower spectral ranges, especially for hotter planets (Boukrouche et al., 2021). The ESO ELT (Extremely Large Telescope, Ramsay et al. (2020)) will further push the bounds of spectral and spatial resolutions that we can reach and allow us to directly image Earth-like exoplanets at larger orbital periods. This continuing progress with regard to our observing capabilities is bringing Earth-sized rocky planets beyond the runaway greenhouse instellation threshold within our characterisability range, which further motivates theoretical studies as precursor science for these missions.

1.2 Aim and Objectives

This thesis has four main goals:

- To develop and validate the SOCRATES real-gas radiative transfer model for use in runaway and post-runaway climate calculations.
- To develop a computationally efficient band-grey model suitable for rapid calculations with three dimensional global circulation models (GCMs), and evaluate the extent to which it reproduces the key features of the SOCRATES calculations and other comprehensive radiative calculations that have appeared in the literature.
- To better elucidate the factors that allow a planet that has undergone a runaway greenhouse to eventually increase its radiative cooling to space, thus reaching a new equilibrium surface temperature, and to determine the dependence of the post-runaway temperature on the initial water inventory.
- To explore the climate dynamics of runaway atmospheres in three dimensions with the GCM Exo-FMS coupled with band-grey radiation, and estimate their observability prospects.

1.3 Thesis Outline

The remainder of this thesis is organised as follows:

Chapter 2 — This chapter goes over the current state of knowledge about the runaway greenhouse effect and its implications for the climate of planets.

Chapter 3 — This chapter explains the theoretical basis for the radiative-convective framework used in the modelling.

Chapter 4 — This chapter goes over the model development work that went into the band-grey model and SOCRATES.

Chapter 5 — This chapter presents the results from the one-dimensional work.

Chapter 6 — This chapter discusses the results presented in the previous chapter.

Chapter 7 — This chapter goes over the model development work that went into Exo-FMS, the coupling of the band-grey model, and the setup used in the simulations.

Chapter 8 — This chapter presents and discusses the results from the three-dimensional work.

Chapter 9 — This chapter brings the results from the previous chapters together.

2 | Review of the runaway greenhouse climate state

The temperate orbital region where liquid water can be stable on the surfaces of rocky exoplanets, often referred to as the habitable zone, is bounded starward by the runaway greenhouse limit (Kasting et al., 1993). It defines an orbit inside which a terrestrial planet harbouring a secondary atmosphere and a reservoir of water can fall into a positive feedback loop and lose its ability to sustain habitable surface conditions (Kopparapu et al., 2013). When the instellation exceeds levels at which the planetary climate can radiatively equilibrate, the available condensed water present at the surface evaporates into the atmosphere. This addition of water vapour to the increasingly steam-dominated atmosphere drives a positive feedback loop that warms the planet and accelerates the evaporation process until all available surface water is exhausted in the post-runaway state.

Planets undergoing a runaway greenhouse effect reach surface temperatures well in excess of those that Venus and Mercury experience in our Solar System today. Mercury, with its tenuous exosphere, reaches about $740\ \mathrm{K}$ on its dayside. Venus, with its dense atmosphere, maintains an average surface temperature of $737\ \mathrm{K}$. Venus's orbit is within the runaway greenhouse instellation threshold. This, coupled to the fact that Venus is considered to be the closest analog to Earth that we have in our solar system, makes it the archetypal case study for the runaway greenhouse effect and its consequences on climate evolution. One of the main evolutionary scenarios proposed is that it went through a moist and/or runaway greenhouse phase early in its history (Goldblatt et al., 2013; Kasting, 1988; Leconte, Forget, Charnay, Wordsworth, & Pottier, 2013), which would explain the absence of water and the massive CO_2 atmosphere observed today. Recent work by Way and Del Genio (2020) suggests that habitable conditions could have been maintained by the cloud albedo effect (Yang & Abbot, 2014) until planetary-scale volcanic events turned the climate into a hothouse. Further investigations by Turbet et al. (2021) shed doubt on this hypothesis, and suggested that the stellar fluxes at Venus's orbit and heating by water vapour absorption were enough to prevent condensation of water and thus cloud formation on the dayside, which would imply that Venus could not have benefited from a cloud shielding effect that would have allowed for stable surface water oceans. Indeed, another hypothesis suggests that Venus could instead have been desiccated right after formation by the presence of a long-lived magma ocean that stayed melted for around 100 Myr (Hamano, Abe, & Genda, 2013).

These pathways largely depend on the initial volatile inventory and their redistribution and loss throughout the planet's history. However, a planet that did undergo a runaway greenhouse effect with an Earth-like reservoir of water would in principle be able to keep its surface temperature up indefinitely until the water is completely lost to space. Runaway greenhouse theory indicates that the outgoing radiation fails to increase with increasing surface temperature until some threshold value, beyond which it increases drastically. What determines this threshold? One well-known mechanism is for the surface to become hot enough to start radiating to space directly through the window regions of the steam atmosphere. However, another mechanism that can increase the outgoing heat flux, less widely appreciated, is the penetration of the dry adiabat into the optically thin upper layers, which allows the planet to also radiate outside the window regions.

From a more general perspective, the observational bias toward extrasolar planets on close-in orbits implies that most detected rock-dominated exoplanets, such as super-Earths, are likely to reside within the instellation threshold of the runaway greenhouse (Jontof-Hutter, 2019). Such planets differ from temperate rocky planets in a variety of ways. Given a large enough water reservoir, the runaway greenhouse effect can inflate the atmosphere such that the increased radius would be indistinguishable from that of a planet with a larger radius free of a runaway state (Turbet, Ehrenreich, Lovis, Bolmont, & Fauchez, 2019). This inflation is caused by the additional water vapour relative to a temperate climate, which renders the atmosphere more opaque, raises the level of the infrared photosphere, cloud top, and overall scale height. The transit radii of runaway greenhouse planets can be further degenerate because of the different densities of molten versus solid rock (Bower et al., 2019). From an evolutionary perspective, long-term runaway greenhouse states can desiccate the planet via H_2O photolysis in the upper atmosphere and subsequent hydrogen escape (Kasting, 1988; Luger & Barnes, 2015; Schaefer, Wordsworth, Berta-Thompson, & Sasselov, 2016; Wordsworth & Pierrehumbert, 2013) and substantially alter the planetary composition inherited from formation. The planetary radius can thus serve as a crucial indicator of possible surface environments, allowing for the determination of the steady-state surface temperature, the shape of the transmission spectrum of the atmosphere, or how much volatile content can be left in the planet's inventory above and below the surface.

In order to test theoretical predictions for rocky planets on both sides of the runaway greenhouse limit, astronomical surveys may allow for more accurate diagnoses of possible climate states and compositions of rock-dominated exoplanets and their atmospheres. To do so, measurements from indirect surveys with instruments such as PLATO (Rauer et al., 2014), ARIEL (Tinetti et al., 2018) and JWST (Beichman et al., 2019) to measure radii, and ESPRESSO (Pepe et al., 2014) or SPIRou (Artigau et al., 2014) to obtain mass measurements, or direct imaging techniques (Quanz et al., 2021b, 2021a), need to be combined and compared to theoretical models.

In particular, the emission spectrum of the atmosphere and its radiating layer have a significant impact on long-term climate evolution and on potentially diagnostic characteristics of the atmospheric structure. Previous studies (Katyal et al., 2020; Lichtenberg et al., 2021; Marcq, Salvador, Massol, & Davaille, 2017; Schaefer et al., 2016) investigated how a runaway greenhouse effect can affect the spectral signature of the atmosphere.

3 | Theory of convection and radiation

3.1 Dry convection

When modelling a tropospheric profile, certain assumptions are usually made unless the context of the study prescribes the inclusion of more comprehensive physics. One such assumption is that the atmosphere only contains ideal gases, such that pressure and temperature are easily accessible from one another through the ideal gas law. This leads to a simple relationship between the two that neglects any form of radiative exchange except through vertical motion of parcels - dry convection. With vigorous mixing by convection, mixing time is generally considered to be short compared to the timescale of radiative transfer. This results in an adiabatic lapse rate that is simple for non-condensing ideal gases.

Deriving the dry adiabatic lapse rate using the ideal gas and isentropic assumptions is straightforward, yet central to understanding the physics at work. Let us simply start with the enthalpic version of the First Law of Thermodynamics,

$$dh = pds + vdp, \tag{3.1}$$

with h, s, v, and p the specific enthalpy, entropy, volume, and pressure variables, respectively. An adiabatic and reversible process is isentropic, yielding $ds = 0$ and

$$dh = vdp \Rightarrow dp = \frac{dh}{v} \tag{3.2}$$

Using the ideal gas assumption here, we get

$$pv = RT \Rightarrow v = \frac{RT}{p}. \tag{3.3}$$

Replacing v and $dh = c_p dT$ in the First Law,

$$dp = \frac{pc_p dT}{RT} \Rightarrow \frac{dp}{p} = \frac{c_p}{R}\frac{dT}{T}. \tag{3.4}$$

Notice that in the z coordinate we had

$$\Gamma_d = -\frac{dT}{dz} = \frac{g}{c_p}. \tag{3.5}$$

This is the dry adiabatic lapse rate in z. We just found that in p, we have instead

$$\frac{dT}{dp} = \frac{R}{c_p}\frac{T}{p}. \tag{3.6}$$

Integrating now between the points (T_0,p_0) and (T_1,p_1),

$$\int_{T_0}^{T_1} \frac{dT}{T_1} = \frac{R}{c_p}\int_{p_0}^{p_1} \frac{dp}{p_1} \Rightarrow \ln\left(\frac{T_1}{T_0}\right) = \frac{R}{c_p}\ln\left(\frac{p_1}{p_0}\right) \Rightarrow \frac{T_1}{T_0} = \left(\frac{p_1}{p_0}\right)^{\frac{R}{c_p}}. \tag{3.7}$$

The expression used for the dry adiabat is therefore

$$T_1 = T_0\left(\frac{p_1}{p_0}\right)^{\frac{R}{c_p}}. \tag{3.8}$$

A well-mixed dry troposphere will tend to relax toward constant potential temperature $\theta = T\left(\frac{p}{p_0}\right)^{-\frac{R}{c_p}}$, which is satisfied by Eq. 3.8.

Although this expression yields the equilibrium state of such a troposphere, an atmosphere might also feature a stratosphere and a boundary layer, which are affected by other processes besides dry convection. The boundary layer might account for surface drag, sensible heat, or internal fluxes, while the stratosphere has next to no convective heat transport and incoming stellar radiation can play a role in determining its depth and position. These effects can be accounted for with forward-marched time stepping, and the initial state of the atmosphere might be an isothermal profile, the dry adiabat derived above, or other customized initialisations.

Time stepping can be done with iterative numerical adjustments. Looping over the vertical levels, we check whether the local temperature follows the dry adiabat. If this condition is realized, the temperature of a given layer is equal to that of the layer below multiplied by $\left(\frac{p_i}{p_{i+1}}\right)^{\frac{R}{c_p}}$, if p_i and p_{i+1} are the pressures of the above and below levels respectively. If the temperature T_i is lower than that for instance, the slope of the profile is steeper than that of the dry adiabat and needs to be adjusted. While the slope is determined by the adiabat, the intercept is determined by the requirement that dry enthalpy must be conserved along the column. The conserved quantity is then the dry enthalpy integrated over the pressure levels,

$$H_{dry} = \int_0^{p_s} c_p T \frac{dp}{g}, \tag{3.9}$$

with p_s the surface pressure, c_p the isobaric heat capacity, and g the surface gravity. This form is only valid if c_p is constant with temperature, though variations can easily be incorporated through minor modifications to the weighting.

We use the pressure thicknesses of layers i and $i+1$, dp_i and dp_{i+1}, as well as the barycenter $T_{\rm bar} = T_i \frac{dp_i}{dp_{i+1}} + T_{i+1} \frac{dp_{i+1}}{dp_i + dp_{i+1}}$ to adjust the temperature of the layer $i+1$ with

$$T_{i+1} = \frac{T_{\rm bar}(dp_i + dp_{i+1})}{dp_i \left(\frac{p_i}{p_{i+1}}\right)^{\frac{R}{cp}} + dp_{i+1}}. \tag{3.10}$$

Then, we adjust in turn the temperature of the layer i with $T_i = T_{i+1} \left(\frac{p_i}{p_{i+1}}\right)^{\frac{R}{cp}}$.

This algorithm is typically applied both upward and downward throughout the column and several times per timestep, in order to ensure stability after each timestep is complete.

3.2 Moist convection

Moist convection needs to be accounted for whenever one of the components of the atmosphere becomes condensible. The effect of condensation on temperature is especially important near the radiating levels, at pressures where the optical depth of the atmosphere is unity. When this happens, the condensible introduces latent heat of condensation and evaporation that changes the thermal structure of the atmosphere. The chemical composition of the atmosphere determines how straightforward this accounting will be. On Earth, the main condensible component is water vapour. Its mixing ratio at the surface varies from 0.01-0.02$\%$ beyond the polar circles where dew point temperatures reach about 230 K, to about 4$\%$ in the tropics when dew point temperatures are closer to 295 K. This dew point temperature is the temperature to which a parcel of air has to be reduced in order to become saturated with water vapour. It can be measured with a hygrometer, an instrument that measures the temperature of air passing over it while being progressively cooled until it detects dew forming on it. The temperature measured at that moment is the dew point temperature. Alternatively, we can calculate the dew point of any substance if we know the local air pressure and the latent heat of condensation of the substance. In planetary atmospheres with one or several condensible components, the knowledge of this dew point temperature is critical, because it can have a significant impact on the thermal structure of the atmosphere and on the radiative budget of the planet.

A moist lapse rate can be pseudoadiabatic, meaning that any condensates formed during condensation are instantaneously removed from the atmosphere in an irreversible manner. It comes down to assuming that precipitation is instantaneous and has a one hundred percent efficiency. If precipitation is an important part of the modelling, it needs to be tracked during time stepping using a reversible, adiabatic lapse rate. The general moist pseudoadiabatic lapse rate formula with background non-condensible components is

$$\frac{d\mathrm{ln}p}{d\mathrm{ln}T} = \frac{p_{\mathrm{sat}}}{p}\frac{L(T)}{R_c T} + \frac{p_a}{p}\frac{c_{pa}}{R_a}\frac{1+\left(\frac{c_{pc}}{c_{pa}}+\left(\frac{L}{R_c T}-1\right)\frac{L}{c_{pa}T}\right)r_{\mathrm{sat}}}{1+\frac{L}{R_a T}r_{\mathrm{sat}}}, \tag{3.11}$$

with p_{sat} the saturation vapour pressure, R the specific gas constant, c_p the specific heat capacity at constant pressure, r_{sat} the saturation mass mixing ratio, a the subscript for the background mix of non-condensible gases, and c the subscript for the condensible gases (Ding & Pierrehumbert, 2016).

Many models use pressure coordinates in place of height coordinates, including the ones used in this thesis. If the temperature is high enough so that $r_{\mathrm{sat}} >> 1$, then $p_{\mathrm{sat}} - p \to 0$ and $\frac{p_a}{p} \to 0$, and the formula reduces to the Clausius-Clapeyron relation,

$$T_{dew}(P) = \frac{T_b}{1 - \frac{RT_b}{L}\ln\left(\frac{P}{P_b}\right)}. \tag{3.12}$$

This is the moist pseudo-adiabat formula for a single-component atmosphere. (T_b,P_b) is the boiling point, which can also be any point on the same coexistence curve. A derivation of this formula can for instance be found in Vallis (2017).

For such a single-component atmosphere, moist convection can be carried out by simply adjusting the temperature profile to the lapse rate described by Equation 3.12. While this is referred to as a kind of moist convective adjustment, for a pure steam atmosphere there isn't actually any need to account for buoyancy generation or convection in the normal sense unlike in the dry convection scheme; rather, the supposition alone that the atmosphere is saturated is enough to determine the temperature profile, regardless of whether this saturation is maintained by convection due to vertical motion or radiative cooling. The same scheme works for any single-component condensible atmosphere, for instance a condensing pure CO_2 atmosphere, as may be common toward the outer edge of the habitable zone (Ding & Pierrehumbert, 2016).

If there isn't any condensed reservoir at the surface, $P_b < P_{sat}(T_s)$. A parcel of air lifted from the surface follows the dry adiabat derived in Sect. 3.1, $T_{dry}(P) = T_a\left(\frac{P}{P_a}\right)^{\frac{R}{c_p}}$ until it reaches a pressure P_{LCL} where $T_{dry}(P) = T_{dew}(P)$ whereafter condensation starts and the parcel follows the single-component moist pseudo-adiabat $T_{dew}(P)$.

This expression relies on three main simplifications from the general form $\frac{P}{T} = \frac{L}{T\Delta v}$, where $L = L(T)$ and Δv is the difference between the specific volumes of the two phases.

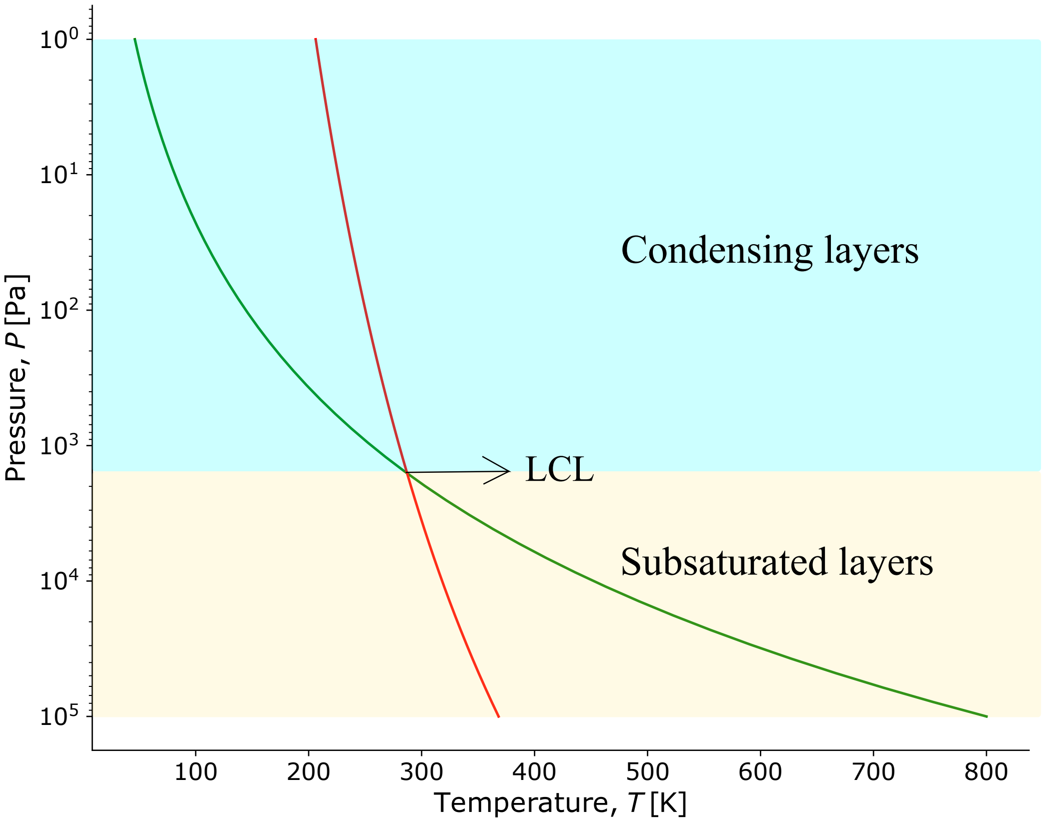

Figure 3.1: Sketch of the condensing and subsaturated layers in a pure steam column with a surface temperature of 800 K and a pressure of 1 bar. The red curve is the Clausius-Clapeyron curve according to Equation 3.12, and the green curve is the dry adiabat following Equation 3.8. The lifted condensation level (LCL) is where the dry adiabat intersects the dew point.

The first simplification is considering the phase change between a gas phase and a condensed phase like a liquid. If T is low enough relative to the critical point of the substance, then we can neglect the volume of the condensed phase. For water, the critical point is at ($T_c = 647.096$ K, $P_c = 220.64$ bar). With a surface temperature $T_s = 400$ K, the air temperature is always lower than T_c and local pressures are also below 1 bar, which validates this assumption as long as the surface stays around this range. In a setting with a magma ocean at 2500 K, this will not hold any longer.

The second simplification comes if P is also low enough that we can apply the ideal gas law, most valid at relatively low pressures and high temperatures. Figure 3.2 shows the domain of temperatures and specific volumes where the percent deviation from ideal behaviour is smaller than 1%. Figure 3.3 is a Nelson-Obert compressibility chart showing how the compressibility factor $Z = \frac{Pv}{RT}$ deviates from the ideal value of unity as a function of the reduced pressure $P_R = \frac{P}{P_c}$. The reduced temperature is correspondingly $T_R = \frac{T}{T_c}$. Below 1 bar and generally for $P_R << 1$, the ideal gas law for water is valid with an error smaller than 0.1% regardless of temperature. For $T_R > 2$, the ideal approximation yields good accuracy unless $P_R >> 1$. For higher pressures, in regions close to the phase boundary and especially the critical point, the errors get large enough that the ideal gas law becomes invalid, and a more elaborate equation of state is needed for accurate results.

The third simplification comes when we assume that the latent heat is a constant of temperature. This assumption is most valid if the temperature stays within the range where the latent heat varies little relative to its mean, and only really needed with an analytic expression of the moist adiabat. Accounting for its temperature dependence is straightforward when we instead integrate the slope function over the column. On Figure 3.4, we see how the slope of the latent heat varies as it gets closer to the critical point. Not only does the slope of the latent heat increase, increasingly invalidating the third simplification, but the density difference between the phases become small, which also invalidates the first simplification. Depending on the critical point density, the second simplification can also become invalid.

Since the prime interest of this thesis is in the high temperature conditions of the runaway greenhouse, the behaviour near the critical point could become important, for instance in cases where the atmosphere is in equilibrium with a hot liquid ocean. Figure 3.5 shows the density of the liquid and vapour phases of water from its

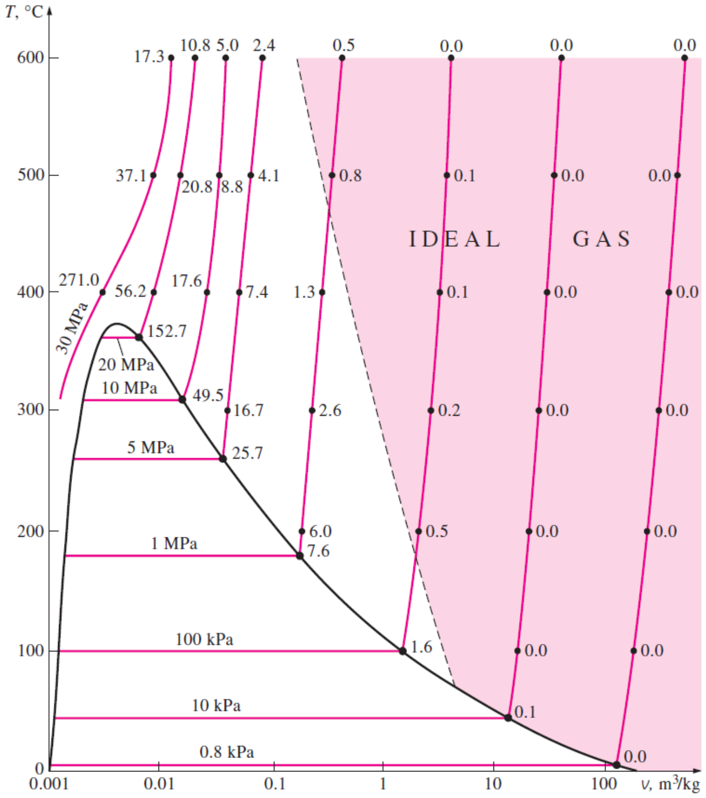

FIGURE 3–49

Percentage of error ($[|v_{\text{table}} - v_{\text{ideal}}|/v_{\text{table}}] \times 100$) involved in assuming steam to be an ideal gas, and the region where steam can be treated as an ideal gas with less than 1 percent error.

Figure 3.2: Figure taken from Cengel et al. (2011), showing the percent errors calculated using the ideal gas law for water vapour on a graph of the temperature T as a function of specific volume v. The solid black line is the liquid-vapour phase boundary.

freezing point to its critical point. There is a big density jump at about 600 K, and the critical point has to be approached relatively closely before the density jump gets small. This means that using the simplified form of the Clausius-Clapeyron relation can provide a good approximation up to around 600 K, so long as the decline in latent heat is taken into account. The reason that the Clausius-Clapeyron relation is only valid where the density jump is large stems from the first simplification of the general form mentioned above. The specific volume of the liquid phase has to be negligible relative to that of the gas phase. Close to the critical point, where the

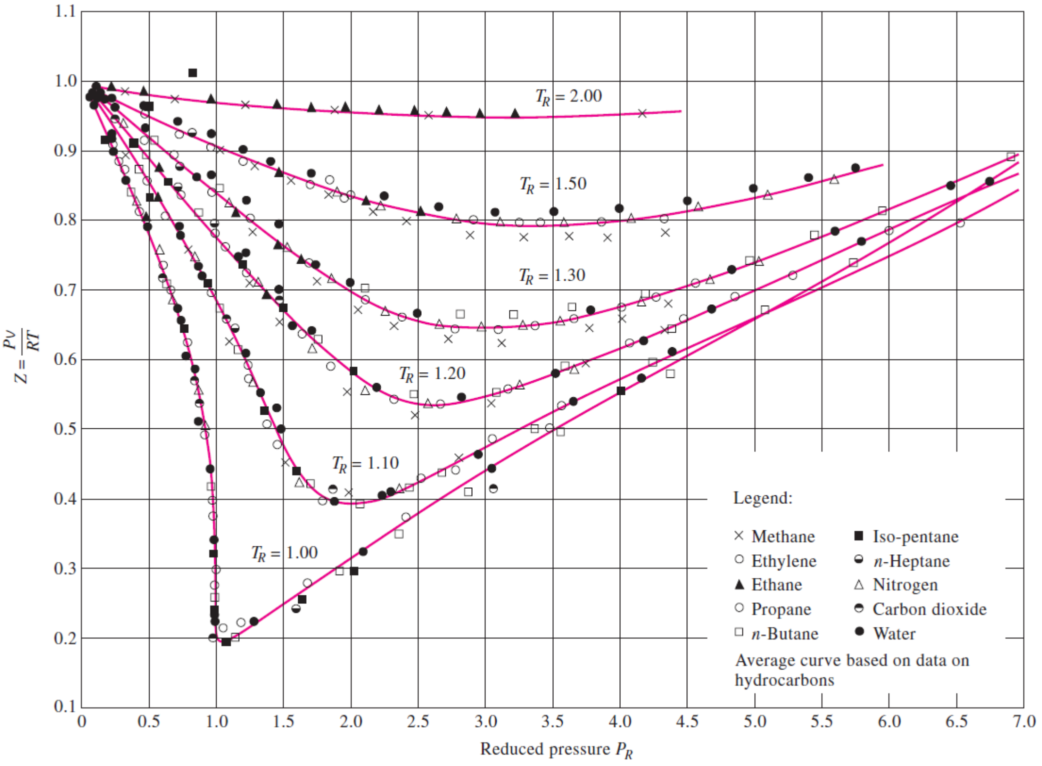

FIGURE 3–51

Comparison of *Z* factors for various gases.

Source: *Gour-Jen Su, "Modified Law of Corresponding States,"* Ind. Eng. Chem. *(international ed.) 38 (1946), p. 803.*

Figure 3.3: Figure taken from Cengel et al. (2011), showing the compressibility factor $Z = \frac{Pv}{RT}$ as a function of the reduced pressure, which is $P_R = \frac{P}{P_c}$, of 10 gases including water vapour.

densities are close to each other, this assumption loses its validity. However, in the post-runaway conditions considered in Chapters 4-8, the condensation happens in a relatively cool part of the atmosphere, so behaviour near the critical point does not enter the problem.

Moist convection refers to the vertical motion of parcels of air in which phase changes such as condensation and evaporation play a significant role. As we have seen, the moist pseudo-adiabat changes the way the temperature of a parcel would

---

[1] `http://ddbonline.ddbst.com`

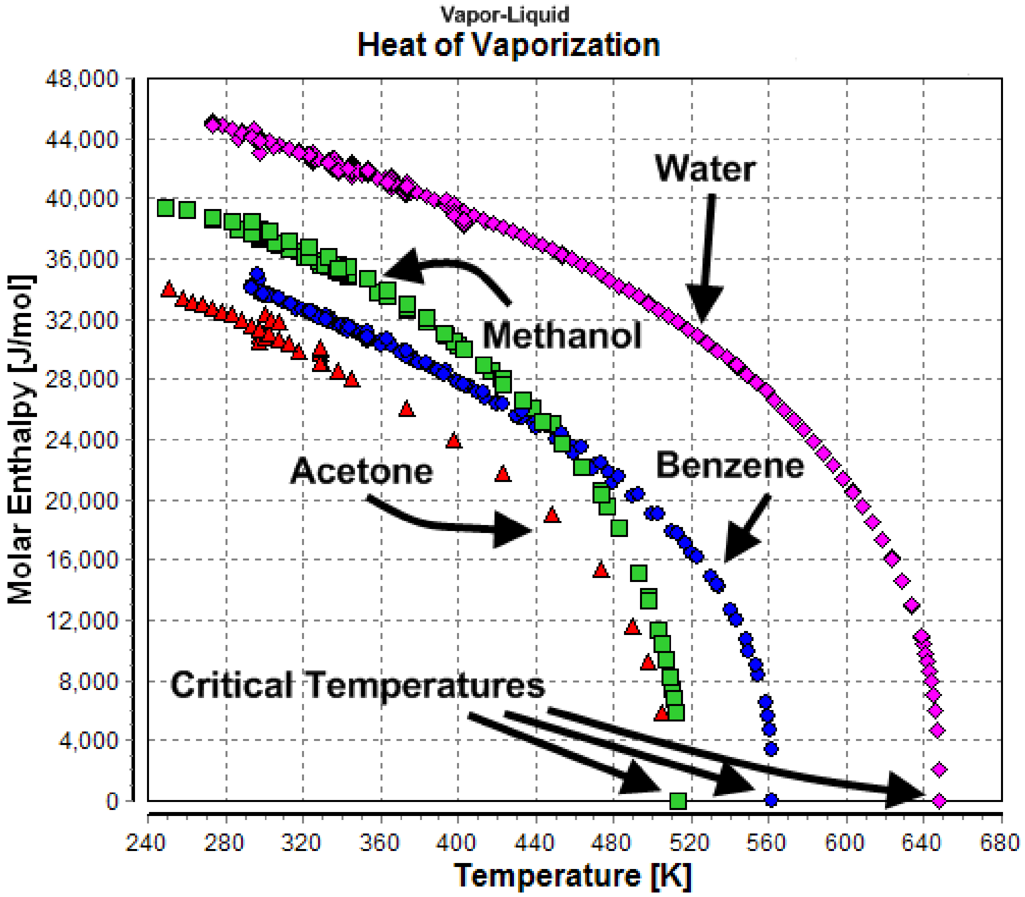

Figure 3.4: Data taken from Dortmund Data Bank[1]. It shows the dependence of the latent heat of vaporization to temperature. For instance, between 273 K to its critical point, the latent heat of water vapour reaches zero and its slope tends to infinity, yielding the discontinuity that characterizes the transition between the sub-critical and the critical regime.

change when it gets positively or negatively buoyant. This has profound implications for the thermal evolution of a planet, which will become clear in the following chapters.

The atmosphere of the Earth is very much in a dilute regime relative to water vapour, meaning that even though the latter is a condensible, it can be modelled as a trace gas

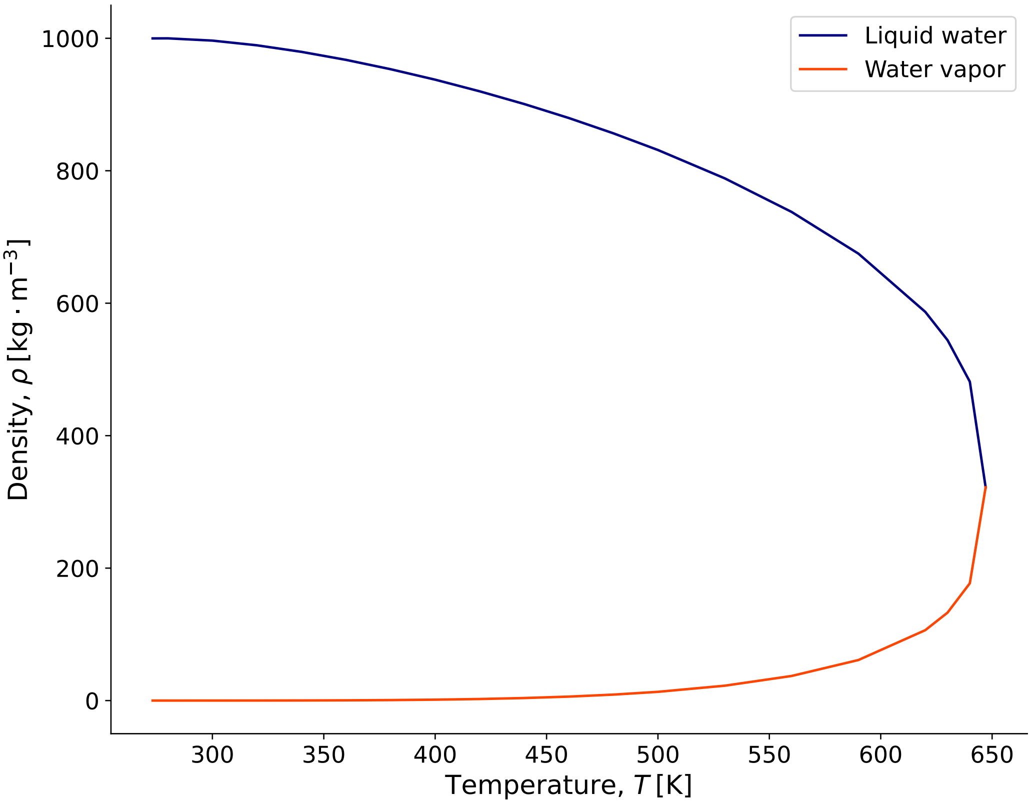

Figure 3.5: Data taken from the Engineering ToolBox (2018). It shows the temperature dependence of the density of the liquid and vapour phases of water on the liquid-vapour phase boundary.

that has little impact on the surface pressure when it goes through phase changes. On the other hand, if we consider a planet where surface air can reach water vapour mixing ratios of 10% or more, the atmosphere is considered to be in a non-dilute state, which features drastically different behaviours to the ones we are accustomed to. The pseudoadiabat described by Equation 3.11 is valid in non-dilute cases with a single condensible. Previous works (Ding & Pierrehumbert, 2016, 2018, 2020; Pierrehumbert & Ding, 2016; Turbet et al., 2021) have started the exploration of such regimes, from dynamical, convective, radiative, and observational perspectives.

The extreme case of the non-dilute regime is the pure steam limit, where the condensible makes up the totality of the atmosphere. Although idealized, it is a good approximation of cases where the planet's initial inventory of this condensible is large enough that, evaporated, it comes to dominate all other constituents. It would be the case of the Earth, which has about 260 bars of condensed water on its surface. If all of it were to evaporate into the atmosphere for one reason or another, the latter would be composed of 260 bars of water vapour and 1 bar of other constituents. This means that water vapour would have a mixing ratio slightly higher than 99.6$\%$, and would therefore dominate the dynamics and radiative properties of the atmosphere.

The dew-point adiabat depends on pressure and thermodynamic constants alone, unlike the case of a mixture with a non-condensible background gas. Therefore, moist convection in the pure steam limit can be accounted for simply by adjusting the temperature profile to the pseudo-adiabatic lapse rate whenever the environment becomes colder than the local dew point of the condensible, without any need for a slope adjustment.

If the atmosphere has multiple condensible components and none of them dominates the others, the adjustment scheme is more complicated. Previous works have started to tackle this issue by accounting for a non-condensible mixed in with a condensible comprising a large enough fraction of the total that the system is considered non-dilute (Leconte, Selsis, Hersant, & Guillot, 2017; Pierrehumbert, 2010), so that the derived formulae are valid even though the condensible cannot be represented as a trace gas. Lichtenberg et al. (2021) used a slightly modified version of the scheme developed by Pierrehumbert (2010) to investigate possible atmospheric compositions arising from magma ocean atmospheres with various non-dilute condensible species, although with this method, each species had to be treated separately, with each atmosphere studied having a different but single condensible component.

Dealing with more than one condensible requires tracking the partial pressures and mixing ratios of each volatile in the system. The temperature follows a profile resulting from the combination of the dry and moist pseudo-adiabatic lapse rates of each constituent depending on the local pressure and temperature at each atmospheric layer. Initial versions of such a generalised pseudo-adiabatic lapse rate has been developed and used with idealized precipitation, first by Li, Ingersoll, and Oyafuso (2018) in the context of hot Jupiters, and then by Graham, Lichtenberg, Boukrouche, and Pierrehumbert (2021) who built upon the previous scheme to include a tunable parameter that controls the efficiency of precipitation, and benchmarked the new method in different planetary contexts.

3.3 Idealized radiation

Though the absorption coefficient of actual atmospheric constituents is typically a sensitive function of wavelength, in idealized simulations it has proved valuable to use variants of "grey" schemes, which simplify or eliminate this dependence. The most simple radiation schemes used in climate and retrieval models are "pure grey" and "semi-grey" ones. Pure grey radiation consists in principle of setting the same opacity coefficient across the electromagnetic spectrum, though this is rarely done. This way, optical depths, fluxes and temperature change rates are independent of wavelength. This is the fastest and least accurate method, as any substantial atmosphere will be composed of molecules that have a complex and very wavelength-dependent absorption spectrum. Semi-grey schemes separate the "longwave" and "shortwave" parts of the spectrum, and sets two different opacity coefficients for each one. This has the advantage of retaining most of the speed of the pure grey approximation while accounting for the fact that gases will generally be less opaque in the shortwave regions, notably in the visible and ultraviolet regions, than in longer waves. However, at the high temperatures that this thesis is dealing with, the atmosphere radiates significantly in the near-infrared (NIR) and even visible, which blurs the usual distinctions between emitted radiation and incoming stellar shortwave radiation. Moreover, some molecules, like water vapour, are still relatively opaque throughout the spectrum, and more importantly, display large variations in opacity due to their window regions. Accounting for these variations requires compromising between the speed of the scheme and its accuracy. "Band-grey", or "picket-fence" (Parmentier & Guillot, 2014) are umbrella terms able to qualify any scheme that includes more than two spectral regions with different opacity coefficients. The advantage of these schemes is that they can include an arbitrary number of bands with arbitrary width and opacity in each spectral region, as illustrated in Fig. 3.6, depending on the context of a particular study.

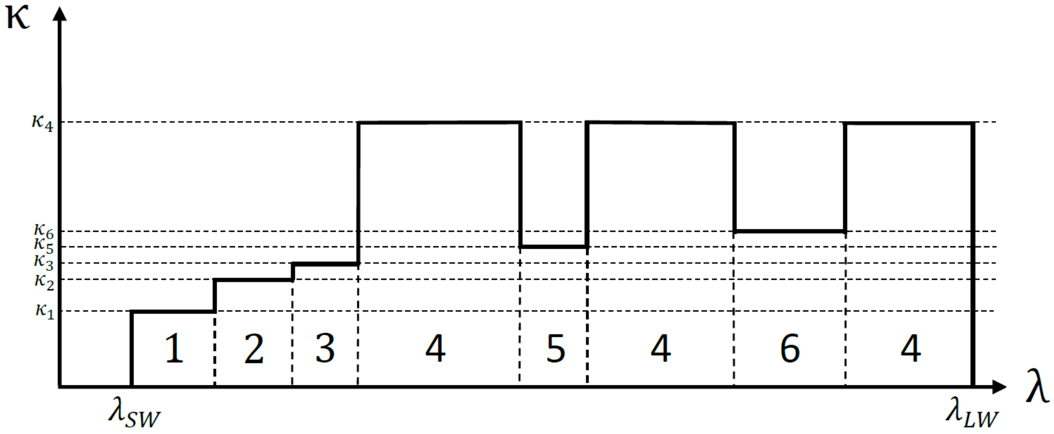

Figure 3.6: Illustration of the framework of a band-grey radiation code. The spectrum is divided into several bands of varying opacity coefficients κ between a minimum wavelength λ_{SW} and a maximum wavelength λ_{LW}. This particular framework uses six bands including two atmospheric windows represented by bands 5 and 6.

In the context of a pure steam atmosphere, Boukrouche et al. (2021) have developed a band-grey radiation-convection model that is tuned to the spectrum of water vapour. This partly determined the optimal number of bands that should be used in the model. Other considerations that affected this decision are developed in Chapter 4, which delves into the formulation of this model and on one-dimensional runaway greenhouse simulations using it. Although water vapour has a relatively high opacity across the spectrum, it is significantly higher in the infrared, and decreases steadily toward the ultraviolet regions. This implies separating the infrared and the visible together with the UV into two bands. Beyond this, it has several important window regions in the infrared, including two main ones in the thermal infrared, between 3.4 and 4.5 microns, and between 7.7 and 20 microns. These windows feature a significant drop in opacity that warrants defining them as separate bands as well. This makes up four bands in total, though further considerations led us to split the visible and UV regions. For every additional band, we lose some speed but gain some accuracy, and it is up to the user to decide where best to strike this balance depending on the particular needs of the study.

3.4 Real-gas radiation

Real-gas radiation is at the other extreme of complexity in radiation schemes. While pure grey schemes are the fastest and least accurate ones, real-gas schemes are the slowest and most accurate. The most obvious way of dealing with real-gas radiation is by accounting for the opacity introduced by each and every absorption line across the spectrum. Fig. 3.7 shows the forest of spectral lines that the main isotopologue of water vapour, $\mathrm{H}_2^{16}\mathrm{O}$, produces between 500 and 717 cm^{-1} at a pressure of 1 bar and a temperature of 300 K. This illustrates the complexity of the line-by-line approach. It involves retrieving the opacity coefficients across a grid of wavenumbers fine enough that enough lines are sampled for the accuracy needs of the study. The shape of the lines makes this a challenge. The standard approximation of spectral line shapes is the Voigt profile, which is the convolution of the Doppler and Lorentz profiles,

$$\begin{aligned} f_{\text{Voigt}}(\nu) &= f_L(\nu) \otimes f_D(\nu) \\ &= \frac{\alpha_L}{\pi} \frac{1}{(\nu-\nu_0)^2 + \alpha_L^2} \otimes \frac{1}{\alpha_D \sqrt{\pi}} \exp\left[-\left(\frac{\nu - \nu_0}{\alpha_D} \right)^2 \right], \end{aligned} \tag{3.13}$$

with f_L and f_D the Lorentz and Doppler profiles, α_L and α_D the half-widths for pressure and Doppler broadening, and ν_0 the frequency of the line centre. Given that the slope of the profile is much larger near the center than at the wings, any wavenumber grid of insufficient resolution will preferentially sample the wings of the lines rather than the peaks. Evaluating the opacity coefficient at every line therefore creates a need for very high spectral resolutions, and large amounts of computer resources and storage.

The correlated-k method has been developed as a compromise between speed and accuracy while still remaining in the domain of real-gas radiation. The fundamental basis for this concept is that, though the opacity coefficients do not vary following any convenient function across the spectrum, we can sort them into a function that increases monotonously. This works because, if we assume that scattering properties and the Planck function are constant within each spectral bin (Goody, West, Chen, & Crisp, 1989), the position of the opacity coefficient in the spectrum does not actually matter; what does is the fraction of the spectrum that each opacity coefficient occupies. Therefore, we divide the spectrum into a given number of bands, and in each band we use a cumulative probability distribution g of the opacity to compute a small number n_k^b of opacity coefficients k_l^b with their associated weights w_l^b in the band b, with $1 \leq l \leq n_k^b$. Then, since $g(k)$ is a monotonous function of k

---

[2] `https://dace.unige.ch/opacity/`

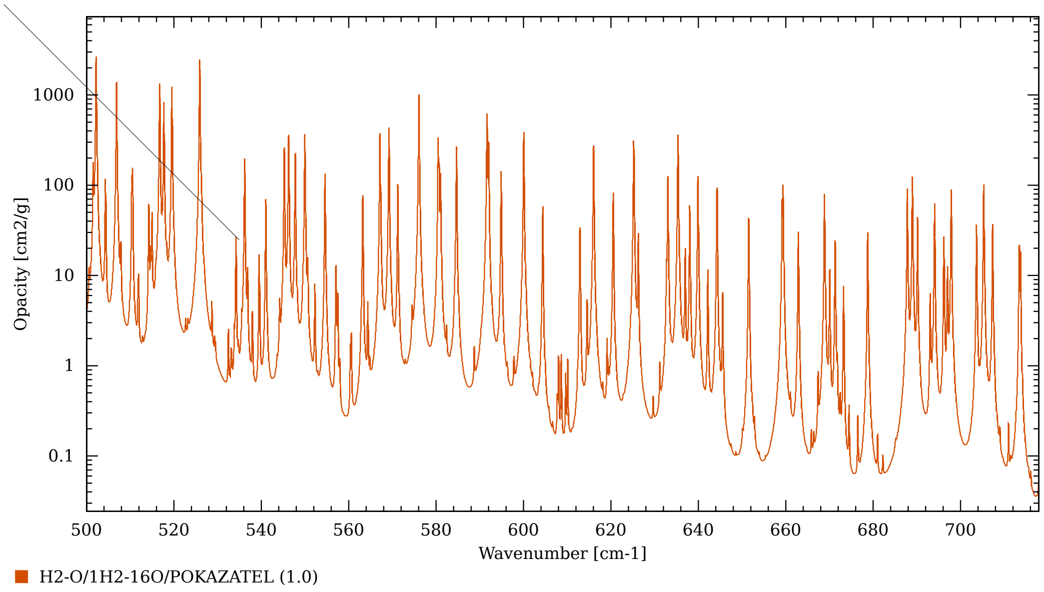

Figure 3.7: Data taken from Data & Analysis Center for Exoplanets (DACE)[2]. It shows the forest of spectral lines produced by $H_2^{16}O$ between 500 and 717 cm^{-1} at a pressure of 1 bar and a temperature of 300 K according to the POKAZATEL line list of the ExoMol database.

and the opacity itself can be defined as $k(g)$, we can replace the wavenumber σ as an independent variable by g in the following way.

$$\begin{aligned} T(u) &= \int_{\Delta\sigma} w(\sigma) e^{-k(\sigma)u} d\sigma \\ &= \int_0^1 e^{-k(g)u} dg \approx \sum_{l=1}^{n_k^b} w_l^b e^{-k_l^b u}, \end{aligned} \tag{3.14}$$

where T is the transmission function in a homogeneous layer of gas, $w(\sigma)$ is the weighting function, $\Delta\sigma$ the wavenumber interval of band b, and u is the column density of gas.

The homogeneous assumption mentioned above is noteworthy. Indeed, while the sorting provides an accurate computation of the transmission function for a homogeneous path at constant pressure and temperature, for an inhomogeneous path the position of the absorption features in wavelength space can matter, because of changes in the shape of g(k). This is where the "correlated" part of "correlated-k" comes in. There are some additional assumptions that need to be made in applying the ideas to an inhomogeneous path, which are discussed in previous works such as Goody et al. (1989) and Amundsen, Tremblin, Manners, Baraffe, and Mayne (2017).

4 | Simulating the runaway greenhouse effect in 1D

We started the investigation of the runaway and post-runaway climate regimes in one dimension. In pursuit of the third goal outlined in Section 1.2, we made use of a contribution function to determine the contribution of various levels in the atmosphere to the radiative emission to space. We showed that the transition from a runaway to a post-runaway climate is marked in the infrared regions by a shift in the altitude of the radiating layer, here called the infrared photosphere of the planet, and in the visible and ultraviolet regions by a significant contribution of thermally emitted outgoing shortwave radiation.

4.1 Radiative considerations

Determination of the climate evolution requires models of the vertical transport of energy by radiation and convection. In this work, we considered only clear-sky conditions in the radiative calculation. Though the radiative effects of clouds are certainly important in determining the conditions for a runaway and the nature of the post-runaway climate regime, a restriction to clear-sky conditions allows us to focus on the underlying physics of the runaway, and makes it easier to compare with existing results in the literature. Furthermore, it is impossible to properly project cloud properties in 1D models, since the necessary dynamical information is not available in a one-dimensional column; such processes are best treated in the context of 3D modelling.

For radiative transfer incorporating comprehensive real-gas opacity variations, we employ the SOCRATES radiative transfer suite (Edwards & Slingo, 1996), which makes use of the correlated-k method to approximate the transmission function and solves the plane-parallel, two-stream approximated radiative transfer equations. For the SOCRATES simulations, the line-by-line opacity data was taken from the HITRAN spectroscopic database (Gordon et al., 2017), choosing the main isotopologue $H_2^{16}O$, and taking the complete available wavenumber range [0.072, 25710.825] cm^{-1}. The self-broadened continuum of water vapour was taken from `https://github.com/DavidSAmundsen/socrates_tools/tree/master/continuum/h2o`, using the files mt_ckd_v3.0_s260 and mt_ckd_v3.0_s296. Though SOCRATES has the capability to represent scattering, our simulations ignore this effect for thermally emitted radiation, though we shall see eventually that in some cases there is enough thermal emission of shortwave radiation to make scattering potentially significant.

The SOCRATES suite uses the two-stream form of the Schwarzschild equations. In the absence of scattering, the up- and downward fluxes satisfy

$$\frac{1}{D}\frac{d}{d\tau_\nu}I_+(\tau_\nu,\nu) = -I_+(\tau_\nu,\nu)+\pi B(\nu,T(\tau_\nu)), \tag{4.1}$$

$$\frac{1}{D}\frac{d}{d\tau_\nu}I_-(\tau_\nu,\nu) = I_-(\tau_\nu,\nu)-\pi B(\nu,T(\tau_\nu)), \tag{4.2}$$

with $D = 1.66$ the diffusivity factor approximating the angular dependence, I_+ and I_- the upward and downward fluxes evaluated at the optical depth τ_ν and at the frequency ν, and B the Planck function evaluated at the frequency ν and at the temperature $T(\tau_\nu)$.

To provide a simpler route to understanding the physical processes involved in runaway and post-runaway atmospheres, and to allow for the greater computational efficiency needed to facilitate later 3D calculations, we also introduce a simplified band-grey radiative transfer model.

Directly integrating the Schwarzschild integrands in an optically thick setting requires a very high vertical resolution, which makes getting a good accuracy difficult in a reasonable amount of time. In order to bypass this issue, we use an approximation using a two-stream source function method from Toon, McKay, Ackerman, and Santhanam (1989), which is faster by more than one order of magnitude, well-suited for optically thick atmospheres, and most accurate in the limit of pure absorption. The source function technique is a two-stream method that uses 'sources' in the atmosphere (i.e. the blackbody flux), and follows the stream of the sources in the upward and downward directions, as a solution to the Schwarzschild equations. Instead of approximating the angular dependence with the diffusion coefficient mentioned above, we use a 2-point Gaussian quadrature with weights determined by the Gauss-Legendre quadrature law. In this formulation, the flux I is integrated over all cosine angles.

$$I(\tau_\nu, \nu) = \pi \int_\mu I_\mu d\mu, \tag{4.3}$$

which in Gauss quadrature becomes

$$I(\tau_\nu, \nu) = \pi \sum_\mu w_\mu I_\mu \mu, \tag{4.4}$$

where I_μ is the directional intensity, w_μ is the weight for that quadrature point, and μ the cosine angle for that quadrature point.

Incorporation of two-stream scattering effects coupling the upward and downward streams is straightforward but will not be pursued here.

The band-grey approximation involves dividing the spectral range into a small number of regions with opacity coefficients assumed to be uniform over each region. This allows a bandwise decomposition of any quantity computed by the model, a feature that we will use in Chapter 5. Here we approximate two of the main near-infrared (NIR) atmospheric windows of water vapour, designated as W1 and W2 in this work. Their opacities are computed by taking the average between the Rosseland mean and the Planck mean of the absorption coefficients over each band. The Rosseland mean, which overweighs the smaller opacities, is defined as

$$\frac{1}{\kappa_{\mathrm{R}}} = \left(\int_0^\infty \frac{\partial B_\nu}{\partial T} d\nu \right)^{-1} \int_0^\infty \frac{1}{\kappa_\nu} \frac{\partial B_\nu}{\partial T} d\nu, \tag{4.5}$$

whereas the Planck mean, which overweighs the larger opacities, is

$$\kappa_{\mathrm{P}} = \left(\int_0^\infty B_\nu d\nu \right)^{-1} \int_0^\infty \kappa_\nu B_\nu d\nu, \tag{4.6}$$

where κ_{R} is the Rosseland mean opacity, κ_{P} is the Planck mean opacity, B_ν is the Planck function depending on frequency ν and temperature T, and κ_ν is the opacity coefficient in $\mathrm{m}^2\,\mathrm{kg}^{-2}$ corresponding to the frequency ν. The arithmetic average between the two means is roughly equal to half of the Plank mean. A better approach would have been to use the Rosseland mean alone, which is valid in the limit of high optical thickness. As explained in Chapter 5 however, these averaged opacity coefficients were later tuned to fit the non-grey contribution function profiles, which makes the averaging operation effectively moot.

Region	Spectral range $[\mathrm{cm}^{-1}]$	Opacity source
UV	$(25000, 40500)$	POKAZATEL
VIS1	$(18750, 25000)$	POKAZATEL
VIS2	$(12500, 18750)$	POKAZATEL
IR	$(1, 12500) - \mathrm{W1} - \mathrm{W2}$	POKAZATEL
W1	$(2200, 2900)$	MT_CKD 3.4
W2	$(500, 1300)$	MT_CKD 3.4
SOCRATES	$(1, 24500)$	HITRAN/MT_CKD 3.4

Table 4.1: Spectral regions and opacity sources considered in the band-grey model and SOCRATES. The longwave bound of the band-grey spectral range, 1 cm^{-1}, is the HITRAN longwave bound. Its shortwave bound, 40500 cm^{-1}, is the POKAZATEL shortwave bound. When using a single shortwave band in the band-grey model, we combine UV, VIS1, and VIS2 into one band called SW going from 12500 to 40500 cm^{-1}. When using two, we combine VIS1 and VIS2 into a single visible band, VIS, defined between 12500 and 25000 cm^{-1}.

The MT_CKD 3.4 data[1] is given at a reference pressure and temperature of 1013 mbar and 260 K. It scales as the normalized density $\frac{\rho}{\rho_0} = \frac{P}{P_0}\frac{T_0}{T}$. The infrared and shortwave spectral regions outside the windows have their opacity averaged with the Rosseland and Planck means as above. The opacity data of these regions is taken from the ExoMol POKAZATEL[2] water line list (Tennyson et al., 2020), which is a theoretically derived line list reliable for temperatures up to and above 3000 K. An updated version of it will form the basis of the new HITEMP water line list at short wavelengths. For each spectral region defined in the band-grey model, we compute a mean opacity table that depends on pressure as well as temperature.

In practice, we first get an averaged opacity table based on the pressure-temperature grid of data sources. The POKAZATEL grid goes from 50 K to 2900 K in temperature, and from 0.001 Pa to 10^8 Pa in pressure. Because we account for water

---

[1] `https://github.com/AER-RC/mt-ckd`

[2] `https://chaldene.unibe.ch/data/Opacity3/1H2-16O__POKAZATEL_e0DAT` (Grimm & Heng, 2015)

condensation, the temperature cannot fall under the dew point of water vapour. The dew point temperature at the minimum pressure of 0.001 Pa is around 163 K. Since the temperature step is 50 K between 50 and 700 K, we start the temperature grid at 200 K instead of 50 K or 150 K. With the Planck means, the Rosseland means, and the average between the two computed, we get opacity matrices corresponding to 27 temperatures and 34 pressures along the POKAZATEL grids. We then use a two-step spline interpolation of first order along the temperature and the pressure dimensions to increase the resolution of the matrices to 100x100. Different interpolation methods were tried, including finding the nearest neighbours, or linear, quadratic, and cubic interpolations. Splines of orders higher than one proved to be unnecessary, while a simple linear method or finding the nearest neighbours created (κ,P,T) surfaces that were too ragged. The scaling law of the MT_CKD 3.4 data described above gives us its variation with pressure and temperature, so that the increase in resolution does not necessitate any interpolation. One can visualize the opacity surfaces of each band on Figures 4.1 and 4.2, depending on how the shortwave region is split.

As the model goes through the atmospheric layers from the top to the bottom, it finds the appropriate opacity coefficients to use based on the current pressure and temperature using a bilinear interpolation routine to avoid vertical jumps in opacity and in net flux. If the current pressure or temperature is outside the range of the opacity tables, the model will instead find the opacity coefficient corresponding to the closest pressure and temperature in the table.

The way the model provides Planck functions for the flux calculations has been changed a few times, and we have settled on an approach that uses look-up tables. We first generate an array of Planck functions integrated over each band over a range of temperatures from 1 to 3000 K with a step of 1 K. Given a band and a

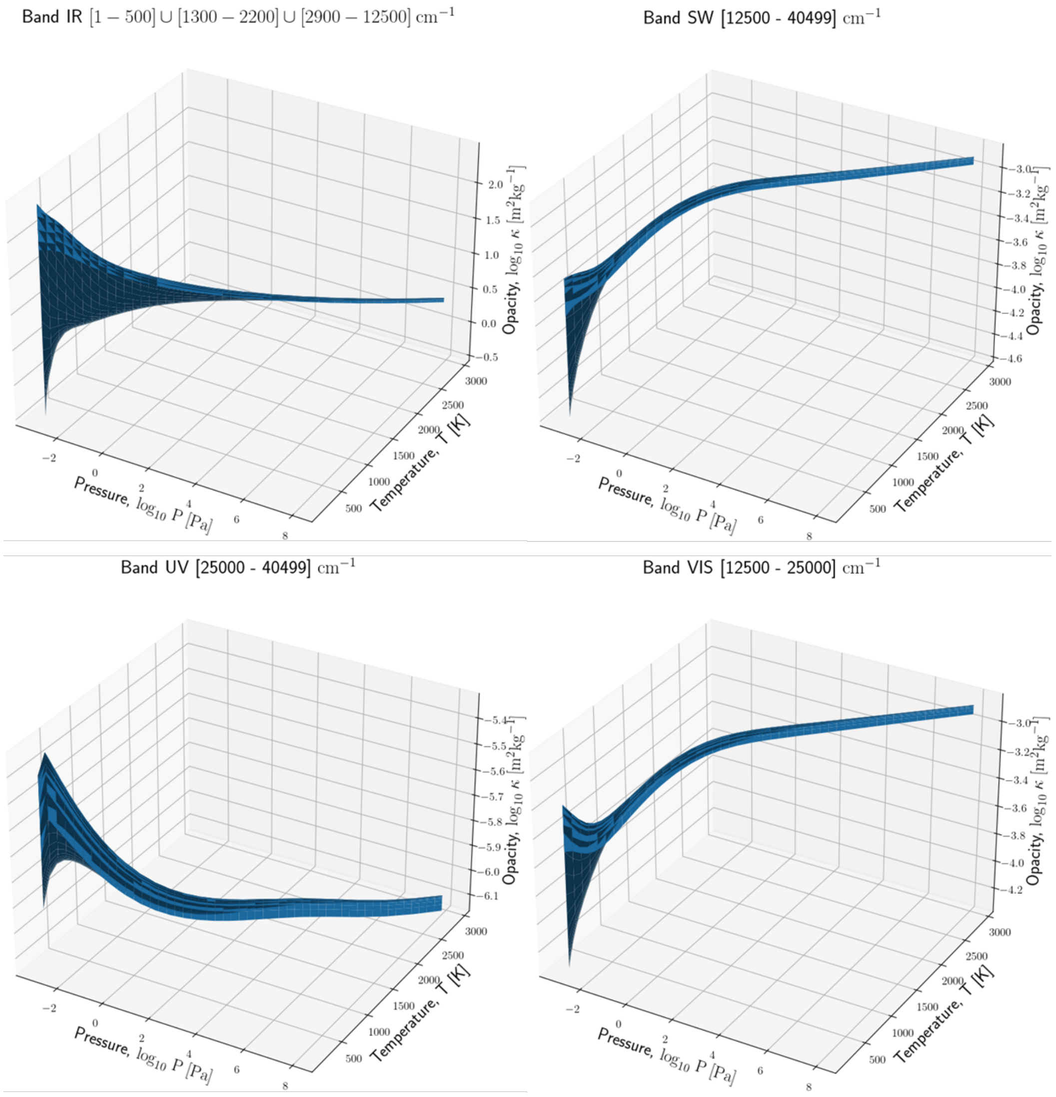

Figure 4.1: Opacity coefficients in bands IR, SW, UV, and VIS, for all pressures and temperatures in their respective validity ranges.

current temperature, the model then reads the corresponding Planck value and feeds it to the radiation scheme to compute fluxes. This increases the performance of the model significantly, as reading tables once at the start of the run is much faster than integrating the Planck function multiple times at every iteration.

The complete spectral range can be seen on Fig. 5.2 and Panel A of Fig. 5.1, only

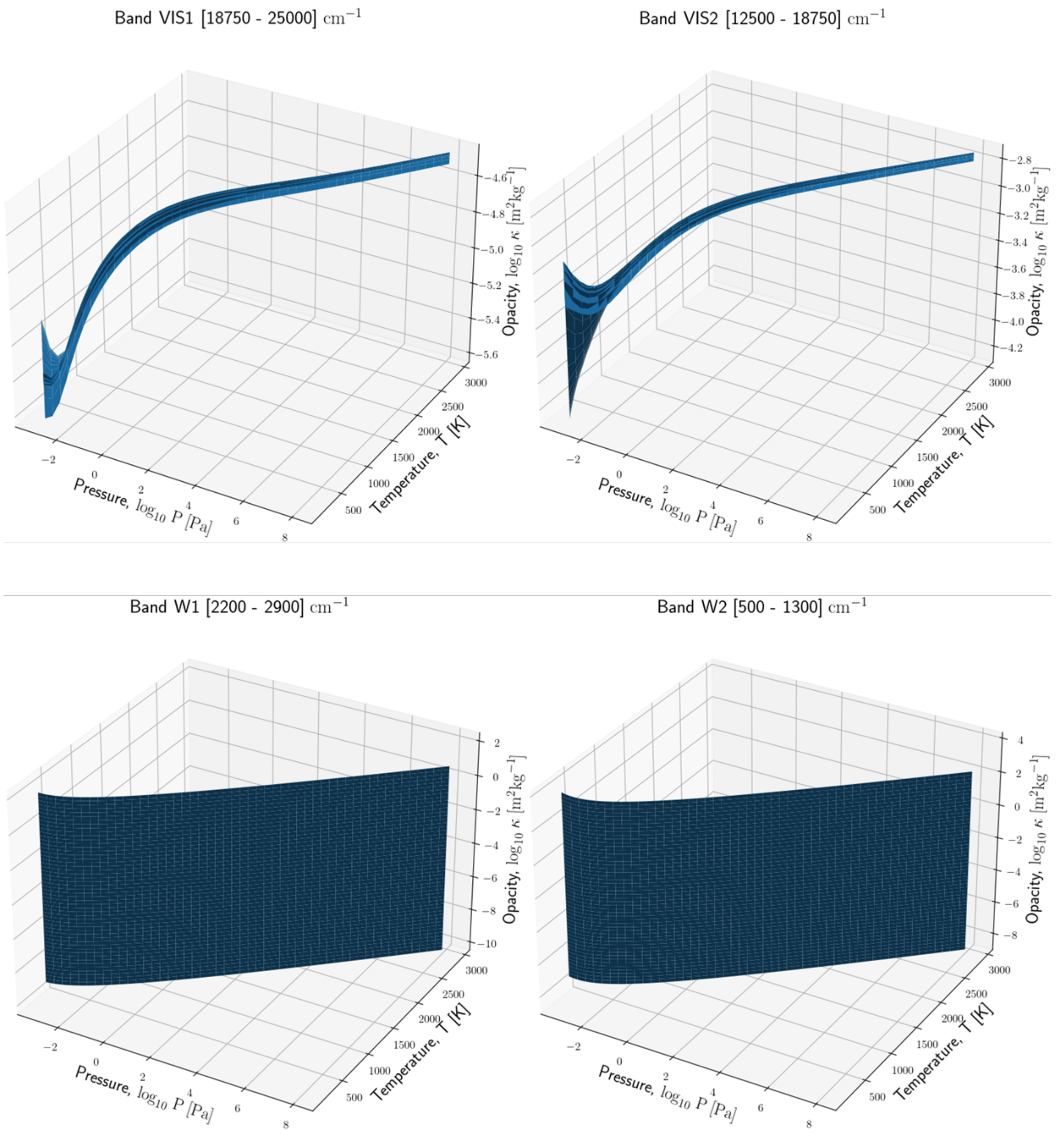

Figure 4.2: Same as Figure 4.1, for bands VIS1, VIS2, W1, and W2.

at a pressure of 0.1 bar for clarity. The spectral range used in SOCRATES as well as in each region included in the band-grey model are listed in Tab. 4.1 along with the sources of the corresponding opacity coefficients. We employ a total of 318 bands between the bounds of the SOCRATES spectral range indicated in Tab. 4.1. The conversion from cm^2 $\mathrm{molecule}^{-1}$ to m^2 kg^{-1} is done with

$$\kappa[\mathrm{m}^2\ \mathrm{kg}^{-1}] = \frac{\kappa[\mathrm{cm}^2\ \mathrm{molecule}^{-1}] N_{\mathrm{Avogadro}}}{M[\mathrm{g\ mol}^{-1}]}\ 10^3[\mathrm{g\ kg}^{-1}]\ 10^{-4}[\mathrm{m}^2\ \mathrm{cm}^{-2}], \quad (4.7)$$

where M is the molar mass of the absorber.

Although the continuum dominates in the windows and the lines dominate outside, in actuality both would contribute some opacity everywhere. It would therefore make sense for future works to improve the model by accounting for both opacity sources over each band.

At the high temperatures considered here, there is significant diffuse thermal emission in the visible (VIS) and ultraviolet (UV) spectral regions. These are treated identically to the longer wavelength radiation. In the general case it is also necessary to consider the absorption and scattering of the incident direct-beam radiation received from the star, but as will be seen shortly the approach to atmospheric structure adopted in this work does not require the vertical profile of the resulting fluxes, but only a specification of the net stellar energy absorbed by the planet, which is then balanced against the outgoing thermal planetary radiation.

We used SOCRATES as a benchmark for the band-grey model. Figure 4.3 compares the flux profiles of the two models for the same temperature profile, without time stepping. The profile uses a surface temperature of 1225 K and a surface pressure of 10 bar. It is then defined with a hybrid-sigma pressure grid with 47 levels; the highest interface pressure level is 0.1 mbar. The instellation is in both cases set to the substellar instellation of TRAPPIST-1b, assuming tidal locking.

$$\frac{L_{\mathrm{TRAPPIST\text{-}1}}}{4\pi\ (a_{\mathrm{major}}\ \mathrm{AU})^2} \approx 5652\ \mathrm{W\,m}^{-2}, \quad (4.8)$$

with $L_{\text{TRAPPIST-1}} = 5.53 \cdot 10^{-4} L_{\text{sun}}$, $L_{\text{sun}} = 3.828\ 10^{26}$ W, and $a_{\text{major}} = 0.01154$ AU.

The stellar zenith angle is chosen according to Hamano, Kawahara, Abe, Onishi, and Hashimoto (2015), setting $\mu_z = \cos\theta = \frac{1}{\sqrt{3}}$ which corresponds to a zenith angle θ of 54.74°.

Dry and moist convective adjustments are applied to the profile. Figure 4.3 shows the net fluxes computed with this temperature profile. The net flux is

$$\begin{aligned}\text{Net flux} &= (\text{Upward diffuse flux} - \text{Downward diffuse flux}) \\ &\quad + (\text{Upward direct flux} - \text{Downward direct flux}),\end{aligned}$$

where the diffuse flux is the flux thermally emitted upward or downward, and the direct flux refers to the incoming stellar beam and the part of it that is scattered upward. No scattering is included in this calculation, so the upward direct flux is zero. The net diffuse flux is then the difference between the upward and downward thermally emitted fluxes. The differences between the SOCRATES and band-grey fluxes underline the requirement for caution when using the band-grey approximation. Though the results obtained with both will be comparable, quantitative accuracy is only approached by real-gas radiation models, and band-grey models can even yield qualitative differences in results. The latter should therefore be checked with a real-gas radiation model in subsequent steps of such studies.

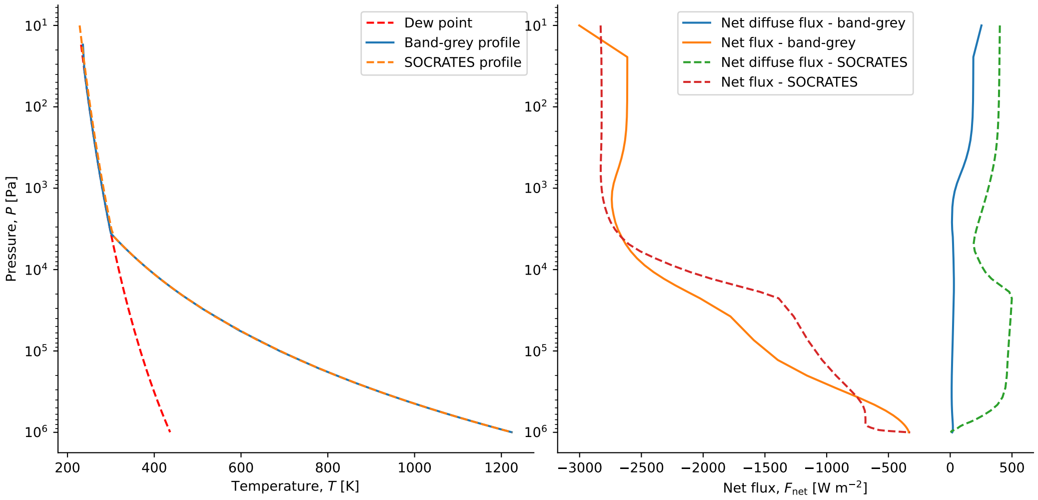

Figure 4.3: **(Left)** Temperature and **(Right)** flux profiles from SOCRATES and the band-grey model.

4.2 Convective considerations

Any radiative transfer calculation requires the specification of the temperature-pressure profile of the atmosphere, as well as the surface temperature; for a clear-sky pure steam atmosphere, no other atmospheric conditions need to be specified. As is common in runaway greenhouse calculations, we assume that the atmosphere has a deep convective layer extending upward from the ground, within which the $T(p)$ profile is given by the appropriate adiabat. This assumption requires that there be sufficient heating of the atmosphere from below to trigger convection, but a water vapour atmosphere of a few bars or more is so optically thick that it takes very little flux, either from instellation reaching the ground or from geothermal flux, to maintain convection. In the post-runaway state, there is no moisture source at the ground, so the atmosphere follows the dry water vapour adiabat until temperatures fall sufficiently that condensation occurs, whereafter the temperature follows the "dew point adiabat" obtained by solving Clausius-Clapeyron for temperature as a function of pressure.

In the unsaturated region extending upward from the planet's dry surface, the atmosphere is on the dry adiabat for water vapour, with corresponding lapse rate

$$\frac{d\ln T}{d\ln p} = \frac{R}{c_p(T)}, \tag{4.9}$$

which can be integrated numerically to obtain the profile $T(p)$. R is the gas constant for water vapour and the temperature-dependent specific heat $c_p(T)$ is taken from the NIST Chemistry WebBook, SRD 69 (Chase Jr, 1998; Cox, Wagman, & Medvedev, 1984). It is assumed that turbulent fluxes keep the temperature of the air near the surface equal to the surface temperature T_s, which provides the boundary condition needed to integrate the equation.

Within the saturated region aloft, the dew-point adiabat is given by

$$T_{\text{dew}}(p) = \frac{T_{\text{b}}}{1 - \frac{RT_{\text{b}}}{L}\ln\frac{p}{p_{\text{b}}}}, \tag{4.10}$$

with $(T_{\text{b}}, p_{\text{b}})$ the boiling point of water, or any point located on the same vapour/liquid co-existence curve as the boiling point. We have neglected the temperature dependence of latent heat in this formula and in all our calculations. Because we account for the temperature dependence of c_p, the code uses the same numerical procedure as Lichtenberg et al. (2021). A Runge-Kutta 4 integrator computes the dry pseudo-adiabatic $T(p)$ profile upward from the surface, up to the point where $T(p) < T_{\text{dew}}(p)$, whereafter the slope changes from $\frac{R}{c_p}$ to $\frac{RT}{L}$ as per the Clausius-Clapeyron relation.

On an adiabat, the temperature falls monotonically as the pressure is reduced to zero toward the top of the atmosphere, though on the dew-point adiabat this occurs very slowly owing to the logarithmic term in the denominator of Eq. 4.10 and the small value of the prefactor multiplying the logarithm. In reality, the temperature structure of the upper atmosphere will be altered by the formation of a stratosphere, which is in pure radiative equilibrium. The formation of a stratosphere warms the upper atmosphere and moderately increases radiation to space. In simplified 1D climate modelling it is common to attempt to represent this effect through inclusion of an isothermal stratosphere with temperature equal to the grey skin temperature (e.g. Kopparapu et al., 2013). Kasting (1988) and Kasting (1991) adopted the same approach to climate equilibration with an overlying isothermal stratosphere in the case of early Venus and early Mars. The dew-point adiabat for water already keeps the upper atmosphere quite warm, and there is no indication that the inclusion of a stratosphere has an important effect on the results for thick steam atmospheres. The neglect of the stratosphere leads to an underestimation of the outgoing planetary radiation to some extent, though it is likely to be slight for the steam atmospheres considered here. In any event, the isothermal assumption yields a poor representation of actual stratospheric behaviour for non-grey atmospheres, and the use of the grey skin temperature is problematic for atmospheres with significant wavelength-dependent opacity. If the stratosphere is thought to be important, it needs to be treated with a full radiative-convective formulation allowing for the formation of one or more pure-radiative layers, using forward calculations, either time-stepped or otherwise iterated toward stable solutions. Here, to allow for a focus on the key phenomena determining post-runaway climate, we adopt the simpler all-troposphere model of atmospheric structure, which does not require iterating.

Because the atmospheric $T(p)$ structure in this approximation can be written solely in terms of the surface temperature and pressure, the distribution of heating from atmospheric absorption of the incoming stellar flux does not enter into the calculation. The stellar heating affects the amount of convective heat transport needed to maintain the adiabat, but not the atmospheric structure or outgoing planetary radiation. In the event that a radiative zone appears somewhere in the column, if stellar or internal fluxes are able to reach it, it will warm up and the temperature profile will change accordingly. Otherwise, surface temperature is determined simply by balancing net top-of-atmosphere absorbed stellar radiation against outgoing planetary radiation, requiring only the specification of instellation and planetary albedo. In this study, we only compute the outgoing planetary radiation as a function of the surface temperature, and do not embark on a calculation of the planetary albedo; we only use an assumed albedo to provide some representative surface temperatures, and the reader is free to substitute other preferred values of albedo if warranted, e.g., by different surface characteristics. The planetary albedo is thus assumed to be constant at 0.2 for surface temperatures above 500 K, based on the planetary albedo calculations of Kopparapu et al. (2013), Goldblatt et al. (2013), and Hamano et al. (2015).

4.3 SOCRATES

SOCRATES (Suite Of Community RAdiative Transfer codes based on Edwards and Slingo, Edwards and Slingo (1996)) is a radiation model that makes use of the correlated-k approach to real-gas radiation described in Section 3.4. It is under continuous development and maintenance in the Met Office, in the United Kingdom. Here we will explain how the model works and the additions and fixes that were made to its source code.

SOCRATES uses a suite of preprocessing programs that define the structure of spectral files, which are particular text files that contain all the necessary information about the features of the atmosphere that depend on wavelength. This includes the number of spectral bands, the number of species in each band, their opacity coefficients, Rayleigh scattering coefficients, thermal source functions, stellar spectra, continua, aerosols, droplets, and ice crystals. The last three are usually ignored unless the needs of the study explicitly require them. Each of these categories is handled by blocks of data generated during the making of a spectral file from a console-based menu of actions to select from during the process of building spectral files. We usually build one spectral file for the needs of one study, or one that handles the longwave calculation and another that handles the shortwave part, as their generation can be demanding on both time and resources. Indeed, during the generation, opacity coefficients are computed in each spectral band for each point included in a predefined pressure-temperature grid. The runtime and computer resources needed increase with the spectral resolution and the resolution of the pressure-temperature grid.

The inputs of SOCRATES are the quantities related to the temperature profile: the pressure and temperature at the layer edges and centres, as well as the mixing ratios of each species included. These, as well as the spectral file, are input using netCDF[3] utilities in the call to SOCRATES. The model then outputs radiances, fluxes and temperature tendencies.

Adding the water vapour continuum in the spectral file was one of the first issues encountered, and was caused by software issues arising from the specific formatting of input files and the fact that the MT_CKD water vapour continuum is treated in a very different way from collisional continua such as the H2-H2 CIA. HITRAN does not provide any water continuum like for other species. We have to use other

---

[3] http://www.unidata.ucar.edu/software/netcdf/

resources, such as CAVIAR (Ptashnik, McPheat, Shine, Smith, & Williams, 2011) or, what I chose, the self-broadened MT_CKD continuum. Additionally, the way to include this continuum in the spectral files is different from other CIA files, for instance because different flags are needed, e.g. -e and -k instead of -CIA, and specific parameters are required by the MT_CKD continuum, such as a line cut-off of 2500 m^{-1}.

While generating my own spectral files, I discovered a group of syntactic properties that SOCRATES makes use of, important to properly communicate with the source code from the Python interface we use to generate spectral files. There are special syntax rules in the naming of auxiliary output files, to specify the total number of bands, the number of bands used for a specific data file, or which pressure-temperature table file to input. The patterns resulting from these rules are read and recognised by the source code. This has been critical to understand how the generation of new files is done, notably to introduce the MT_CKD foreign-broadened continuum absorption of water vapour.

Also relating to the continuum, there is an important distinction between Block 8, which is associated with the old way of introducing continua, and Block 18, a newer and more flexible way of introducing them. The "generalised continuum" and the "old continuum", that Blocks 18 and 8 respectively handle, are different numerical parameterizations of continuum absorption. The "generalised continuum" is based on calculating k-tables for continuum absorption, while the "old continuum" involves fitting some functions to approximate the continuum absorption. To introduce different types of continuum absorption like the MT_CKD continuum for water vapour or various types of Collision-Induced Absorption (CIA) for other molecules, we therefore use Block 18.

Another potential issue that can arise in some cases is the fact that, in non-dilute cases, if we have a dominant absorber among other species, its self-broadened continuum will be important and depend on its concentration, and the spectral file would require taking this into account. This is done by adding a parameter space of concentrations on top of the wavenumber, pressure, and temperature parameter spaces. Runaway greenhouse atmospheres are an example where this would be an important consideration, except in the pure steam limit. This is an important issue for mixed atmospheres with multiple abundant absorbers, for instance with 50% H_2O and 50% CO_2, or 50% H_2O and 50% H_2, and would arise if the composition of the atmosphere varies in time, or with altitude, because of condensation for instance. If the concentrations of absorbers are constant as a function of time and height, they are just specified and the issue can safely be ignored. Additionally, in dilute cases, where the self-broadened continuum is not as important, k-coefficients for mixtures of gases can be computed on the fly without the spectral file needing a separate entry for each gas concentration.

We have not yet introduced this dependence on absorber concentration in the spectral file generation, both because our work on the pure steam limit has not yet required it, and because the runtime of a spectral file generation with this additional parameter space would be multiplied by the number of gas fractions introduced. Unless we have some clues about the atmospheric composition of the planet under study to constrain this number, we would have to explore the whole concentration parameter space from 0 to 1. In the case of a CO_2-dominated atmosphere though, like the one on Mars or Venus, we could limit the exploration to a couple of values close to unity.

I worked alongside the UK Met Office, mainly with Dr. James Manners, to fix codebreaking issues present in the SOCRATES source code that caused NaNs and other errors to appear when generating spectral files. As an example, I noticed an issue that several people in my group were having. We had been getting NaNs in the spectral files produced by SOCRATES, specifically in Block 19 corresponding to the collision-induced absorption. The .par files from HITRAN did not cause any NaNs in Block 5, which deals with the line absorption. I tested the CO2-CO2 and N2-N2 CIA data files as well as the water vapour MT_CKD 3.0 self-continuum, and each caused their own sets of NaNs in Block 19 of the resulting spectral file.

"Ccorr_k" and "prep_spec" are two Fortran utilities that are used to write spectral files, the former to compute coefficients, and the latter to edit blocks. For N2-N2 for instance, the call to Ccorr_k followed by prep_spec in my Python script was as follows:

```
f.write(’Ccorr_k -F pt_cont -CIA N2-N2_2018.cia -R 1 9 -c 2500.0 -i 1.0 -ct 13 13 1.0e2 -t 1.0e-2 -k -s sp_file +p -lk -o n2_cia_o -m n2_cia_m -L n2_cia_lbl.nc’ + ’\n’)
```

```
# Add to spec file with prep_spec
f.write(’prep_spec «EOF’+ ’\n’)
# Select spectral file
f.write(’sp_file’+ ’\n’)
# Append
f.write(’a’+ ’\n’)
# Select block 19 (CIA data)
f.write(’19’+ ’\n’)
# Select data
f.write(’n2_cia_o’+ ’\n’)
f.write(’-1’+ ’\n’)
f.write(’EOF’+ ’\n’)
```

This generated NaNs in Block 19 as well as in the auxiliary file n2_cia_o. I suspected that these NaNs were indicative of an issue in the call to Ccorr_k. I wondered if SOCRATES considered NaNs in this block as zeros, but Dr. Manners told me it did not, and that the NaNs would be causing problems in the model runs where the CIA is used. I then investigated whether the NaNs were caused by a lack of data in the corresponding bands of the CIA file itself. It wasn't the case. I also checked whether the NaNs only occurred for bands that overlap the edges of the data, but they were also present in bands that were wholly included in the spectral range of the data. It eventually turned out that the NaNs were caused by zero and negative values of absorption not being captured correctly in the corr_k code. The N2-N2 CIA file from HITRAN contains blocks of negative values, and is not continuous in wavenumber range. We wanted to make sure that the code could handle this properly. Dr. Manners opened a ticket in a dedicated development branch of SOCRATES, with the description: "The correlated-k program "corr_k" uses a calculation of the pressure at which the optical depth reaches 1 for a given absorption coefficient. This does not guard against zero absorption coefficients so can produce NaNs in this case. There is also currently no check to ensure absorption coefficients read in from cross-section or CIA data files do not contain any unphysical negative values. This ticket will introduce checks to catch these issues and correctly zero the resultant absorption coefficients."

After this was corrected, I noticed another issue that we added to the ticket. Trying to generate a spectral file for H_2O and CO_2, I found an error occurring after the Ccorr_k calls to both h2o.par and co2.par were done, when I called prep_spec to include Block 6, the thermal source, specifically when I input the name of the spectral file. I tried to exclude CO_2, and H_2O alone worked fine, along with its self-broadened continuum. And when I tried with CO_2 alone it also worked. Only a spectral file generation including both H_2O and CO_2 yielded the error. I tried adding the thermal source manually, meaning on the command line instead of the Python script, and when I entered the name of my spectral file the same error appeared. I also noticed something that I thought could be related to the error, "***" symbols beside some k-terms in Block 5. I thought it could be a compatibility issue between the two Ccorr_k calculations. Dr. Manners found that the locations of the "***" symbols are where one can add in an integer to specify a scattering method for a given k-term. This is a hidden feature most of the time, as the Fortran code reads zeros for blank spaces. The problem was that when I added in data for a new gas with more k-terms than had previously been allocated, the extra space was allocated but the scattering method was not set for the extra terms. In my case, there happened to be some memory that wasn't representable as a 3 digit integer, so produced "***". In the development branch of SOCRATES, we defaulted these to zero, which actually tells the code to put blanks in the file.

Once these fixes were introduced to the master branch, we also discovered a few systemic problems through interactions with Prof. Raymond Pierrehumbert, Dr. James Manners, and Dr. David Amundsen. These are Earth-centric parameterizations that will eventually need to be generalised to any planetary context. For instance, the MT_CKD 3.0 foreign-broadened continuum of water vapour simulates collisions between water vapour molecules and dry Earth air, even if we are in an exotic $H_2O - CO_2$ or a $H_2O - H_2$ atmosphere. It should ideally be adaptive and account for the chemical composition of the atmosphere. Similarly, the Rayleigh scattering computed by SOCRATES is calculated using fixed scattering cross-sections represented by a constant value in each band determined in the spectral file itself, even though they would actually depend on composition, which may vary in time or with altitude. Until recently, Rayleigh scattering in SOCRATES was due to either Earth air molecules or an H_2/H_e composition, instead of the specific mix of molecules defined by the user. Sometime since then, a new option has been introduced in the prep_spec code to use the custom composition defined by the user in the spectral file.

Another issue investigated was the calculation of the Outgoing Shortwave Radiation (OSR). In principle, as the surface warms up to sufficiently high temperatures, the Planck function shifts toward the visible and ultraviolet range of the spectrum due to Wien's displacement law. As this happens, an increasingly larger amount of radiation emitted by the surface and the air layers above it in these shortwave regions, where water vapour is much less opaque, should escape to space, adding to the total energy lost by the planet. It seemed that SOCRATES did not account for it at the time, as the OSR remained close to 1 $\mathrm{W.m^{-2}}$ as the surface temperature went from 500 to 3000 K. This problem was of a semantic nature. "Shortwave" and "longwave" in SOCRATES are used to refer to the provenance of the fluxes and not their place in the spectrum. "Shortwave" fluxes come from solving for a solar source, and what is called the "longwave" flux comes from the thermal source calculation over both the longwave and shortwave parts of the spectrum. In the band-grey model described in section 4.1, this distinction is made more explicit, and using the opacity coefficients seen on Fig. 5.1, the OSR is defined as the planetary flux in the shortwave regions. It starts to have a significant contribution to the total outgoing radiation after the surface warms up above about 2300 K, as seen in Chapter 5. We also have the option of manually tweaking the opacity coefficients of our explicitly defined shortwave region. As we increase its transparency while staying in a reasonable range of opacity, the OSR can be significant at much lower surface temperatures. Previous papers investigating the energy budget in a runaway greenhouse context, like Goldblatt et al. (2013), Kopparapu et al. (2013), or Hamano et al. (2015), also do not account for the shortwave contribution of the energy loss.

The spectroscopic data for water vapour used in our spectral files comes from HITRAN, which uses measurements done in or close to Earth-like conditions. This introduces some inaccuracy at higher temperatures where the data quickly becomes incomplete and results in inaccurate opacities (Tennyson & Yurchenko, 2017), and though the TOA balance is mostly determined in the upper atmosphere in the cases of this study, some accuracy is still lost when it comes to the behaviour of the deeper layers at temperatures higher than 600 K. HITEMP and ExoMol would be more accurate and more complete datasets to include in the spectral files. Including ExoMol into SOCRATES spectral files requires a new script that is currently being worked on at the Met Office but is not yet ready for testing. Alongside Tim Lichtenberg, we developed a spectral file generation script that could include HITEMP data files. It is ready for use, however the generation of such files turned out to take at least several months of runtime. It likely requires the use of a supercomputer, which we will try in the future.

4.4 Flux contribution function on rocky exoplanets

As mentioned at the beginning of this chapter, we made use of a contribution function computing the amount of flux remaining from each layer at the top of the atmosphere. It was first derived by Drummond et al. (2018) in the context of hot Jupiters, and it has been adapted by Boukrouche et al. (2021) to planets with a solid surface. The expressions for the flux contribution function to the outgoing planetary radiation, $\mathcal{CF}_{\mathrm{F}}$ and the surface flux contribution $\mathcal{SCF}_{\mathrm{F}}$ are:

$$\mathcal{CF}_F = 2\pi\pi B(T(\tau_{12}))\frac{e^{-D(\tau_\infty-\tau_2)} - e^{-D(\tau_\infty-\tau_1)}}{D}, \tag{4.11}$$

and

$$\mathcal{SCF}_F = I_+(0)e^{-\tau_\infty}, \tag{4.12}$$

with $B(T(\tau_{12}))$ the Planck function at the temperature of the layer between τ_1 and τ_2, τ_∞ the optical thickness of the atmospheric column, and D the diffusivity factor defined in Eq. 4.1 and 4.2.

They can be derived in the way described below. We start with the Schwarzschild two-stream radiative equation without scattering,

$$\frac{d}{d\tau_\nu} I_\nu(\tau_\nu, \mu, \phi) = -\frac{1}{\mu}\left[I_\nu(\tau_\nu, \mu, \phi) - \pi B(\nu, T(\tau_\nu))\right], \tag{4.13}$$

with $\mu = \cos(\theta)$ and θ the zenith angle, and ϕ the azimuthal angle. For the rest of the derivation, we will drop the ν indices for clarity. All quantities depend on frequency. We also use the convention that at the top of the atmosphere $\tau = \tau_\infty$ and at the bottom $\tau = 0$. Drummond et al. (2018) uses the opposite convention.

The upward flux then satisfies

$$\mu \frac{d}{d\tau} I_+(\tau, \mu, \phi) = -I_+(\tau, \mu, \phi) + \pi B(T(\tau)), \tag{4.14}$$

which, integrated, becomes

$$I_+(\tau, \mu, \phi) = I_+(0, \mu, \phi)e^{-\frac{\tau}{\mu}} + \int_0^\tau \pi B(T(\tau'))e^{-\frac{|\tau-\tau'|}{\mu}} \frac{d\tau'}{\mu}. \tag{4.15}$$

We then evaluate this expression at the top of the atmosphere.

$$I_+(\tau_\infty, \mu, \phi) = I_+(0, \mu, \phi) e^{-\frac{\tau_\infty}{\mu}} + \int_0^{\tau_\infty} \pi B(T(\tau')) e^{-\frac{\tau_\infty - \tau'}{\mu}} \frac{d\tau'}{\mu}. \tag{4.16}$$

Computing the contribution of a given atmospheric layer $\tau_1 \rightarrow \tau_2$ is done by setting the integration bounds to τ_1 and τ_2. The surface contribution is not the contribution of any atmospheric layer, and thus does not come into the expression of the contribution function. It will instead be dealt with separately. Drummond et al. (2018) assume that $B(T(\tau'))$ is constant over the layer $\tau_1 \rightarrow \tau_2$ of width $d\tau'$. We keep this assumption and define τ_{12} any optical depth in the range $[\tau_1, \tau_2]$.

The contribution of a particular layer $\tau_1 \rightarrow \tau_2$ is then

$$I_+(\tau_\infty, \mu, \phi) = \pi B(T(\tau_{12})) \int_{\tau_1}^{\tau_2} e^{-\frac{\tau_\infty - \tau'}{\mu}} \frac{d\tau'}{\mu}, \tag{4.17}$$

with

$$\int_{\tau_1}^{\tau_2} e^{-\frac{\tau_\infty - \tau'}{\mu}} \frac{d\tau'}{\mu} = \frac{\mu}{\mu} e^{-\frac{\tau_\infty}{\mu}} \left(e^{\frac{\tau_2}{\mu}} - e^{\frac{\tau_1}{\mu}} \right) = \left(e^{-\frac{\tau_\infty - \tau_2}{\mu}} - e^{-\frac{\tau_\infty - \tau_1}{\mu}} \right), \tag{4.18}$$

The intensity contribution function $\mathcal{CF}_I$ is then

$$\mathcal{CF}_I = I_+(\tau_\infty, \mu, \phi) = \pi B(T(\tau_{12})) \left(e^{-\frac{\tau_\infty - \tau_2}{\mu}} - e^{-\frac{\tau_\infty - \tau_1}{\mu}} \right). \tag{4.19}$$

The flux contribution function $\mathcal{CF}_F$ is

$$\mathcal{CF}_F = \int_0^{2\pi} d\phi \int_0^1 \mu \mathcal{CF}_I d\mu, \tag{4.20}$$

Replacing, we get

$$\mathcal{CF}_F = 2\pi\pi B(T(\tau_{12})) \int_0^1 \left(\mu e^{-\frac{\tau_\infty - \tau_2}{\mu}} - \mu e^{-\frac{\tau_\infty - \tau_1}{\mu}} \right) d\mu. \tag{4.21}$$

This is solved with the diffusivity approximation (Thomas and Stamnes (2002), section 11.2.5) providing

$$\int_0^1 \mu e^{-\frac{\tau}{\mu}} d\mu = \frac{e^{-D\tau}}{D}, \tag{4.22}$$

with $D \approx 1.66$ the diffusivity factor.

The $\mathcal{CF}_F$ becomes

$$\mathcal{CF}_F = 2\pi\pi B(T(\tau_{12})) \frac{e^{-D\frac{\tau_\infty - \tau_2}{\mu}} - e^{-D\frac{\tau_\infty - \tau_1}{\mu}}}{D}. \tag{4.23}$$

Assuming that $I_+(0)$ is independent of μ, we get

$$\mathcal{CF}_F = 2\pi\pi B(T(\tau_{12})) \frac{e^{-D(\tau_\infty - \tau_2)} - e^{-D(\tau_\infty - \tau_1)}}{D} \tag{4.24}$$

The surface contribution function is simply the upward flux radiated by the surface attenuated by the entire atmospheric column.

$$\mathcal{SCF}_F = I_+(0) e^{-\tau_\infty}. \tag{4.25}$$

The column-integrated $\mathcal{CF}_F$ should yield the outgoing radiation. Let's integrate it from 0 to τ_∞. First, we express the exponentials in the $\mathcal{CF}_F$ expression of Equation (4.24) as a differential, as

$$\mathcal{CF}_F = \frac{2\pi}{D}\pi B(T(\tau_{12}))de^{-D(\tau_\infty-\tau)}. \tag{4.26}$$

We can solve it by integrating by parts:

$$\begin{aligned}\int_0^{\tau_\infty}\mathcal{CF}_F d\tau' &= \frac{2\pi}{D}\left[\pi\left(B(T(\tau_\infty))e^{-D(\tau_\infty-\tau_\infty)} - B(T(0))e^{-D(\tau_\infty-0)}\right) - \int_0^{\tau_\infty}\pi dB(\tau)e^{-D(\tau_\infty-\tau)}\right]\\ &= \frac{2\pi}{D}\left[\pi\left(B(T(\tau_\infty)) - B(T(0))e^{-D\tau_\infty}\right) - \int_0^{\tau_\infty}\pi dB(\tau)e^{-D(\tau_\infty-\tau)}\right]\end{aligned} \tag{4.27}$$

The outgoing radiation yielded by the Schwarzschild radiative equation is

$$I_+(\tau_\infty) = I_+(0)e^{-\tau_\infty}+\pi\left(B(T(\tau_\infty)) - B(\tau_0)e^{-D\tau_\infty}\right)-\int_0^{\tau_\infty}\pi dB(T(\tau))e^{-D(\tau_\infty-\tau)}, \tag{4.28}$$

which is equal to the integrated $\mathcal{CF}_F + \mathcal{SCF}_F$ except for the $\frac{2\pi}{D}$ factor due to the angle integration and the diffusivity approximation.

4.5 Multispecies adiabat for non-dilute atmospheres

As the investigation on the runaway greenhouse expanded to include a project in collaboration with a team aiming at building a framework coupling atmospheres to magma oceans and planetary interiors, we developed a code allowing for the introduction of a generalised moist adiabatic lapse rate accounting for multiple ideal condensible species at once. The aim was to determine the atmospheric structure and the planetary energy balance given conditions at the magma ocean surface, regardless of the number of species condensing across the column. This requires the thermal profile to be valid in a wide range of dilute and non-dilute regimes. Magma oceans on young terrestrial planets play an important role in the partitioning of volatiles between the interior of the planet and the atmosphere. They are expected to form early on, mainly because of the leftover primordial heat generated by planetary accretion and differentiation during its formation, and the heat produced by the radioactive decay of unstable elements like ^{238}U, ^{235}U, ^{232}Th or ^{40}K. Different volatiles have different solubilities in silicate melts, and the thermodynamical and mechanical properties of these melts, like viscosity, vary significantly over the first millions of years of a planet's evolution, which influences how much volatile content can be stored in the interior, and how much outgasses into the atmosphere. As different volatiles are expelled from the mantle to form a secondary atmosphere, the compositional and thermal structure changes accordingly, which requires taking into account the interplay of multiple volatile gas phases that can condense depending on the local pressure and temperature conditions.

In Lichtenberg et al. (2021), we started using a moist adiabatic lapse rate scheme that we coupled to SOCRATES in order to be used in the SOCRATES-SPIDER framework. SPIDER (Simulating Planetary Interior Dynamics with Extreme Rheology, Bower, Sanan, and Wolf (2018)) is an interior dynamics and energy balance model that handled the melting, cooling, and crystallization of the mantle. The lapse rate scheme, developed by Pierrehumbert (2010), is valid for non-dilute conditions where only one condensible species is present.

$$\frac{d\ln T}{d\ln P} = \begin{cases} \frac{R}{c_{p,i}(T)}, & \text{if } p_i < p_{\text{sat},i} \\ \frac{RT}{L_i}, & \text{if } p_i > p_{\text{sat},i} \end{cases} \tag{4.29}$$

L_i, p_i, and $p_{\text{sat},i}$ are the latent heat, partial pressure, and saturation vapour pressure of species i, respectively. R is the universal gas constant equal to 8.314 J.K^{-1}.mol^{-1}. The thermodynamical properties of the species included, like the critical points, triple points, molecular weights, latent heats etc. are defined according to Pierrehumbert (2010). The heat capacity at constant pressure c_p varies weakly with temperature, and we account for this variation using the Shomate equation defined in the NIST Chemistry WebBook, SRD 69 (Chase Jr, 1998; Cox et al., 1984), along with species-dependent fitting parameters A_{i} up to E_{i} such that

$$c_{\text{p,i}}(\widehat{T}) = A_{\text{i}} + B_{\text{i}}\widehat{T} + C_{\text{i}}\widehat{T}^2 + D_{\text{i}}\widehat{T}^3 + E_{\text{i}}/\widehat{T}^2, \tag{4.30}$$

with $\widehat{T} = T(K)/1000$.

We integrate the lapse rate defined in Eq. 4.29 from the ground up. The surface temperature is given by the uppermost temperature yielded by SPIDER. Alternatively, it can be defined arbitrarily when we wish to use the general adiabat code as a standalone. The profile follows a dry adiabat as long as it stays warmer than the condensation curve of species i. When condensation happens, the slope changes to that of the dew point curve of species i, and the fraction of condensates forming from the condensing gas phase is rained out immediately. This scheme was also modified to include an approximation of a stratosphere, by using the coupling with SOCRATES. The radiation code provides a shortwave heating rate that we use to estimate the position of the tropopause, then we make the layers above this point isothermal, and we run the radiation code again with the new profile. We iterate between the radiation and the adiabatic adjustment to get a stable solution.

The downside of this method is that it can only account for one condensible species at once. Multiple condensibles are needed in some cases however, because over the wide range of pressures and temperatures expected in such an atmosphere, two or more species can condense simultaneously. As an example, Fig. 4.4 shows that for pressures above about 35 bars, there is a temperature interval at which CO_2 and H_2O are both in a liquid phase (red zone). The corresponding temperature intervals can span from 273 K to a maximum of 304.25 K. At lower temperatures, from about 216 K to 273 K, CO_2 will condense into liquid droplets while H_2O will condense into ice crystals, as long as the pressure stays high enough (yellow zone). At even lower temperatures, both will condense into ice crystals (blue zone). Given the high surface pressures and temperatures possible in the evolutionary pathways under study, it seems reasonable to expect the possibility of both water and carbon dioxide condensing at some level in the column.

To the aim of handling multiple condensibles at once, we started developing a new model to generate a generalised pseudoadiabatic lapse rate valid regardless of the diluteness of the atmosphere and the number of species condensing at the same time in any given layer. The model is based on a fully reversible formula introduced by Li et al. (2018) in the context of hot Jupiters and brown dwarfs. The following lapse rate is integrated from the bottom up with a fourth-order Runge-Kutta method.

$$\Gamma_{\mathrm{m}} = \frac{d\ln T}{d\ln P} = \frac{1 + \sum_i \eta_i \beta_i}{\frac{\widehat{c}_{\mathrm{p}}}{R} + \left[\sum_i \eta_i \beta_i^2 + \left(\sum_i \eta_i \beta_i\right)^2\right] / \left(1 + \sum_i \eta_i\right)}, \tag{4.31}$$

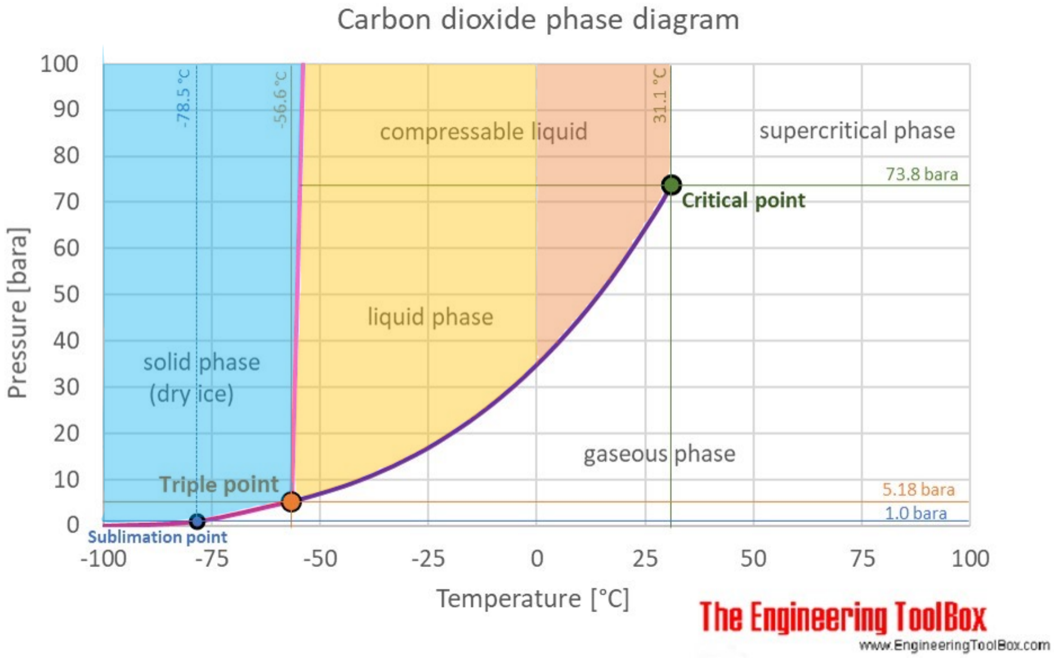

Figure 4.4: Phase diagram of CO_2 adapted from the Engineering Toolbox (`https://www.engineeringtoolbox.com/CO2-carbon-dioxide-properties-d_2017.html`). The red area indicates the range of pressures and temperatures at which both CO_2 and H_2O are in liquid phase. In the yellow area, CO_2 is in liquid phase whereas H_2O is in solid phase. In the blue area both are in solid phase.

with

$$\hat{c}_{\mathrm{p}} = \frac{\overline{c_{\mathrm{p}}}}{x_{\mathrm{d}} + \sum_i x_{\mathrm{v}_i}} = \frac{x_{\mathrm{d}} c_{\mathrm{pd}} + \sum_i x_{\mathrm{v}_i} c_{\mathrm{pv}_i} + \sum_i x_{\mathrm{c}_i} c_{\mathrm{pc}_i}}{x_{\mathrm{d}} + \sum_i x_{\mathrm{v}_i}}. \tag{4.32}$$

The indices d, v, and c respectively designate the non-condensible, condensible, and condensed states of the species with the molar abundance x considered. The η fractions for species i are $\eta_i = \frac{x_{\mathrm{v}_i}}{x_{\mathrm{d}}}$, and in case condensation happens, the latent heat of condensation L_i comes in through $\beta_i = \frac{L_i}{RT}$.

At each atmospheric layer, we check whether the saturation vapour pressure of any condensible species is reached. As long as it is not, the lapse rate is dry adiabatic. Once it is, we saturate the mixing ratio of the condensing species and its partial pressure, and we adjust the temperature to its specific saturation vapour pressure curve. We transfer parts of x_{v_i} condensing into x_{c_i}, keep the condensates in the atmosphere, and perform the integration again with the updated ratios, since changing the partial pressure of one species can affect others.

Equation (4.31) reduces to the Clausius-Clapeyron relation for a single species atmosphere. Looking at equation (4.32), we see that there would be issues in using this equation as it is in specific cases such as when the whole column of a pure steam atmosphere condenses and the scheme is used in a fully reversible setting. Nothing would be left in x_v or x_d, and the formula would break down. It would also be unrealistic to keep all condensates aloft in the atmosphere in non-dilute regimes, because it could create absurd situations. For example, in a pure steam atmosphere, it could generate an ocean of liquid water up high, where vapour condenses. Conceivably, a parcel of this ocean being brought down to lower altitudes would re-evaporate and become positively buoyant again. To avoid such cases, one can switch to the Clausius-Clapeyron formula, or compute the pseudoadiabat by assuming that all condensates rain down instantly and with infinite efficiency, by setting x_c to 0. The latter solution actually yields the correct pseudoadiabat associated to the fully reversible adiadat Γ_{m}. It was the one used in Fig. 4.6, and it was used in the pure steam limit by Boukrouche et al. (2021).

Figure 4.5 displays the behaviour of the general reversible adiabat code in an example atmosphere. The surface temperature is 800 K, and the surface is pressured by 300 bars of $\mathrm{H_2O}$, 100 bars of $\mathrm{CO_2}$, and 1 bar of $\mathrm{N_2}$. Graph A shows the temperature profile in black, p_i is the partial pressure of molecule i, and $p_{\mathrm{sat}}i$ is the individual saturation vapour pressure curve corresponding to species i. Graph B shows the concentration profiles of the gaseous and condensed phases.

From the surface, the temperature profile follows the dry adiabatic lapse rate until

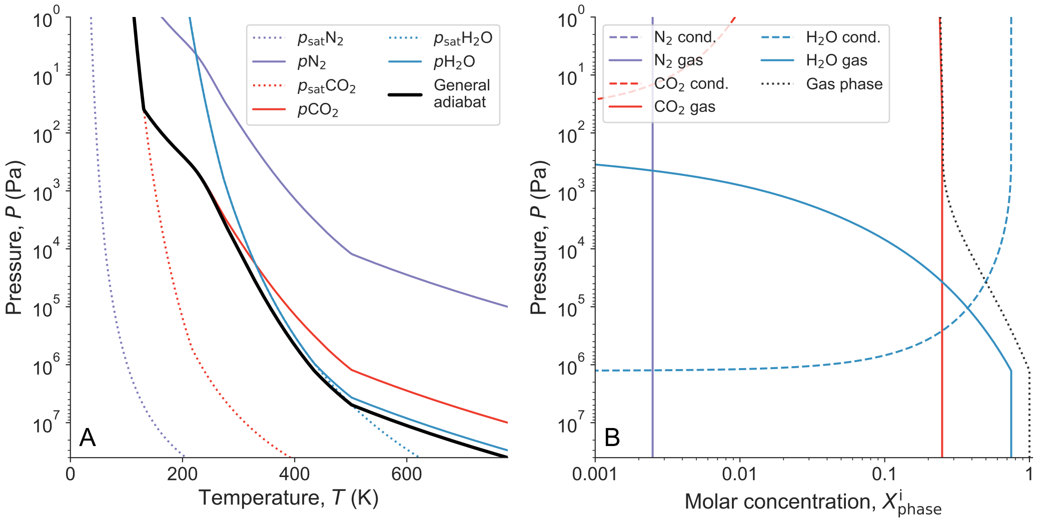

Figure 4.5: Thermal structure computed using the generalised moist adiabat code, in an atmosphere composed of 300 bars of water, 100 bars of CO_2, and 1 bar of N_2. The surface temperature is fixed at 800 K.

it intersects with the Clausius-Clapeyron curve of water vapour at around 50 bars. Then water starts to condense as we can see on graph B, where the concentration of the gas phase of water decreases while that of the condensed phase increases. The profile continues following the dew point of water, slightly diverted from it by the dry CO_2 and N_2. Above about 400 Pa, all the water vapour has condensed, at which point the profile starts following the dry adiabatic slope again. Then, at around 40 Pa, the profile becomes cold enough to condense CO_2, so it follows its saturation vapour pressure curve, and parts of the gas phase of CO_2 is converted to condensed phase. The atmosphere does not run out of CO_2 to condense here, so the profile never gets cold enough to condense N_2.

Figure 4.6 shows the same temperature profile using the pseudoadiabat formulation, zeroing out the concentrations of the condensed phases. The same amount of water condenses and is being rained out instantly, so the slope of the gas phases is the same than in the reversible case.

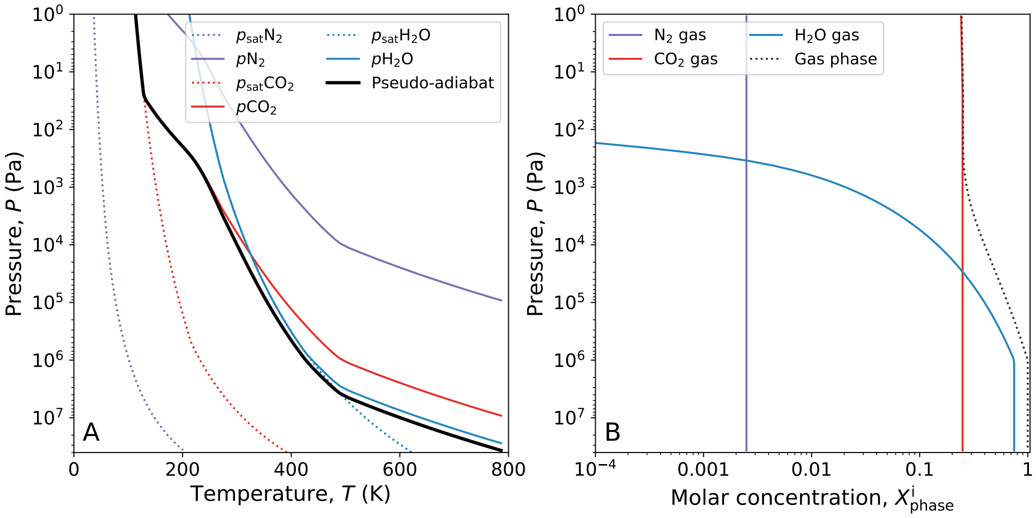

Figure 4.6: Thermal structure computed using the generalised moist pseudo-adiabat code, in an atmosphere composed of 300 bars of water, 100 bars of CO_2, and 1 bar of N_2. The surface temperature is fixed at 800 K.

The problem of the retained condensate fraction mentioned above was addressed in a later publication (Graham et al., 2021) where we included in the formula introduced by Li et al. (2018) a condensate fraction parameter that allows the possibility to control the fraction of condensates retained in a given layer after a species condenses in it. It allows for the resulting adiabatic profile to be fully reversible, pseudo-adiabatic, or anything in between. The corresponding formula is derived in Graham et al. (2021), and the final expression is

$$\frac{d\ln T}{d\ln P} = \frac{x_d + \sum\limits_i x_{v,i}}{x_d \frac{c_d x_d + \sum\limits_i \left(x_{v,i}(c_{v,i} - R\beta_i + R\beta_i^2) + \alpha_i x_{c,i} c_{c,i}\right)}{R\left(x_d + \sum\limits_i \beta_i x_{v,i}\right)} + \sum\limits_i \beta_i x_{v,i}}, \tag{4.33}$$

where α_i is the mole fraction of condensate that is retained in the column instead of raining out for species i.

This scheme has already shown that the lapse rate, and therefore the energy budget of a planet, can be significantly impacted by the choice of the fraction of retained condensates. It will be further developed and improved upon in preparation for subsequent papers that will explore the radiative transfer in mixed atmospheres outgassed by magma oceans, and potentially the non-dilute and supercritical regimes reigning over magma oceans overlaid by a water-dominated atmosphere subject to a runaway greenhouse effect.

5 | 1D results

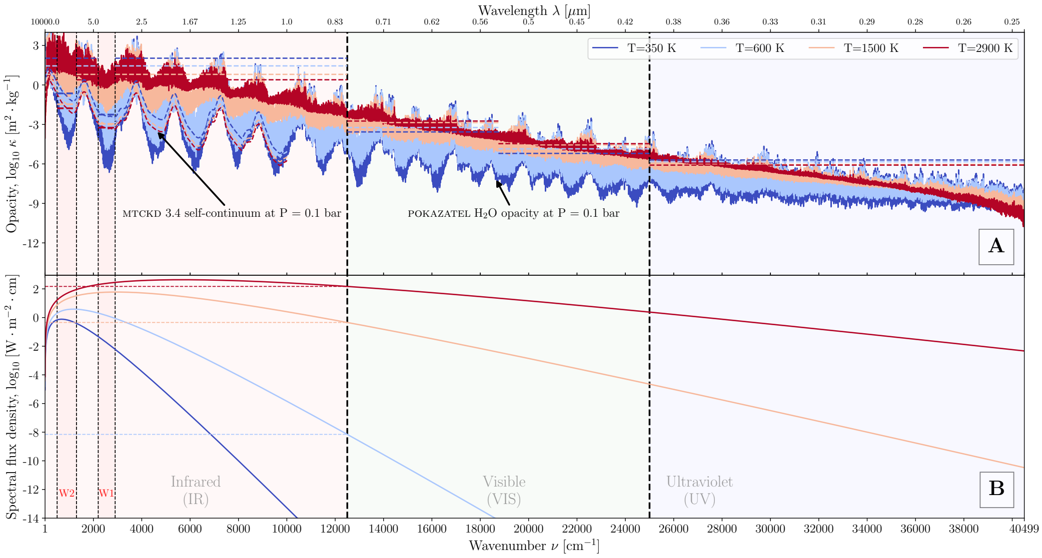

Figure 5.1: **(A)** Water vapour opacity data from the POKAZATEL line list for selected temperatures and a pressure of 0.1 bar. The spectral resolution plotted is 1 cm^{-1}. The MT_CKD 3.4 self-broadened continuum has been superimposed between 1 and 10000 cm^{-1} (dashed coloured lines). Horizontal dashed lines of matching colours represent the mean opacity computed from taking the average between the Rosseland mean and the Planck mean in each specified spectral region, for each temperature. **(B)** Spectral radiance as a function of wavenumber for selected surface temperatures. Horizontal dashed lines mark the intersection of the Planck curves with the visible range of the spectrum. Temperatures higher than ≈2000 K yield significant visible and ultraviolet fluxes. Case with a single shortwave band.

Fig. 5.2 and Panel A of Fig. 5.1 show the opacity coefficient of water vapour between 1 and 45000 cm^{-1}, for 350, 600, 1500, and 2900 K, and for a pressure of 0.1 bar. The calculations of the band-grey model take into account the shortwave regions up to 40500 cm^{-1}, while those of SOCRATES stop at 24500 cm^{-1}. The solid lines show the ExoMol POKAZATEL line list, and the dashed curves between 1 and 10000 cm^{-1} show the MT_CKD 3.4 lines plus self-broadened continuum. Horizontal dashed lines represent the average of the Rosseland means and the Planck

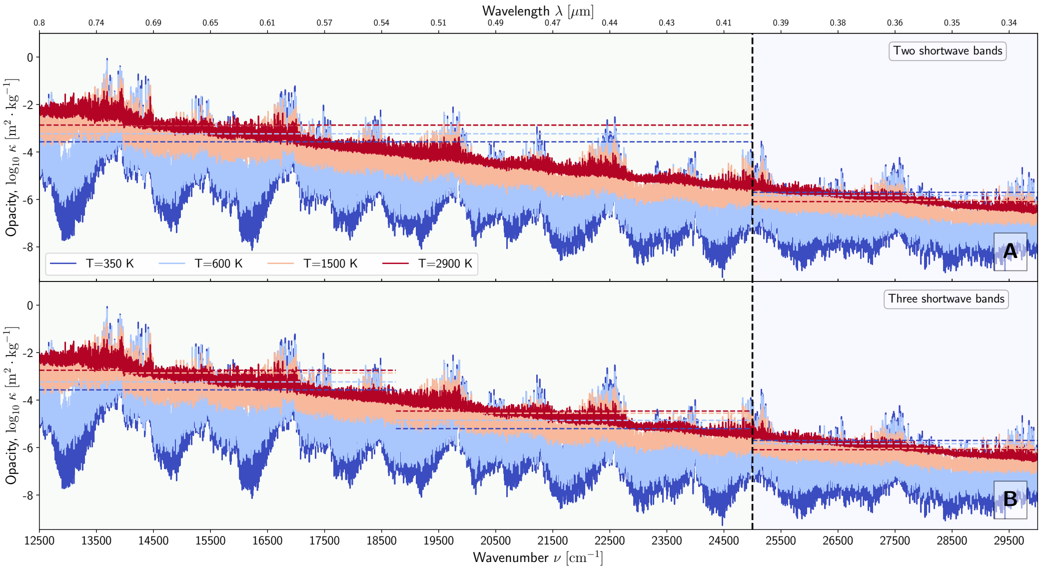

Figure 5.2: Same as Panel A of Fig. 5.1, but focusing on the shortwave part of the spectrum and displaying cases with **(A)** two and **(B)** three shortwave bands.

means computed over each region and for each temperature. They are used in the formation of the band-grey model. Figure 5.1 shows the average as taken by the band-grey model when using a single shortwave band. Fig. 5.2 shows how the average changes when the band-grey model uses two and three shortwave bands. Panel B of Figure 5.1 shows the spectral flux density of a blackbody for each temperature. Intersections of the Planck curves with the beginning of the visible range of the spectrum are shown as horizontal dashed lines, which gives an impression of the contribution of shortwave regions with higher temperatures.

It is important to note that what is often called outgoing "longwave" radiation actually refers to the total thermally emitted radiation coming out of the planet, which includes the shortwave parts of the spectrum up to 40500 cm^{-1} in the case of the calculations presented in this work. Since we define explicit "infrared" and "shortwave" regions in our band-grey model, and because at the high temperatures we work with, the terms "longwave" and "shortwave" as they are often understood can be misleading, we will refer to this total outgoing radiation as Outgoing Planetary Radiation (OPR) in both models, meaning that the name will account for the provenance of the radiation instead of its place on the spectrum. Similarly, the incoming "shortwave" radiation will then be the Incoming Stellar Radiation (ISR).

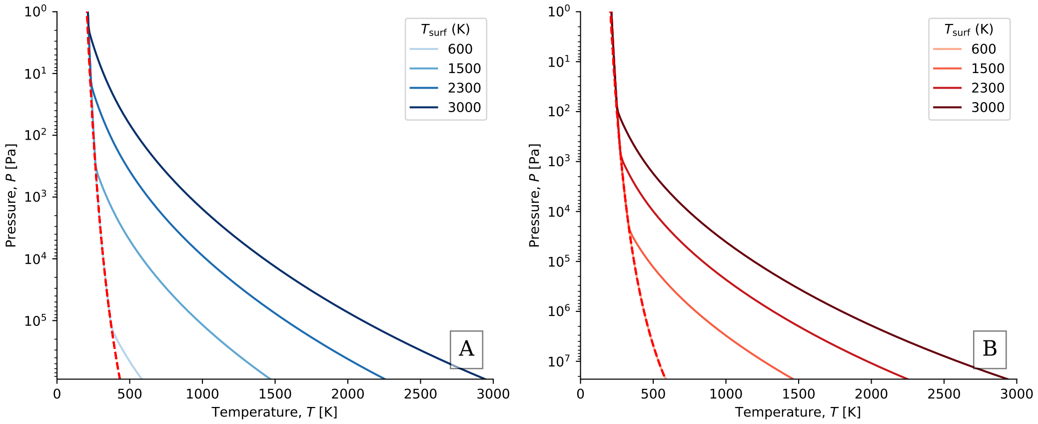

Figure 5.3: Temperature profiles used in the band-grey model and in SOCRATES for selected surface temperatures, at a surface pressure of **(A)** 10 and **(B)** 260 bars. The dashed red line is the Clausius-Clapeyron curve of water vapour.

Figures 5.4 to 5.7 shows the results of simulations performed with the SOCRATES suite and with the band-grey model, in the pure steam limit. A surface pressure of 260 bar was chosen to reproduce the curves obtained by Kopparapu et al. (2013), Goldblatt et al. (2013), and Hamano et al. (2015), visible on Figures 5.8, 5.12, and 5.13. We added a surface pressure of 10 bar to provide a sense of the impact of surface pressure on outgoing radiation. A surface pressure of 10 bars in a post-runaway atmosphere corresponds to a planet with a limited water inventory (about 5% of Earth's), or a planet that has lost most of a more massive ocean through photolysis, hydrogen escape, and geochemical sinks of oxygen.

Figures 5.3A and B show the temperature profiles from which fluxes were computed, for four selected surface temperatures of 600, 1500, 2300 and 3000 K, and

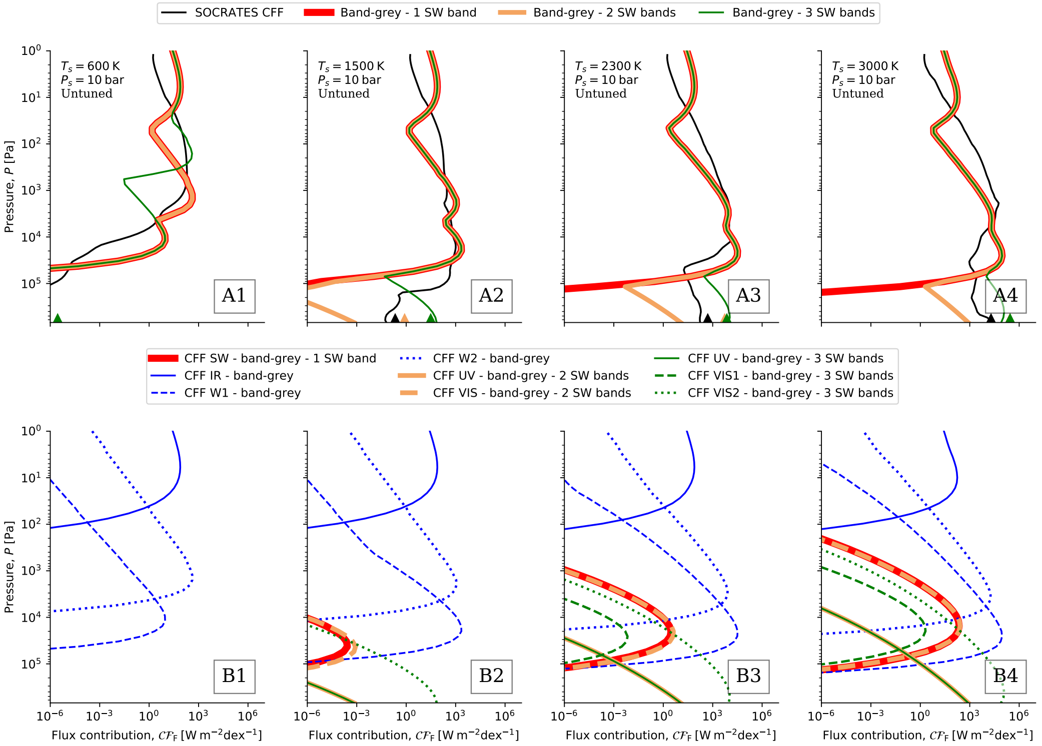

Figure 5.4: Pressure as a function of the flux contribution function $\mathcal{CF}_\mathrm{F}$ to the OPR, for a surface temperature of **(A1/B1)** 600K, **(A2/B2)** 1500K, **(A3/B3)** 2300K, **(A4/B4)** 3000K. The $\mathcal{SCF}_\mathcal{F}$ is shown as triangle markers. On the first row, the $\mathcal{CF}_\mathrm{F}$ is summed over all bands. On the second row, the band-grey $\mathcal{CF}_\mathrm{F}$ is decomposed bandwise and the SOCRATES curve is not included. Cases using one, two, and three shortwave bands are compared. The surface pressure is 10 bar and the band-grey shortwave opacities are not tuned.

for a surface pressure of 10 and 260 bar, respectively. The saturation vapour pressure curve for water vapour, $p_{\mathrm{sat,H_2O}}$, is shown as a red dashed line, superimposed by the thermal profile with the smallest surface temperature.

Figures 5.4, 5.5, 5.6, and 5.7 show the profile of the flux contribution function to the outgoing planetary radiation, $\mathcal{CF}_\mathrm{F}$, along with the surface flux contribution $\mathcal{SCF}_\mathrm{F}$, for the same selection of surface temperatures and surface pressures. It computes how many watts per square meter each atmospheric layer contributes to the top

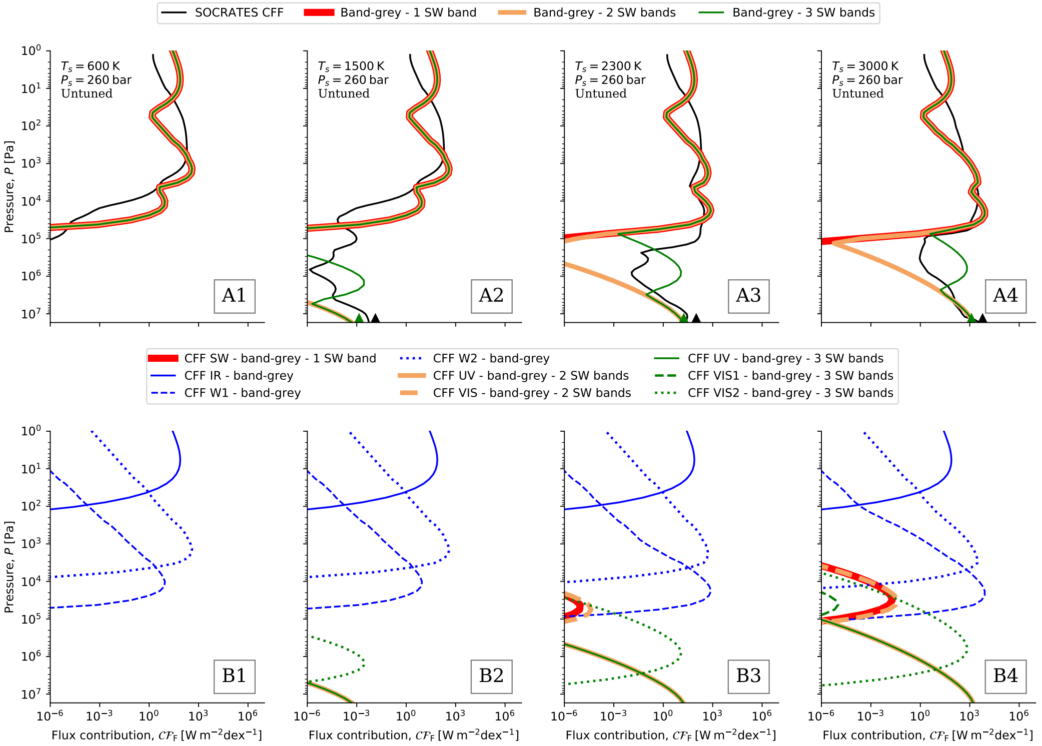

Figure 5.5: Same as Fig. 5.4, but in this case the surface pressure is 260 bar and the band-grey shortwave opacities are not tuned.

of atmosphere (Drummond et al., 2018). The upper panels show the total $\mathcal{CF}_\mathrm{F}$, summed over all spectral bands. The blue curves in these panels show the results of simulations performed with the SOCRATES suite in the pure steam limit. The corresponding band-grey simulation results are shown in red, orange, and green lines, when using a single shortwave band, two, or three, respectively. The $\mathcal{SCF}_\mathrm{F}$ is also plotted as triangles of the corresponding colour. The lower panels show a bandwise decomposition of the $\mathcal{CF}_\mathrm{F}$ obtained with the band-grey model, which allows an easy distinction of $\mathcal{CF}_\mathrm{F}$ by spectral region. Figures 5.4 and 5.5 show baseline cases, at surface pressures of 10 bar and 260 bar respectively, where the averaged shortwave opacity coefficients used in the band-grey model have not been tuned. Figures 5.6 and 5.7 show cases where the shortwave opacity coefficients

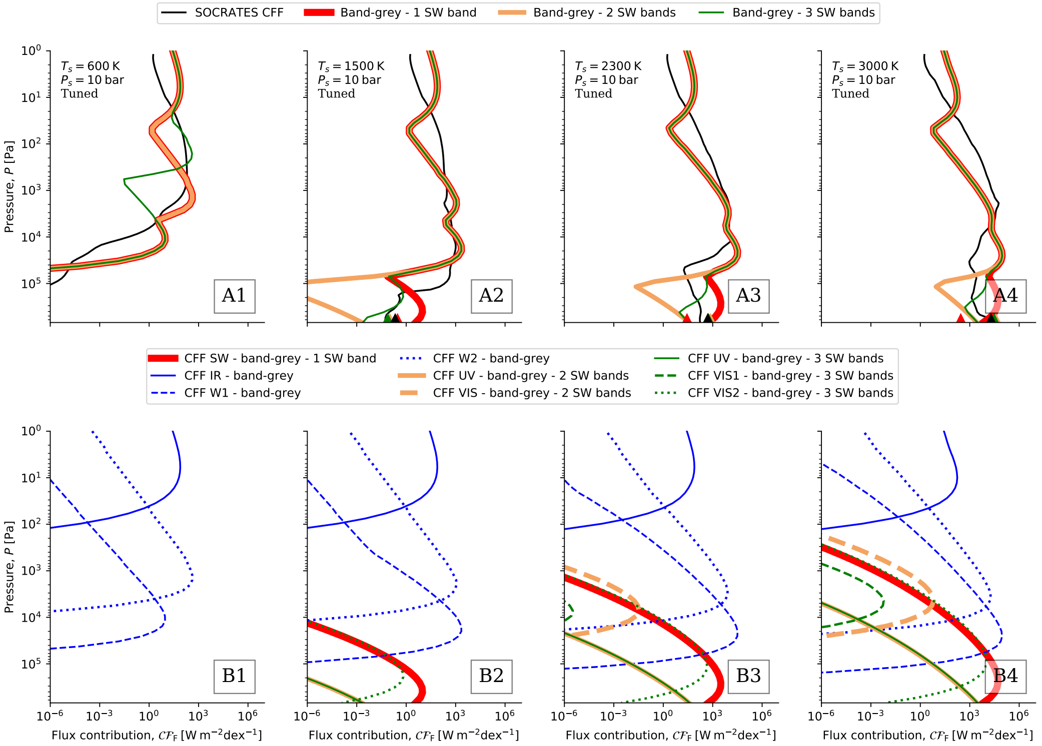

Figure 5.6: Same as Fig. 5.4, but in this case the surface pressure is 10 bar and the band-grey shortwave opacities are tuned to the SOCRATES outgoing planetary radiation.

of the band-grey model have been manually tuned to match the outgoing planetary radiation obtained with the SOCRATES suite. The tuning coefficients used in each band and at each surface pressure can be seen in Table 5.1.

At a surface temperature of 600 K, all three band-grey cases explored here follow the behaviour that SOCRATES yields, and the atmosphere at pressures higher than 1 bar does not contribute to the outgoing planetary radiation in any of the cases explored. The $\mathcal{CF}_\mathrm{F}$ increases with height and peaks at about 400-1000 Pa, which sits comfortably within the moist convective zone. The two windows of water vapour accounted for are more transparent, and therefore bring down the peak relative to what the IR region alone would yield. They also create a secondary peak at about

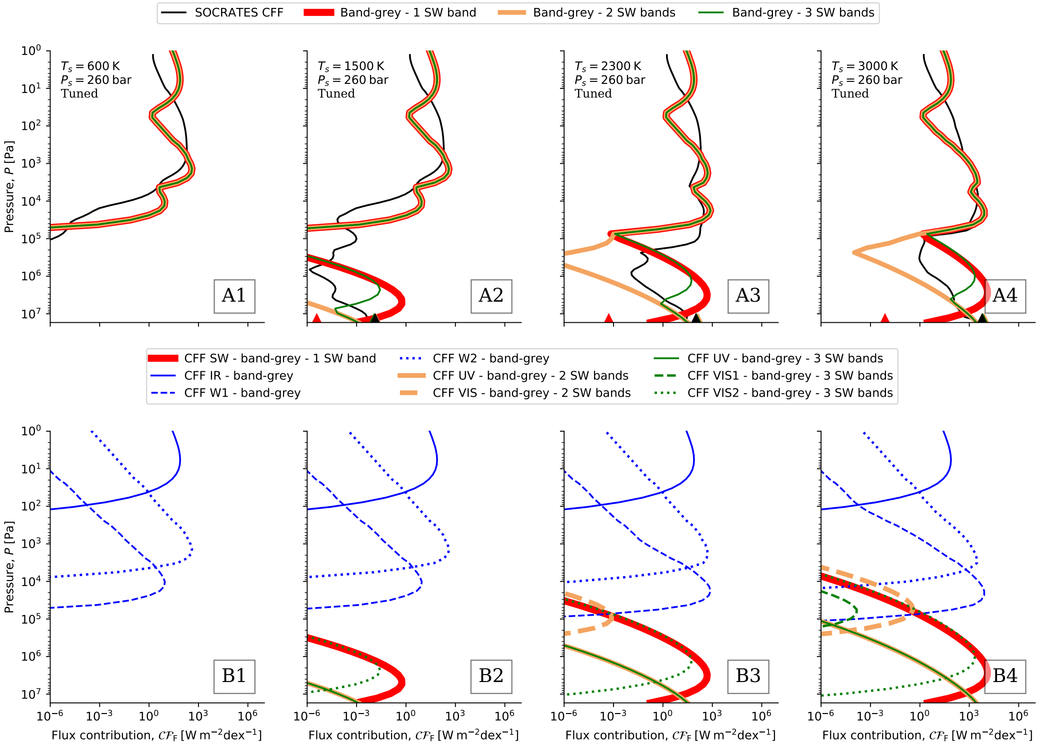

Figure 5.7: Same as Fig. 5.4, but in this case the surface pressure is 260 bar and the band-grey shortwave opacities are tuned to the SOCRATES outgoing planetary radiation.

0.1 bar, due to the bluest window region, W1. Different spectral regions contribute to the OPR with peaks located at different levels because each region has a different width and opacity, and the Planck contribution varies in each of them. The cases with one, two, and three shortwave bands are superimposed as the shortwave contribution is negligible at this temperature.

Going up to $T_\mathrm{s} = 1500$ K, the atmosphere already contributes a significant amount of energy at subsaturated levels at $p_s = 10$ bar, however at $p_s = 260$ bar, most of the contribution still comes from the moist convective zone, even in the tuned case where the single shortwave band (SW) contribution curve peaks at about 20 bar but stays below $1\ \mathrm{W\,m^{-2}\,dex^{-1}}$. The dex unit is adimensional; it is an order of

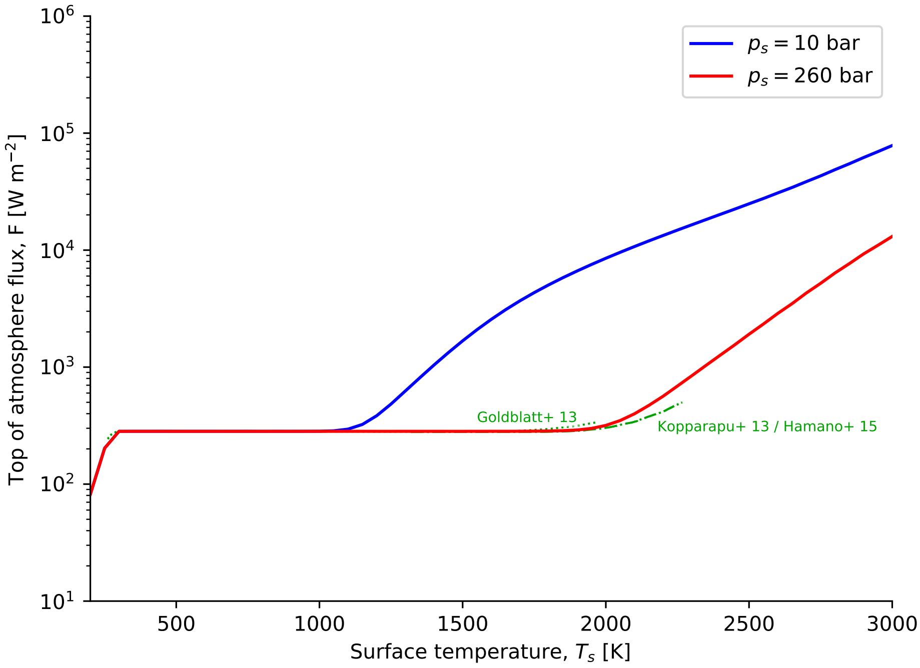

Figure 5.8: Outgoing planetary radiation obtained with SOCRATES for a surface pressure of 10 and 260 bars. Included reference curves from Kopparapu et al. (2013), Goldblatt et al. (2013), and Hamano et al. (2015).

magnitude. A difference of x dex is a change by a factor 10^x. The primary peak due to reddest window region, W2, is relegated to secondary peak, whereas the previous secondary peak becomes the most important. Both peaks do not move noticeably from the $T_{\rm s} = 1500$ K case, however. The shortwave contribution starts to show near the surface up to a millibar at $p_s = 10$ bar and up to 3 bar at $p_s = 260$ bar. It reaches the surface when we use two or three shortwave bands, but the case with a single shortwave band requires tuning to get the shortwave $\mathcal{CF}_{\rm F}$ to do the same. Using three shortwave bands yields a larger shortwave $\mathcal{CF}_{\rm F}$ near the ground than using two.

At $T_{\rm s} = 2300$ K and 3000 K, the shortwave contribution near the ground becomes dominant, overcoming the contribution of the infrared region. This makes the con-

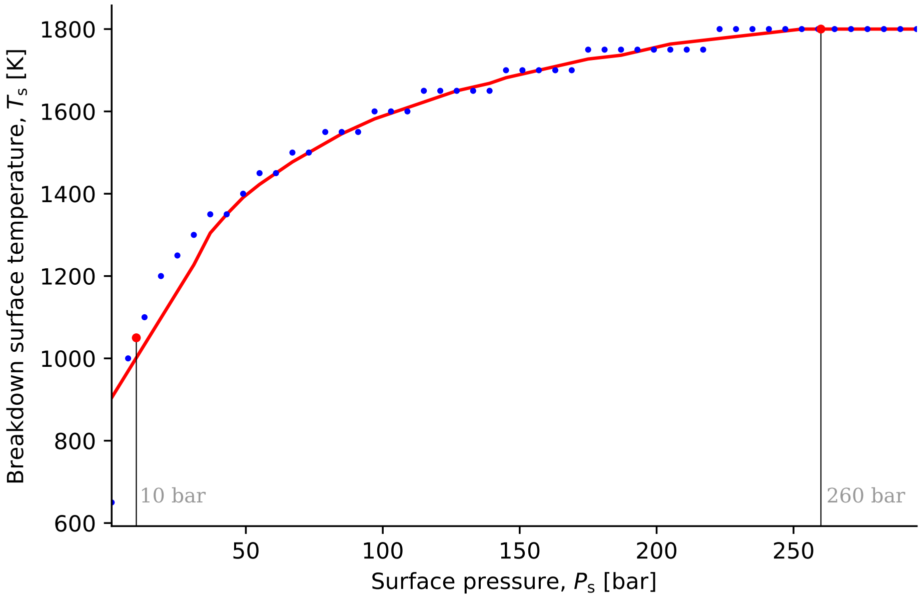

Figure 5.9: Surface temperature at which the OPR increases by 1 $\mathrm{W\,m^{-2}}$, marking the end of the tropospheric radiation limit, as a function of surface pressure. Surface pressures go from 1 to 295 bars, with a step of 6 bars. The discrete data has been smoothed, the result of it showed by a red line. Red dots show the positions of the reference 10 and 260 bar surface pressures.

tribution to the OPR come from both saturated and subsatured parts of the atmosphere. The contribution of the surface itself also becomes important at these high surface temperatures.

Figure 5.8 shows the top of atmosphere energy budget as a function of the surface temperature and for both surface pressures explored on Figures 5.4 to 5.7, 10 and 260 bars.

After an initial increase, the OPR stays flat between 300 and 1800 K in the 260 bar case, and between 300 and 1050 K in the 10 bar case. This flattening represents the familiar limiting "OLR", called the Simpson-Nakajima limit by Goldblatt et al. (2013). In this work, we will refer to it as the ’limiting OPR’, the ’OPR limit’,

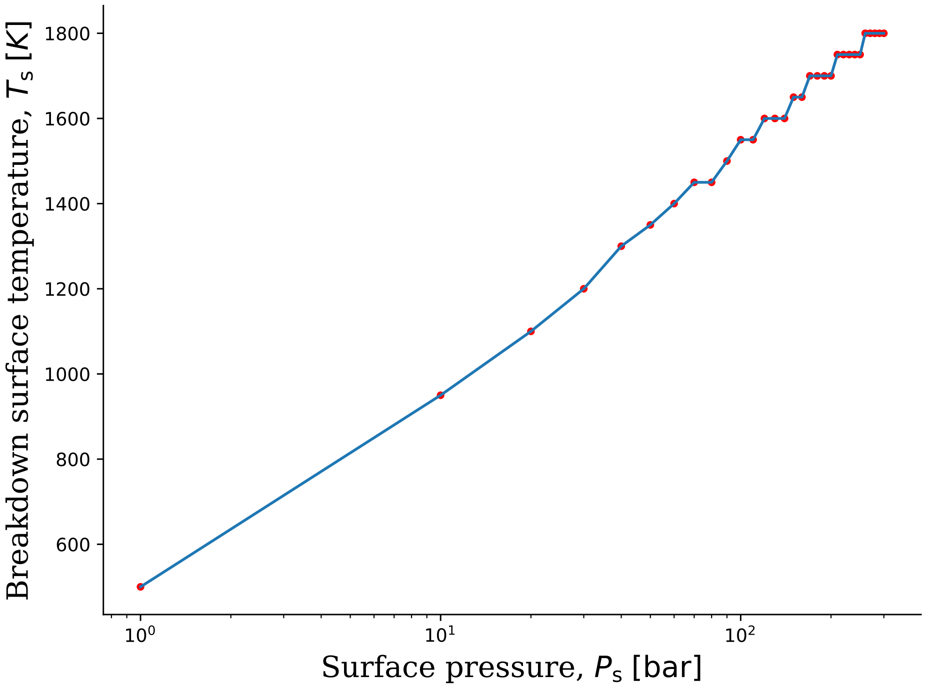

Figure 5.10: Same as Figure 5.9 with the x-axis in a logarithmic scale. Red dot represent the computed values, which are connected with each other by the blue line.

or the 'tropospheric radiation limit', denoted by OPR_∞. It then increases at hotter surface temperatures, almost at an exponential rate. The 260 bar curve fits relatively well the reference curves shown in dotted and dashed green lines, showing that the SOCRATES radiation code, which is widely used in planetary climate studies, can reproduce the OPR limit found in other calculations. The tropospheric radiation limit is about $\mathrm{OPR}_\infty = 283\ \mathrm{W\,m^{-2}}$.

Figure 5.9 shows how the surface temperature at which the outgoing planetary radiation limit breaks down evolves as a function of surface pressure. The blue points are SOCRATES simulations computing the surface temperature at which $\mathrm{OPR}(T_\mathrm{s}) - \mathrm{OPR}_\mathrm{ref} > 1$, with OPR the Outgoing Planetary Radiation and $\mathrm{OPR}_\mathrm{ref}$ a reference OPR value arbitrarily chosen as $282.7\ \mathrm{W\,m^{-2}}$. The temperature at which the limit

Region	$p_s = 10$ bar	$p_s = 260$ bar
SW	$4.6\ 10^{-2}$	$4.23\ 10^{-3}$
UV, VIS	5	$4.9\ 10^{-1}$
UV, VIS1, VIS2	6	$5.4\ 10^{-1}$
IR	0.2	0.2
W1	0.2	0.2
W2	0.2	0.2

Table 5.1: Tuning coefficients used in the band-grey model. When the shortwave region SW is divided into two (UV and VIS) or three (UV, VIS1, and VIS2) subregions, the tuning coefficients between them are the same.

breaks down increases non-linearly with surface pressure and reaches a constant value of about $T_{\mathrm{s,breakdown}} = 1800$ K. The discontinuity of the plot is not a physical effect; it is due to the coarse resolution of the temperature grid used. We use surface pressures from 10 to 300 bar with a step of 10 bar, including $p_s = 1$ bar as the bottom end of the range. The temperatures go from 200 K to 3000 K with a step of 50 K. The distance between two adjacent breakdown surface temperatures decreases as surface pressure increases, as shown by Figure 5.11, and becomes smaller than 50 K when the surface pressure passes about 50 bar.

Even though the OPR limit itself does not depend on the surface pressure, which in turn depends on the mass of the original ocean, the breakdown that allows the OPR to increase again strongly depends on the surface pressure, at least up to about 295 bars. The non-linearity of this increase comes from the non-linearity of the speed at which the intersecting point between the dry and moist adiabats rises, as well as from the non-linearity of the increase in contribution of the Planck function in the shorter waves, as the surface warms up. Figure 5.10 shows the same graph as Figure 5.9 but in a logarithmic scale. The scale change makes it clear that the points follow a logarithmic trend. This agrees with the trend obtained on Figure 3B of Turbet et al. (2019), which extends the range to a hundred Earth oceans.

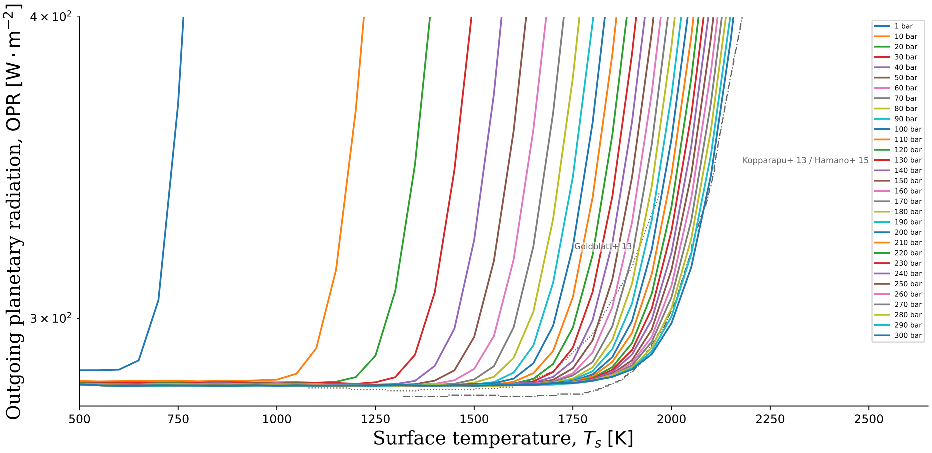

Figure 5.11: Outgoing planetary radiation computed by SOCRATES as a function of surface temperature for a grid of surface pressures.

Figures 5.12 and 5.13 show results from pure-steam simulations using the band-grey model with the same parameters as in Figure 5.8, for $p_\mathrm{s} = 10$ and 260 bar respectively. They show the top of atmosphere radiation budget as a function of the surface temperature. It includes the outgoing planetary radiation in dark blue, which is the sum of the outgoing longwave radiation, plotted in cyan, that comes strictly from the IR, W1, and W2 regions of the spectrum, and the outgoing shortwave radiation, shown in green. In this work, outgoing shortwave radiation refers to thermal shortwave emission, not reflection. Figure 5.12 shows baseline band-grey simulations where the averaged shortwave opacities have not been tuned to the SOCRATES outgoing planetary radiation. The first row of Figure 5.12 uses only one shortwave band, and the shortwave contribution is negligible at all surface temperatures. The second and third rows use two and three shortwave bands respectively. As we can see, using two or three shortwave bands instead of one brings the shortwave contribution up so that the OSR dominates the OLR at $p_s = 10$ bar, with a shortwave-dominated regime starting around $T_s = 2400 - 2500$ K.

Figure 5.13 shows band-grey simulations where the averaged shortwave opacity coefficients have been tuned to match the outgoing planetary radiation yielded by SOCRATES. All three subplots then show similar results. At $p_s = 10$ bar, the OSR becomes significant, almost matching the OLR at $T_s = 3000$ K, and at $p_s = 260$ bar, the OSR exceeds the OLR, defining a shortwave-dominated regime starting at $T_s = 2600 - 2700$ K.

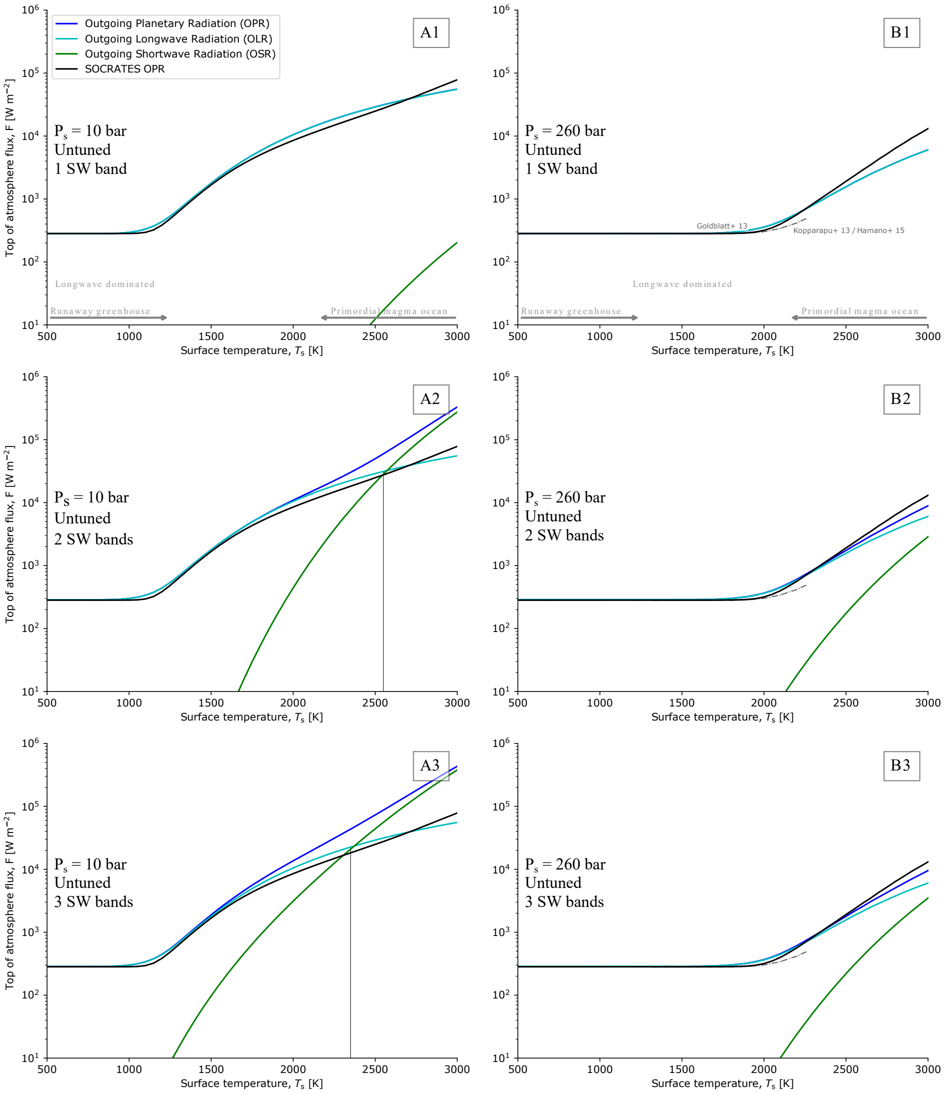

Figure 5.12: Band-grey energy budget at the top of the atmosphere for a surface pressure of **(A)** 10 bars and **(B)** 260 bars in a pure steam atmosphere. The first row uses a single shortwave band, the second uses two, and the third uses three. The dark blue line is the Outgoing Planetary Radiation (OPR), the cyan line is the Outgoing Longwave Radiation (OLR), the green line is the Outgoing Shortwave Radiation (OSR), and the black line is the OPR computed by SOCRATES. The reference curves from Kopparapu et al. (2013), Goldblatt et al. (2013), and Hamano et al. (2015) are plotted in the 260 bar case in the right panels. A black vertical line divides the surface temperature domain into longwave- and shortwave-dominated parts wherever the OSR exceeds the OLR. The tropospheric radiation limit is found at about $\mathrm{OPR}_\infty = 281\ \mathrm{W\,m^{-2}}$. The band-grey shortwave opacities are not tuned.

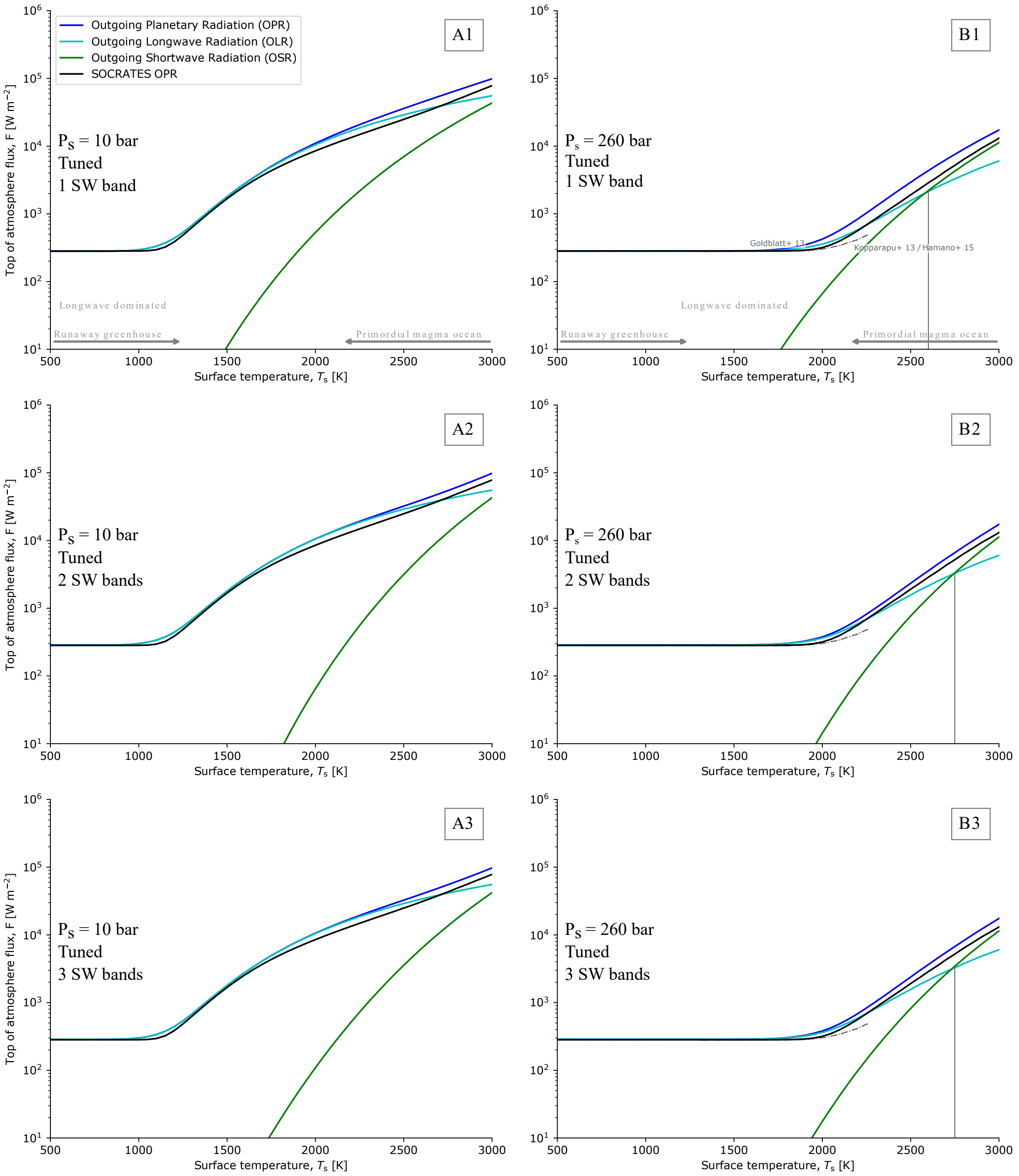

Figure 5.13: Same as Fig. 5.12, but here band-grey shortwave opacities are tuned to the SOCRATES outgoing planetary radiation.

6 | Discussion

The need for tuning the opacity coefficients used in the band-grey model results from the high degree of arbitrariness that averaging over wide spectral regions brings. This is the challenge of handling the shortwave regions when modelled using idealized radiation codes. Averaging over the visible and ultraviolet regions of the spectrum implies ignoring the local variations of the lines, which can lead to an over- or underestimation of the opacity in these regions, depending on the averaging method used. In this work, we tried three cases. The first involves a single shortwave band that includes the visible and ultraviolet regions together. The second has two bands, one that includes the visible range, and the other the ultraviolet range. The third is the same as the second, except that the visible range is split in two bands.

Each addition of a band multiplies the runtime but increases the accuracy of the opacity in each region. This is illustrated by Tab. 5.1, which shows the fact that the tuning coefficients of the shortwave bands become closer and closer to unity as we increase their number. Subdividing the shortwave regions comes down to lessening the need for tuning, meaning that tuning coefficients may get closer to unity, with the limit being using real-gas radiation codes such as SOCRATES, however doing so also increases the runtime significantly.

So long as the outgoing radiation is independent of surface temperature, a planet in a runaway state will continue to get hotter, even after the oceans are completely evaporated. Thus, the factors that eventually allow the outgoing radiation to increase determine the ultimate temperature of the surface, whether a magma ocean forms, and how hot the magma ocean becomes at the surface.

A critical characteristic of the dew-point adiabat derived from the Clausius-Clapeyron relation, Eq. (4.10), is that it is independent of the surface temperature. Therefore, as long as the infrared photosphere of the planet is located at a height where the temperature profile is fixed on the saturated moist adiabat of a pure water vapour atmosphere, the outgoing planetary radiation stays constant as the surface warms up during the runaway greenhouse effect. This has been long recognized as the basis of the tropospheric outgoing planetary radiation limit that gives rise to a runaway greenhouse (Goldblatt et al., 2013; Nakajima, Hayashi, & Abe, 1992; Pierrehumbert, 2010). As the surface warms further, the moist convective zone shrinks and its lowermost reach gets higher and higher until the atmosphere completely aligns with the dry adiabat. When the saturated zone retreats to higher altitudes, increasing the surface temperature can increase the temperature of the radiating layer, because the radiating layer is connected to the surface temperature by a dry adiabat. A separate mechanism is that as lower layers get hotter, they can radiate relatively short waves to space through window regions. This mechanism also relies on the distinction between which part of the atmosphere is on the dry adiabat and which part is on the saturated moist adiabat, since if shortwave radiation from a hot part of the atmosphere can radiate through windows, the radiation to space can only increase with surface temperature if the source region of the radiation is in the dry adiabatic part of the atmosphere.

At first, the whole atmospheric column is fixed on the dew point of water, and any layer emitting near-infrared flux upward would do it at a temperature that will not change with surface warming, because of the lack of dependency of the dew-point adiabat on the surface temperature. Then, in the 260 bar case, at around 2000 K, the contribution function seen on Figures 5.4 to 5.7 begins to be significant, meaning outside of the moist convective zone, around 0.1 bar and to lower pressures as well as near the surface. In the 10 bar surface pressure case, the surface temperature at which the near-surface layers begin to contribute is higher, at about 2300 K. At this surface pressure, we also see the contribution function getting significant at subsaturated levels at 1500 K, while at $p_s = 260$ bar, this happens at surface temperatures of 2000 K and higher. At higher surface temperatures, the peaks of the contribution function become increasingly located at subsaturated levels, which allows the OPR to regain its dependency on the surface temperature. This effect is visible when plotting the outgoing planetary radiation as a function of the surface temperature, as done in Figure 5.8. The surface contribution $\mathcal{SCF}_\mathcal{F}$ derived in section 4.4 is also plotted. At a surface pressure of 10 bar, it is equal to about $7 \cdot 10^{-6}$, $1.3 \cdot 10^{3}$, $1.5 \cdot 10^{5}$, and $1.4 \cdot 10^{6}$ $\mathrm{W\ m^{-2}}$ for surface temperatures of 600 K, 1500 K, 2300 K, and 3000 K respectively. Only the SW band including the visible and UV regions is contributing to these values. The bands IR, W1, and W2 are too optically thick to let the surface emission break out to space. Similarly, at the surface pressure of 260 bar, the $\mathcal{SCF}_\mathcal{F}$ is respectively $1.9 \cdot 10^{-6}$, $3.4 \cdot 10^{2}$, $3.8 \cdot 10^{4}$, and $3.3 \cdot 10^{5}$ $\mathrm{W\ m^{-2}}$. At temperatures where the moist convective zone shrinks enough to allow the dominantly contributing layers to become dependent on the surface temperature, beyond 1800 K at $p_\mathrm{s} = 260$ bar, and beyond 1050 K at $p_\mathrm{s} = 10$ bar, as we saw with SOCRATES, the OPR is able to increase. Our simulations closely align with the reference curves from Kopparapu et al. (2013), Goldblatt et al. (2013), and Hamano et al. (2015). This does not take into account the effect of condensation on radiation, through clouds for instance. Clouds would decrease the level of the radiation limit as well as extend its reach to higher surface temperatures, as Marcq et al. (2017) pointed out, though high altitude clouds would also have a compensating effect in reflecting more incoming stellar radiation back to space.

When the surface warms up to this temperature range and beyond, it starts to radiate increasing amounts of shortwave flux upward, extending to the visible and

UV ranges to some extent. In a pure steam environment where water vapour is the only relevant absorber, fluxes at these wavelengths can escape to space through the vapour without being absorbed as much. As this happens, the peak of the Planck function shifts toward the visible range of the spectrum, as seen on Figure 5.1 B. At about 2000 K the amount of shortwave flux emitted by the surface is on the order of $10\,\mathrm{W\,m^{-2}}$. Assuming the atmosphere is completely transparent to shortwave radiation, the outgoing shortwave radiation would quickly become a significant addition to the outgoing planetary radiation at the top of the atmosphere, and can bridge the gap to a runaway climate state if conditions are already close enough.

While the processes that makes the OPR increase beyond a certain surface temperature are the same as in Figure 5.8, the OSR yielded by the band-grey model and shown on Figure 5.13 increases quite rapidly to dominate the OLR at a surface temperature of about 2730 K at $p_s = 260$ bar (panel B3). Below this threshold, the outgoing energy of the planet is longwave-dominated; above it, it is shortwave-dominated. At $p_s = 10$ bar, the OSR only reaches about 76% of the OLR at $T_s = 3000$ K. Given that the OSR seems to only be dominant at high surface pressures and at temperatures well above 2700 K, these are the conditions that represent the best prospects for observing runaway atmospheres. Lower surface pressures and temperatures would prevent their detection based on the OSR.

This increase has some ramifications for the post-runaway equilibrium state. First, if we assume for instance an incoming stellar radiation of 311 $\mathrm{W\ m^{-2}}$, the value predicted for Earth in one billion years, it reduces the equilibrium temperature of the post-runaway climate by $\approx$ 18 K in the 260 bar case, which is not significant, and does not change it noticeably at all in the 10 bar case. If only the longwave contribution to the outgoing flux is taken into account, the post-runaway equilibrium temperature would be $T_\mathrm{s} \approx$ 1853 K at 260 bar, where the outgoing longwave radiation intersects the incoming stellar radiation when the Earth is 6.067 Gyr old. Taking into account the shortwave contribution, this shifts the equilibrium to T_{s} = 1835 K, where the outgoing planetary radiation intersects the incoming stellar radiation at the same epoch. The instellation received on TRAPPIST-1b is higher, at about 1343 $\mathrm{W\ m^{-2}}$, assuming the bond albedo is 0. In this case, the equilibrium temperature shift becomes $2451 - 2364 = 87$ K at 260 bar. Because the outgoing shortwave radiation increases faster than the outgoing longwave radiation, the shift in equilibrium temperature is expected to increase with the instellation. At 10 bar however, the shift is negligible, suggesting that surface pressure also affects the sensitivity of the equilibrium surface temperature to the shortwave contribution. Rayleigh scattering in the shorter waves would likely reduce the outgoing shortwave radiation, meaning that this cooler equilibrium surface temperature is to be taken as a lower bound. It is worth noting that at the 10 bar surface pressure, the equilibrium surface temperatures are below the solidus temperature of silicates (T_{eq} is found at 1027 K here assuming the same epoch of 6.067 Gyr for the Earth), which means that a solid surface would be able to form and volatile exchange between the atmosphere and the mantle would be reduced.

Both Figs. 5.8 and 5.13 show how the two different types of runaway greenhouse planets approach the transition. Planets right after formation approach the transition from the right and cool down. This means that for planets within the runaway greenhouse limit (Hamano et al., 2013), the equilibrium temperature during the extended desiccation phase may critically depend on the contribution of the shortwave flux. On the other hand, planets that transition from a possibly habitable state to a runaway phase due to increasing instellation over time approach the transition from the left and are similarly affected by the increase in shortwave flux. For both types of magma ocean planets, primordial and secondary, and within or without the runaway greenhouse limit, the contribution of the shortwave flux and the aforementioned radiation throughout the whole spectrum needs to be considered for future surveys that aim to detect and characterize such magma ocean planets (Bonati, Lichtenberg, Bower, Timpe, & Quanz, 2019; Lupu et al., 2014).

The initial volatile inventory of the planet plays a critical role in its evolution. A runaway atmosphere does not start off at the pure steam limit, but approaches it as the water vapour feedback runs its course, however this is assuming that the planet starts off with a large enough initial water reservoir. If not, then the atmosphere may never reach the pure steam limit or even the non-dilute limit, in which case it will not undergo the positive water vapour feedback loop leading up to planet's desiccation. The question of what happens before then, including what might happen if the water inventory is at, say, 1% of an Earth ocean, warrants further study. With a sufficiently low surface pressure, the equilibrium surface temperature can be low enough that a magma ocean does not form, unless the instellation is very high.

The transition from the runaway to the post-runaway stage is important to understand since it likely marks a dominant evolutionary phase in the history of the rocky exoplanet population, with major implications for their present-day climate, total volatile inventory, and observable features in the atmosphere. Here, we utilized 1-D radiative-convective climate simulations in order to explore this transition phase.

Firstly, we explored the change in the main radiating level as a result of an increase in surface temperature during a runaway phase. As the surface warms up, the outgoing radiation begins to become dominated from sub-saturated parts of the atmosphere that follow the dry adiabatic lapse rate, which depends on the surface temperature. Surface warming therefore heats up these atmospheric layers, which increases their contribution to the outgoing radiation.

Secondly, we used a computationally efficient band-grey model with similar settings to evaluate the contribution of the shortwave flux to the outgoing planetary radiation and reproduce the key features of the full correlated-k model. The flux contribution function is a useful tool that can highlight the parts of the atmosphere that determine the outgoing planetary radiation. For moderate temperatures, the outgoing planetary radiation mostly originates from the upper 10 mb of the atmosphere, indicating the need for adequate vertical resolution in this part of the atmosphere for GCM studies. Surface temperatures above the silicate liquidus, during magma ocean stages in the post-runaway regime, will make the surface and the lower atmosphere radiate in the visible and ultraviolet parts of the spectrum. This may reduce the post-runaway equilibrium temperature of the planet with increasing instellation, and affect the shape of the atmospheric spectrum.

Future astronomical observations sensitive to the shortwave regions may probe both the reflection of stellar radiation and innate shortwave radiation from the planet itself. Figure 6.1 superimposes on the domain covered by the band-grey model the spectral range of a few active and upcoming instruments that could observe potential runaway planets in photometry or spectroscopy. For instance, combined observations with ESPRESSO and the recently launched James Webb Space Telescope (JWST) could help discriminate the drivers of the complex wavelength-dependent thermal evolution of such planets.

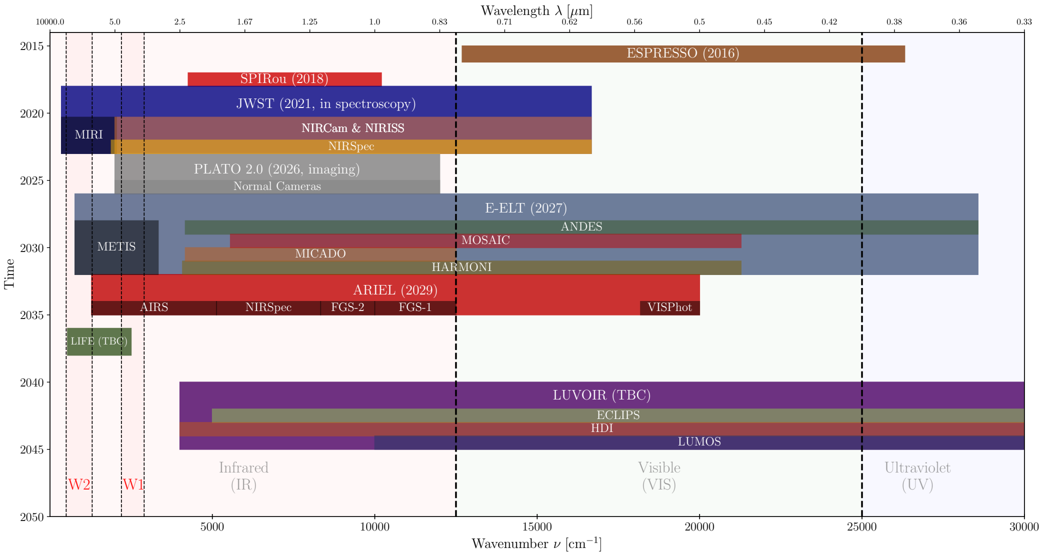

Figure 6.1: Spectral ranges of different observatories. The ECLIPS and HDI instruments of LUVOIR were expected to cover the ultraviolet regions up to 200 nm, and the current design for LUMOS was to reach 100 nm, exceeding the shortwave range of this graph.

7 | Simulating the runaway greenhouse effect in 3D

Exo-FMS is a Global Climate Model (GCM) based on the Princeton Geophysical Fluid Dynamics Laboratory (GFDL) Flexible Modelling System (FMS). It is described at length and benchmarked for gas giant planetary atmospheres by Lee et al. (2021). Here we will give a shorter description, then present the different modifications and improvements made to it during this work.

The dynamical core of Exo-FMS is the GFDL Finite-Volume cubed-sphere dynamical core (FV3). It uses a cubed-sphere geometry, illustrated by Figure 7.1, which avoids the usual singularity issues at the poles that latitude-longitude-based grids intrinsically have.

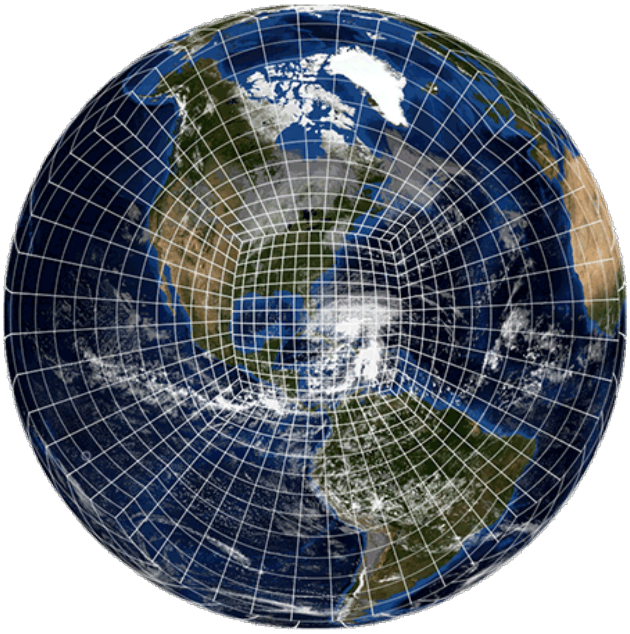

Figure 7.1: The cubed-sphere geometry used by the FV3 dynamical core, taken from `https://www.gfdl.noaa.gov/fv3/`.

Boukrouche, Hammond, and Innes (in prep.) are revamping the framework of Exo-FMS around its dynamical core with three main goals:

- To make the use of Exo-FMS significantly easier and more intuitive for new users.
- To introduce new physics modules in a clean and well-structured way while including existing modules in this new structure.
- Publish another benchmarking study for hot Jupiters, Earth, and warm rocky planets.

7.1 Collaborative development

The first goal involved rewriting the hierarchy of modules that call the physics routines. This change was initiated by Dr. Mark Hammond, and was continued by him, Hamish Innes, and me using the version control system and management tools provided by GitHub. It greatly clarified and simplified the process of running the model. The runscript file, exofms-runscript-writer.py, is now the only file the user needs to edit before starting a new run, unless new quantities need to be output by the model, or the existing modules need to be expanded or otherwise improved. All parameters and model settings are now centralised in this file, to be communicated to the correct auxiliary ones from there.

Notably, we coupled to the GCM three different semi-grey radiation modules and I added the band-grey model I developed, as described in the next section. A simple boundary layer scheme was also added by Mark Hammond to couple the surface temperature and the temperature of the bottom layer in the time stepping scheme. Hamish Innes has also added a preliminary alteration of the dynamical core to account for non-dilute dynamics, notably through a variable isobaric heat capacity with temperature, which will soon be testable. I added extensive amounts of comments to each file to make them readable by new users. Another improvement I brought to the model is in the way it communicates with the NetCDF tools that provide the final output data files. There are now specific routines that the user can call to automatically register the diagnostic fields of the various physics schemes and send them to NetCDF, for two- or three-dimensional quantities. This is the only other place that would need editing before a new run, besides the runscript, in the case where new quantities need to be output.

I made the model use by default a dry adiabatic adjustment on midpoint levels to output a temperature tendency due to dry convection in Kelvin. A debugging tool to check the budget of the dry adiabatic adjustment is also available. It uses the temperature tendency and the pressures at the interface levels to compute the following quantity that should be reduced to zero in hydrostatic balance to ensure dry enthalpy conservation:

$$\int_{1}^{\mathrm{npz}} dT\frac{dP}{g}, \tag{7.1}$$

where npz is the number of midpoint layers, dT the temperature change in K, dP the pressure thickness in Pa, and g the gravitational acceleration in $\mathrm{m\ s^{-2}}$. This expression assumes constant $\mathrm{c_p}$.

I added an optional moist adiabatic adjustment module valid for pure steam atmospheric columns. It outputs a temperature tendency which is the difference between the current temperature and the dew point temperature of water vapour at the current pressure, expressed by Equation 4.10. This is a key difference with the 1D band-grey model described in Section 4.2, in that instead of performing an instantaneous adjustment to the dew point of water, it outputs a temperature tendency associated to the moist adjustment, which is added to the total temperature tendency due to radiation and dry convection. As a part of this work, I also tested different ways to funnel the temperature tendencies into quantities that the model can handle without diverging. The solution we settled on is a convective timescale parameter dividing the tendencies due to convection, fixed at 1000.

The collaborative development of Exo-FMS is still ongoing, and we as a team are periodically meeting and taking on new tasks to complete for the eventual benchmarking study. Eventually, we aim to make Exo-FMS a versatile GCM able to model several types of planets while staying user-friendly. I started the draft of the benchmarking paper with Mark Hammond and Hamish Innes as collaborators.

7.2 Coupling of the band-grey radiation

The collaborative work briefly described in the previous section underpinned my own work on the runaway greenhouse effect. It ultimately allowed the coupling of the band-grey model to the new Exo-FMS framework, as well as comparisons and benchmarking with other radiation models. If a band-grey framework is selected in the runscript, the model calls the necessary routines in the initialisation stage to read and interpolate opacity tables for water vapour in each of the available bands. I made use of the new structure to make the number of these bands accessible from the runscript via the master namelist that we use to communicate parameters from the interface to the different core modules. These bands and the opacity data used for each are the same as the ones described in Section 4.1. Exo-FMS also reads a predefined Planck table to avoid integrating the Planck function with respect to wavelength at every timestep. Then during the time stepping phase, Exo-FMS calls a routine that finds the appropriate opacities given current pressures and temperatures, using bilinear interpolations, and the closest Planck value corresponding to the current temperature. Solving the two-stream equations is done with a different method than the one used in the 1D work. It follows the short characteristics method described by Olson and Kunasz (1987) and Kitzmann et al. (2020) with linear interpolants. It is very fast and stable, and it is accurate at all optical depths except very small ones, around 10^{-6}, due to numerical instability where the linear in τ term gets quite large. At very small optical depths, the code switches to an isothermal layer approximation. The ability to account for scattering of stellar radiation was also added to it, which is a notable addition compared to the version of the band-grey model used for the 1D work, however for the 3D simulations presented in this thesis, scattering was neglected. The scheme does not yet contain any ability to account for scattering of thermally emitted radiation, either shortwave or longwave, which is a shortcoming that will be rectified as this scheme keeps being developed. In high-temperature atmospheres, emitted shortwave radiation could scatter significantly and reduce the OPR. Accounting for scattering is therefore a logical and important step for future work.

In semi-grey schemes, the instellation is usually defined as a single value that is used to compute the incoming stellar radiation (ISR). In the band-grey scheme, we could also keep using a single value, but I opted to use a wavelength-dependent instellation. Exo-FMS now has an additional option to partition the stellar flux into any number of bands defined by the band-grey framework. This is done using routines that read the spectrum of the star selected in the runscript and partition its flux across the spectral bands. The stars currently supported are the Sun from Lean and DeLand (2012), the M star GJ551 from Youngblood et al. (2017), and TRAPPIST-1 from Lincowski et al. (2018). Routines read the spectral irradiance of the selected star in $\mathrm{W\,m^{-2}\,Hz^{-1}}$ and its associated wavelength in meters. They then compute the irradiance as well as its fraction relative to the bolometric irradiance, contained in each band. The fractions are then input into the radiation code.

7.3 Model parameters

The goal of this modelling work was to investigate the circulation patterns, condensation regions, and observability of planet targets beyond or near the runaway greenhouse instellation threshold. We chose TRAPPIST-1b and TRAPPIST-1d and ran simulations for as long as time allowed. We assumed both planets to be tidally locked, so that the spin-period, is equal to the orbital period. They are irradiated by the incoming flux of TRAPPIST-1, which, as it is an M star, means that their atmospheres absorb incoming radiation strongly. This can inhibit condensation in the upper atmosphere and perhaps even suppress convection in the lower atmosphere if insufficient radiation reaches the ground to support convection. Various server issues prevented us from finishing longer simulations, however we were able to output results that seemed to have stabilized after different periods of time in most cases. We initialised the surface temperature to values close to the equilibrium values expected from our 1D work.

A parameter that varies between the target planets is the angular velocity, which affects the global dynamics. The Earth, TRAPPIST-1b, and TRAPPIST-1d have different angular velocities, which means different Coriolis parameters. The Coriolis parameter has a strong effect on the nature of the circulation. Planets that have weak Coriolis parameters generally having weak temperature gradients, except perhaps in thin layers of atmosphere near the top or bottom. Figure 7.2 compares the Coriolis parameters of the Earth, TRAPPIST-1b, and TRAPPIST-1d as a function of latitude. The Coriolis parameter is $f = 2\Omega\sin\lambda$. The angular velocity Ω for the TRAPPIST-1 planets were obtained from the orbital periods recorded by Gillon et al. (2017). TRAPPIST-1b and TRAPPIST-1d both rotate more slowly than the Earth assuming they are tidally locked, with TRAPPIST-1d being the slowest rotator. Their Coriolis forces will be weaker as we move away from the equator than they would be on Earth.

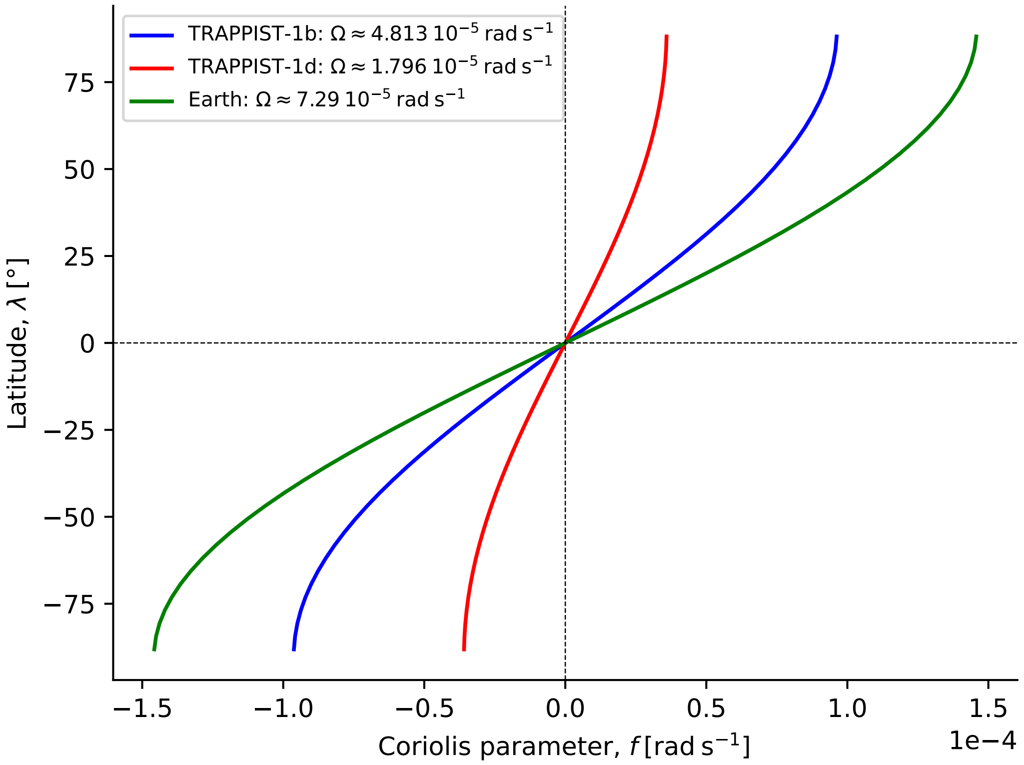

Figure 7.2: Coriolis parameter as a function of latitude for the Earth, TRAPPIST1-b, and TRAPPIST-1d.

Following Pierrehumbert and Ding (2016), the proximity of an atmosphere to the weak temperature gradient (WTG) regime (Pierrehumbert & Hammond, 2019) can be estimated using the ratio Λ of the Rossby deformation radius to the planetary radius. If we assume the atmosphere to be isothermal with characteristic temperature T and that the disturbances introduced by the dynamics have a characteristic length larger than the planetary scale height, we can approximate Λ by an expression that is easier to evaluate,

$$\Lambda = \frac{\sqrt{RT}}{\Omega R_\mathrm{p}}, \tag{7.2}$$

with R the specific gas constant of the dominant species in the atmosphere, T the characteristic temperature of the atmosphere, Ω the angular velocity of the planet, and R_p the radius of the planet. With the parameters shown in Tables 7.1 and 7.2, we can plot the variation of Λ with the characteristic temperature assuming a water-dominated atmosphere. Figure 7.3 shows that using these assumptions, both planets can feature WTG behaviour globally as long as the characteristic temperature of their atmospheres is above 280 K. This is especially the case for the outer planet. This suggests that the temperature through most of the atmosphere may stay close to the 1D average results, so initialising the surface temperature close to the latter would be a reasonable way to speed up convergence. It is worth noting though, that for layers much thinner than the scale height, for instance the condensing layer near the top of the atmosphere, the wave speeds are smaller than the deep-wave speeds, so larger temperature gradients can be supported.

Parameters	TRAPPIST-1b	TRAPPIST-1d	Source
Radius R_p	$1.116 \cdot R_\oplus$	$0.788 \cdot R_\oplus$	Agol et al. (2021)
Semi-major axis a	0.01154 AU	0.02227 AU	Agol et al. (2021)
Orbital period P	1.51 Earth days	4.05 Earth days	Gillon et al. (2017)
Tidal locking	Yes	Yes	Gillon et al. (2017)
Angular velocity Ω	$4.813 \cdot 10^{-5}\,\mathrm{rad\,s^{-1}}$	$1.796 \cdot 10^{-5}\,\mathrm{rad\,s^{-1}}$	Gillon et al. (2017)
Surface gravity g	$1.102\,\mathrm{g} \approx 10.8\,\mathrm{m\,s^{-2}}$	$0.624\,\mathrm{g} \approx 6.12\,\mathrm{m\,s^{-2}}$	Agol et al. (2021)

Table 7.1: Parameters for TRAPPIST-1b and TRAPPIST-1d.

The physical parameters and simulation parameters are shown in Tables 7.1 and 7.2. The run length varies between the six simulations presented in this work, and will

Model parameters	Value	Source (if applicable)
Dynamical and radiative timestep dt	100 seconds	-
Cubed-sphere resolution	25x25 grid points	-
Number of vertical levels	47	-
Gas constant	$461.50\,\mathrm{J\,kg^{-1}\,K^{-1}}$	-
Heat capacity $\mathrm{c_{p,air}}$ at 300 K	$1864\,\mathrm{J\,kg^{-1}\,K^{-1}}$	-
Surface albedo	0	-
Initial surface temperature	1225 K	-
Initial stratospheric temperature	300 K	-
Radiation module	Band-grey with 6 bands	-
Initialised profile	Dry adiabat	-
Luminosity of TRAPPIST-1	$0.000553 \cdot L_{\odot} \approx 2.1 \cdot 10^{23}\,\mathrm{W}$	Ducrot et al. (2020)

Table 7.2: Model parameters.

be seen in the next chapter, in Table 8.1. The model writes outputs every 100 days to improve the resilience of simulation runs and so that runs can be continued and results can be updated if needed. The radiative timestep of 100 seconds was based on test 3D simulations that explored a range of timesteps from 10 to 300 seconds. 100 seconds was found to be small enough to avoid instabilities while being large enough to keep run lengths acceptable. The need to compromise between speed and accuracy in the radiation module, described in Section 3.3 and Chapter 6, played a role in the number of bands chosen. We used the band-grey model in one dimension in part to find a number of bands that would yield comparable quantitative results to the ones obtained with SOCRATES while keeping the runtime of subsequent GCM simulations in three dimensions reasonably short. We therefore kept the framework of six bands capturing the infrared region, two important infrared windows of water vapour, the visible range split at 500 nm, and the UV region. A systematic study of the run speeds using increasingly more bands including other atmospheric windows and subdividing the visible or UV regions further could be considered. Conceivably, this could indicate whether a sweet spot exists where an increase in the number

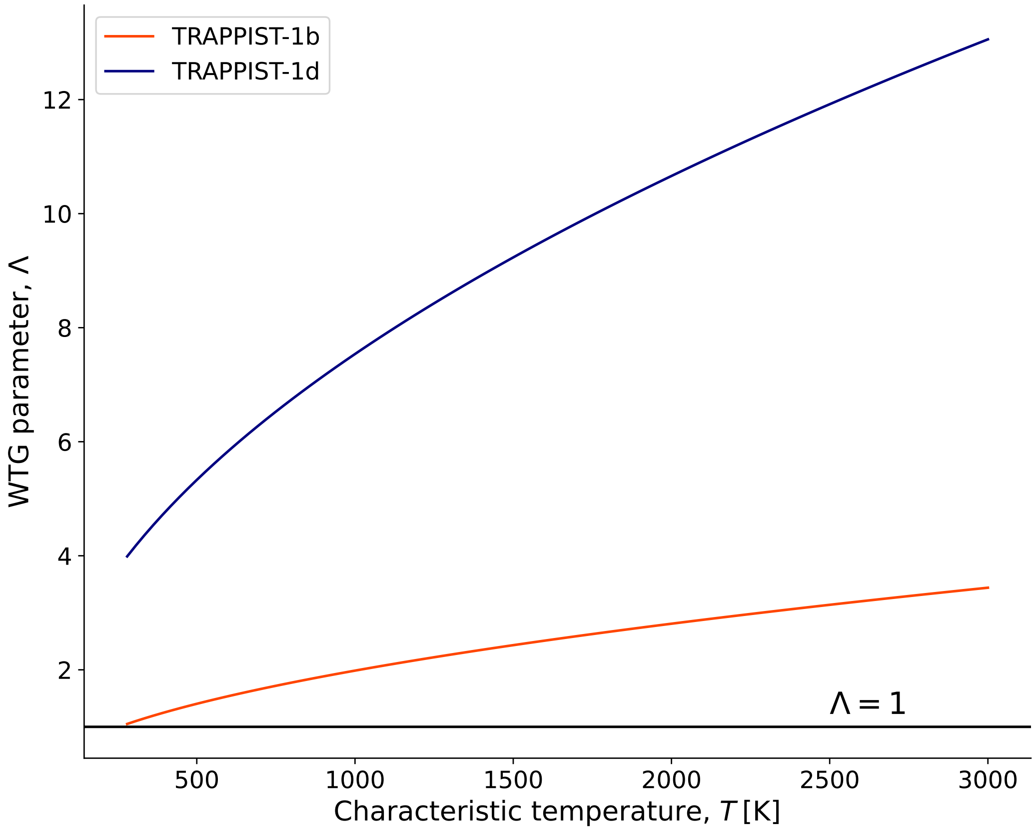

Figure 7.3: WTG parameter as a function of the characteristic temperature of the atmosphere. The minimum value for TRAPPIST-1b is 1.05 at 280 K.

of bands above this threshold would lead to an increase in runtime along with a significantly smaller increase in accuracy. Conversely, it could be that the increase in accuracy versus runtime follows a roughly linear trend up to the limit of real-gas radiation. This will be worth investigating in the future.

The cubed-sphere resolution is 25x25 grid points in the X and Y directions on each face of the cube. This comes down to a lon-lat resolution of 3.6°, corresponding to about 123.8 km for TRAPPIST-1b and 87.4 km for TRAPPIST-1d. The vertical grid with 47 levels was originally defined by the GFDL to study the quasi-biennial oscillation (QBO) on Earth. It is used here because its top pressure is low enough that the model can resolve the top layers up to 0.1 mbar. The specific heat capacity of dry air at constant pressure, $\mathrm{c_p}$, is assumed constant, set at the value for water vapour at 300 K. Its variation as a function of temperature can be seen on Figure 7.4. Incorporating a T-dependent $\mathrm{c_p}$ would require major rewrites of the dynamical core, which are beyond the scope of the present work which is aimed at elucidating basic phenomena. The incident stellar flux at the top of the atmosphere is computed using Equation 7.3,

$$F_{\mathrm{star}} = \frac{L_{\mathrm{star}}}{4\pi a^2}, \tag{7.3}$$

where L_{star} is the stellar luminosity and a is the orbital radius, with the orbit assumed circular. The additional factor 1/4 usually multiplied to the flux to account for the rotation is omitted, since we assume tidal locking. The Bond albedo $\mathrm{A_B}$ should be computed by scattering in the radiation scheme, but is set to zero since scattering is neglected here. The surface albedo is a free parameter, and given the high opacities involved in the atmospheres studied here, setting it to zero is also a reasonable, if idealized, approximation.

The hybrid sigma-pressure coordinates are defined at each level k as $\mathrm{p(k) = a_k(k) + b_k(k) \cdot p_s}$, where $\mathrm{p_s}$ is the surface pressure and the $\mathrm{a_k}$ and $\mathrm{b_k}$ coefficients are respectively defined as the arrays shown below.

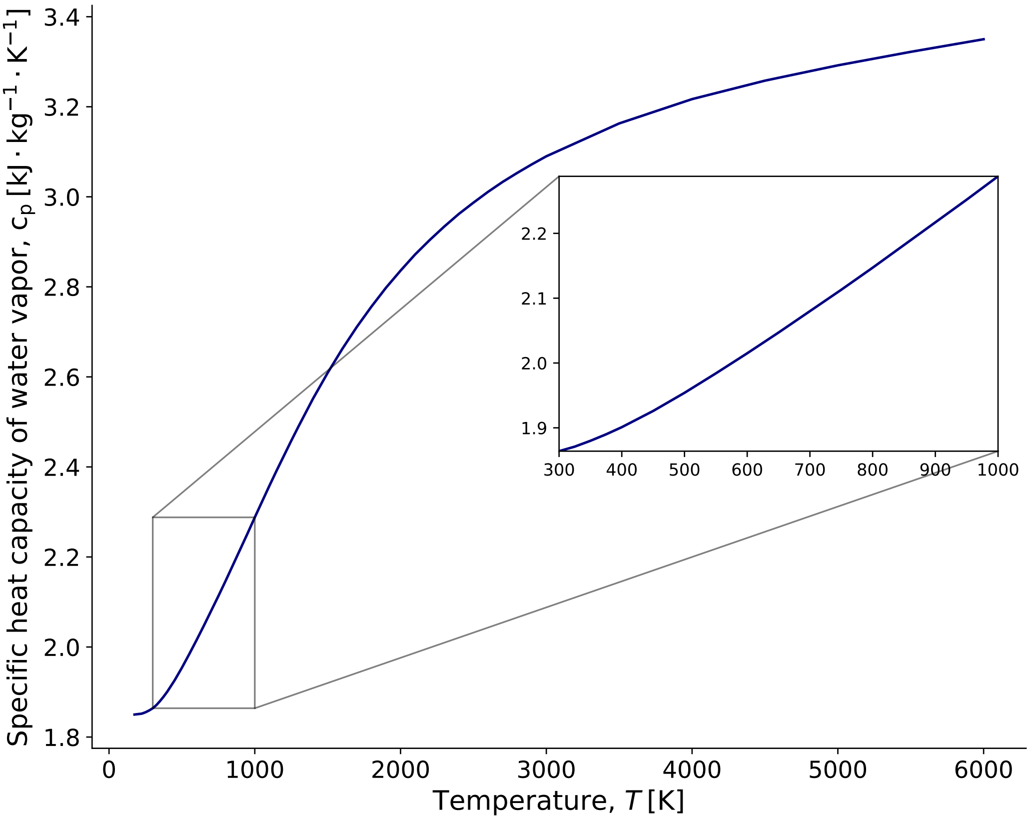

Figure 7.4: Variation of the specific heat of water vapour with temperature according to the Engineering ToolBox (2005).

$$\begin{pmatrix}
10.00000 & 24.45365 & 48.76776 & 85.39458 & 133.41983 & 191.01402 \\
257.94919 & 336.63306 & 431.52741 & 548.18995 & 692.78825 & 872.16512 \\
1094.18467 & 1368.11917 & 1704.99489 & 2117.91945 & 2622.42986 & 3236.88281 \\
3982.89623 & 4885.84733 & 5975.43260 & 7286.29500 & 8858.72424 & 10739.43477 \\
12982.41110 & 15649.68745 & 18811.37629 & 22542.71275 & 25724.93857 & 27314.36781 \\
27498.59474 & 26501.79312 & 24605.92991 & 22130.51655 & 19381.30274 & 16601.56419 \\
13952.53231 & 11522.93244 & 9350.82303 & 7443.47723 & 5790.77434 & 4373.32696 \\
3167.47008 & 2148.51663 & 1293.15510 & 581.62429 & 0.00000 & 0.00000
\end{pmatrix}$$

$$\begin{pmatrix}
0.0000 & 0.0000 & 0.0000 & 0.00000 & 0.00000 & 0.00000 & 0.00000 & 0.00000 \\
0.00000 & 0.00000 & 0.00000 & 0.00000 & 0.00000 & 0.00000 & 0.00000 & 0.00000 \\
0.00000 & 0.00000 & 0.00000 & 0.00000 & 0.00000 & 0.00000 & 0.00000 & 0.00000 \\
0.00000 & 0.00000 & 0.00000 & 0.00000 & 0.01188 & 0.04650 & 0.10170 & 0.17401 \\
0.25832 & 0.34850 & 0.43872 & 0.52448 & 0.60307 & 0.67328 & 0.73492 & 0.78834 \\
0.83418 & 0.87320 & 0.90622 & 0.93399 & 0.95723 & 0.97650 & 0.99223 & 1.00000
\end{pmatrix}$$

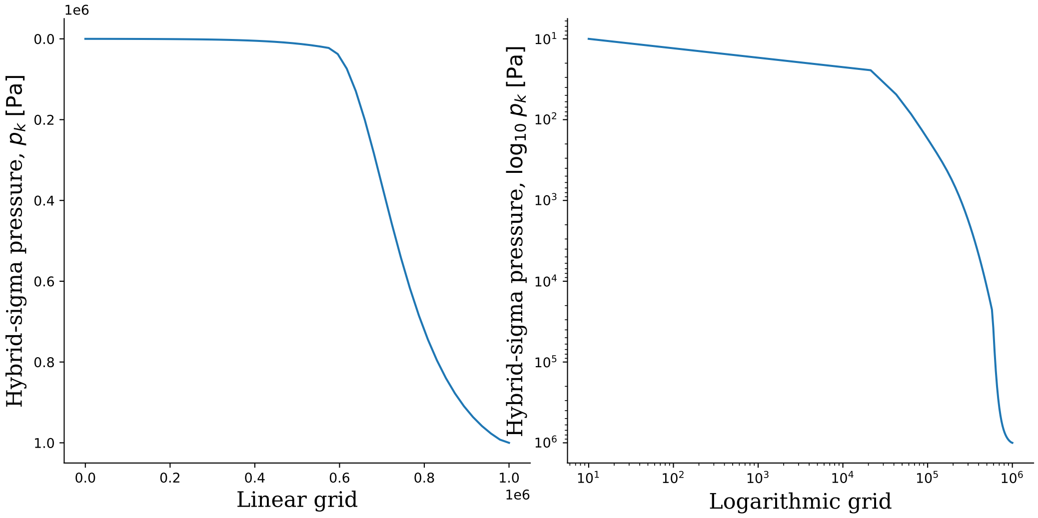

Figure 7.5: Hybrid-sigma pressure grid as a function of a linear grid spanning the same pressure range between 10 and 10^6 Pa. The left panel uses a linear scale, and the right panel a logarithmic scale.

Figure 7.5 shows the structure of the pressure grid used. Both a linear scale (left) and a logarithmic scale (right) are shown, to highlight the variation at the top of the atmosphere. Above about 250 mbar, the b_k coefficient becomes zero and the profile adopts a more linear behaviour.

7.4 Diagnostics for linking model outputs to observations

Phase curves were computed to estimate the detectability of a secondary eclipse depending on the spectral region probed. They measure the ratio of band-integrated powers $\frac{\int \mathrm{P_p d\lambda_p}}{\int \mathrm{P_\star d\lambda_\star}}$ as a function of the orbital phase, with P_p the outgoing planetary radiation integrated over the surface area of the planet, and $P_\star$ the wavelength-dependent stellar flux of TRAPPIST-1 from Lincowski et al. (2018) multiplied by the square of the star's radius. This is done separately for each of the six bands defined by the band-grey model, using a simple Python code developed for this purpose, whose formulation is described e.g. by Cowan and Agol (2008).

The TRAPPIST-1 planets will be observed by several Cycle 1 GTO (Guaranteed Time Observations) and GO (General Observers) programs using JWST instruments.

The W2 band defined in Boukrouche et al. (2021) and in this work spans the range $[7.692, 20.00]$ μm, which is included in the MIRI spectral range but does not cover it. The low-resolution spectrometer (LRS, Kendrew et al. (2015)) of MIRI has a nominal range between 5 and 10 μm, however the bandpass provided by PANDEXO (Batalha et al., 2017) reaches 14 μm, close to the limit of 14.5 μm beyond which the slit spectrum no longer falls onto the detector.

In order to get an idea of the signal-to-noise ratio for theoretical observations of these planets in each model band, we computed the error bars associated with secondary eclipse observations of TRAPPIST-1b and d by MIRI/LRS using PANDEXO and accounting for 5 secondary eclipse observations. This is inspired by Greene, Lagage, Rieke, and Schlawin (2017), with the difference that they employ MIRI in photometry using the imager rather than in spectroscopy. We assumed a saturation limit of 250,000 e^{-} after Rieke et al. (2015) and a noise floor of 40 ppm after Chouqar et al. (2020). We binned the errors over the spectral range of MIRI/LRS using Equation 7.4 (Vivien Parmentier, personal communication).

$$\mathrm{E}_{\mathrm{binned}} = \left(\left(\sum_{\lambda_{\mathrm{MIRI}}} \frac{\mathrm{d}\lambda}{\mathrm{E}^2} \right) \left(\frac{1}{\sum_{\lambda_{\mathrm{MIRI}}} \mathrm{d}\lambda} \right) \right)^{-\frac{1}{2}}, \tag{7.4}$$

where $\mathrm{E}_{\mathrm{binned}}$ is the error in ppm binned over the part of the MIRI range provided by PANDEXO (5 to 13.86 microns), accounting for 5 eclipses. $\mathrm{E} = \frac{\mathrm{E}_{\mathrm{PANDEXO}}}{\sqrt{5}}$ is the spectral precision $\mathrm{E}_{\mathrm{PANDEXO}}$ computed by PANDEXO in ppm scaled for 5 eclipses. This provided two error bars, for each planet, that we added to the phase curves at a phase of 0.75 corresponding to the secondary eclipse.

It is important to note that only 70% of the spectral range of MIRI/LRS overlaps with that of W2. This difference means that this calculation does not yield the actual error bars that would result from observations in the W2 band, but only an indication of the orders of magnitude that can be expected. The next step of this calculation will include error bars for the MIRI imager over the filters F770W, F1000W, F1130W, F1280, F1500W, and F1800, which, together, span the range [6.5, 20] $\mu\mathrm{m}$, which fits much more closely with the W2 band.

8 | 3D results

This chapter presents the results obtained from the simulations performed with Exo-FMS. There are six main simulations using parameters corresponding to two planets, TRAPPIST-1b and TRAPPIST-1d, and exploring three surface pressures, as described on Table 8.1.

Planet	Surface pressure	Run time
TRAPPIST-1b	1 bar	8000 days
TRAPPIST-1d	1 bar	10000 days
TRAPPIST-1b	10 bar	5000 days
TRAPPIST-1d	10 bar	10000 days
TRAPPIST-1b	260 bar	9400 days
TRAPPIST-1d	260 bar	12500 days

Table 8.1: Run lengths.

These simulations were mainly aimed at exploring the depth of the condensation layer, the temperature contrast between the dayside and the nightside as a function of height, the possible suppression of clouds on the dayside and nightside, and the phase curves expected from each scenario.

Figure 8.1 shows the locations of the substellar and antistellar points and the morning and evening terminators on the cubed-sphere grid that are shown in Figures 8.5, 8.18, and 8.28. All global maps use a Robinson projection and are time-averaged over one Earth day. The coordinates for each point on the grid are:

- $\mathrm{x_{substellar}} = 1°52'30''\mathrm{N}, 1°52'30''\mathrm{E}$
- $\mathrm{x_{antistellar}} = 1°52'30''\mathrm{N}, 178°7'30''\mathrm{W}$
- $\mathrm{x_{morning}} = 1°52'30''\mathrm{N}, 88°7'30''\mathrm{W}$
- $\mathrm{x_{evening}} = 1°52'30''\mathrm{N}, 88°7'30''\mathrm{E}.$

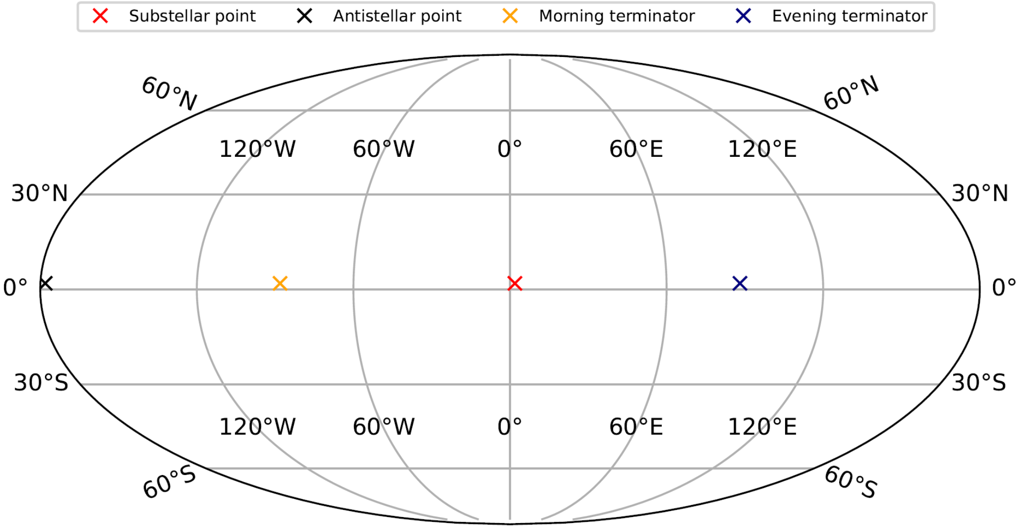

Figure 8.1: Robinson projection displaying the locations on the cubed-sphere grid used in the 1D graphs.

8.1 Convergence analysis

During the ongoing development of Exo-FMS, we studied the performance of the different modules included in the model, including the dynamical core and the radiation modules. When plotting equilibration evolutions, I noticed a significant TOA energy imbalance of typically a few hundred watts per square meter in any run using the new radiation schemes introduced during the development.

In these opaque conditions, making the deep layers converge would conceivably take an order of magnitude larger number of simulation days than the number that we had time to use in this thesis. This might have implications on the resulting thermal structures and energy budgets retrieved. Turbet et al. (2019) implemented a numerical method in the LMD Generic Planetary Climate Model (PCM) dedicated to significantly speed up the convergence toward radiative equilibrium in thick steam atmospheres. Even using this method, with a surface pressure of 10 bar, they needed more than 50000 Earth days of model time to converge, which is in line with the required number of 72000 days that we estimated from 1D test simulations. With 260 bar, they expect that an order of magnitude of 10^6 simulation days might be needed to equilibrate the deep layers (Martin Turbet, personal communication), especially in the case of an M dwarf whose emission spectrum peaks closer to the IR regions than the Sun. In these cases such as with TRAPPIST-1, less radiation is able to reach the deep layers before being absorbed, which results in less radiative heating and a slower convergence. This can also possibly make the deep atmosphere less convective, which removes the benefit of rapid heat transport from convective adjustment.

Even so, we wanted to identify the source of the imbalance that we obtained even in less opaque conditions. To this aim, we plotted on Figure 8.2 the evolution of the distance to equilibrium for TRAPPIST-1b at $\mathrm{p_s} = 1$ bar, at the substellar and antistellar points as well as the global imbalance. The distance to equilibrium is the difference between the ISR and the bolometric OPR integrated over all latitudes and longitudes and normalized by the surface area of the planet, with the equation

$$\mathrm{Budget} = \frac{\sum_i \mathrm{ISR}_i\, a_i - \sum_i \mathrm{OPR}_i\, a_i}{A_p}, \tag{8.1}$$

where A_p is the analytic surface area of the planet, ISR_i and OPR_i the incoming stellar radiation and outgoing planetary radiation in the cubed-sphere cell i, and a_i the local surface area of the cubed-sphere cell i.

The global imbalance sits at an average of -222 $\mathrm{W\,m^{-2}}$ after 200 days. After the same threshold, the difference between the substellar and antistellar imbalances is on average 4740.7 $\mathrm{W\,m^{-2}}$. This suggests that the global imbalance is rather small compared to the amount of heat transported from the dayside to the nightside.

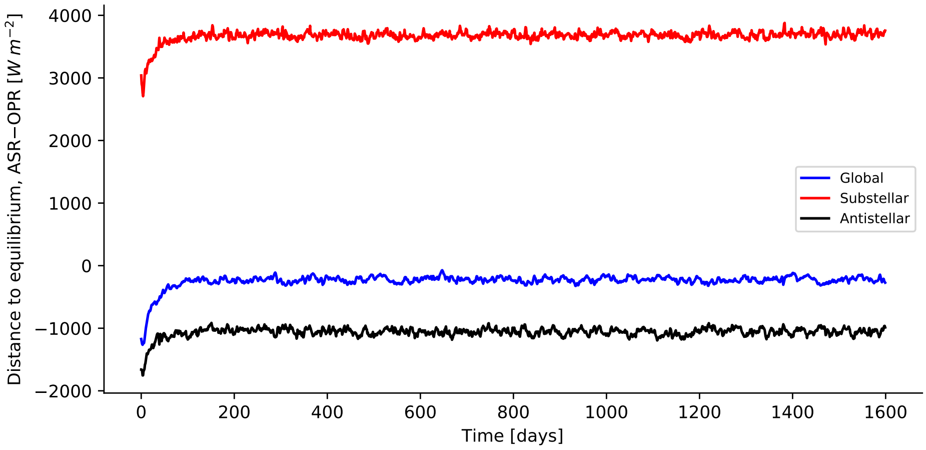

Figure 8.2: Evolution of the distance to equilibrium for TRAPPIST-1b at $\mathrm{p_s} = 1$ bar, at the substellar and antistellar points as well as the global imbalance.

On Figure 8.3 we explore the contribution of the radiation module to the imbalance by turning off the dynamics, using the case of TRAPPIST-1b at $\mathrm{p_s} = 10$ bar. When transport is turned off, the nightside has no source of heating, so will cool down forever and never reach equilibrium. Therefore we restrict our exploration to the dayside. After 2300 simulation days, the dayside imbalance flattens out around 7.96 $\mathrm{W\,m^{-2}}$ with a rate of change of about -0.02 $\mathrm{W\,m^{-2}\,day^{-1}}$. The substellar regions within 30° of latitude and longitude show an imbalance of -1.87 $\mathrm{W\,m^{-2}}$ with a rate of change of about $-9{\cdot}10^{-4}\ \mathrm{W\,m^{-2}\,day^{-1}}$. This calculation demonstrates that most of the imbalance is due to the dynamical heat transport. The radiation flux scheme and convective adjustment explicitly conserve column-integrated enthalpy, so the slight imbalance relative to the instellation is most likely due to the time stepping of the surface energy budget.

Finally, on Figure 8.4 we turn off the radiation and the boundary layer scheme and test the dynamical core. We first initialise a tidally locked simulation with a warm dayside and cold nightside by running a hundred days with a semi-grey radiation

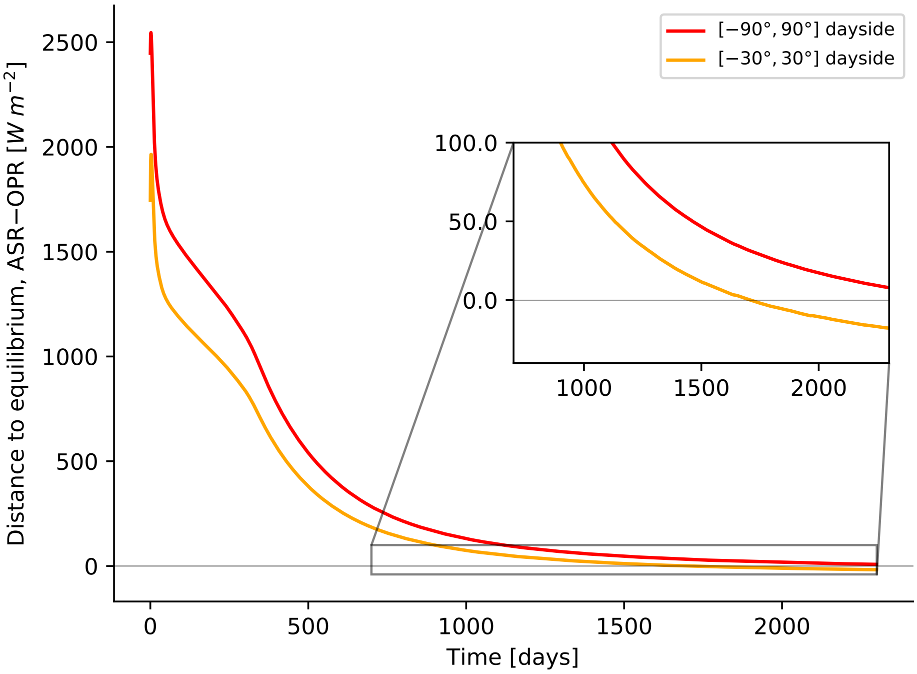

Figure 8.3: Evolution of the distance to equilibrium for TRAPPIST-1b at $\mathrm{p_s} = 10$ bar. The red curve is the imbalance on the dayside and the orange curve is the imbalance from the circle around the substellar point within 30°. Dynamics have been turned off.

scheme. After the hundredth day, we turn off the radiation and let the dynamics adjust. We then plot the total energy output by the model, computed by

$$\mathrm{E_{total}} = \frac{\sum_i \mathrm{E}_i\, a_i}{A_p}, \tag{8.2}$$

where $\mathrm{E_{total}}$ is the total energy of the planet, E_i the addition of the kinetic and potential energy integrated over the atmospheric column i located in the cubed-sphere cell i, and a_i the local surface area of the cubed-sphere cell i. A_p is the analytic surface area of the planet as above.

The curve reaches a local maximum at around 3000 days before decreasing. The total energy decreases by about $8.16 \cdot 10^8$ J $\cdot$ kg^{-1} over the last 3000 days and is still decreasing, and the curve shows higher frequency variations on the order of $2 \cdot 10^9$ J $\cdot$ kg^{-1}.

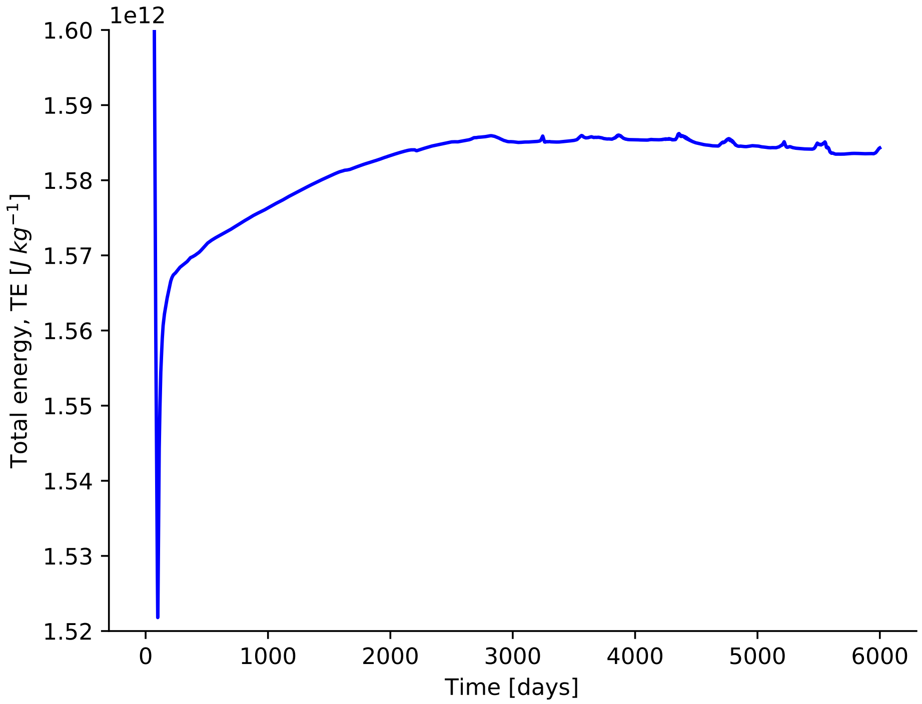

Figure 8.4: Evolution of the total energy for TRAPPIST-1b at $\mathrm{p_s} = 10$ bar. Radiation is turned on only over the first 100 days of the simulation.

It suggests that something outside the radiation and boundary layer schemes might be improperly conserving energy. It it also possible that a much longer simulation run might yield a stabilized total energy in the model. The Exo-FMS thermodynamic equation is based on potential temperature and written in advective form, so it does not guarantee enthalpy conservation. Either way, more work is needed in order to identify the exact source of the imbalance and prepare Exo-FMS for its next benchmarking phase.

8.2 10 bar surface pressure

The first case we looked at is a surface pressure of 10 bar. Figures 8.5 to 8.17 compare TRAPPIST-1b and TRAPPIST-1d for each quantity explored at this surface pressure. TRAPPIST-1b is represented by panels T1b, and TRAPPIST-1d by panels T1d. The surface temperature is initialised at 1225 K, which is close to the equilibrium temperature expected from our 1D work, and is allowed to evolve.

The left plots of Figure 8.5 show the temperature profiles at each point defined in Figure 8.1. The red dotted curve indicates the dew point curve of water vapour for reference. The substellar surface temperature reached 1568 K on TRAPPIST-1b and 1454 K on TRAPPIST-1d. A potential non-convective radiative layer can be seen developing on the substellar points of both planets around 3 bar, and the TOA displays a definite inversion consistent with the impact of stellar heating, suggesting that condensation may only occur on the night side above about 0.3 mbar. One often expects to see a nightside surface inversion (Pierrehumbert & Hammond, 2019), but in this case the extreme optical thickness of a water vapour atmosphere radiatively heats the nightside surface enough to keep a nightside surface inversion from forming. The TOA inversion is less significant on TRAPPIST-1d, due to the weaker incoming stellar flux heating the upper layers. In this case, condensation becomes possible between about 0.5 to 0.2 mbar at all longitudes. Most of the thermal emission is from the very upper part of the atmosphere, and that is where all the condensation is too, in a thin skin near the top. This means that it is important to have adequate resolution near the top of the model.

The middle plots show the profiles of the total flux at the same locations, defined by the sum of the thermal and stellar fluxes, with the upward direction being positive. These curves give an idea of the pattern of local disequilibrium caused by dynam-

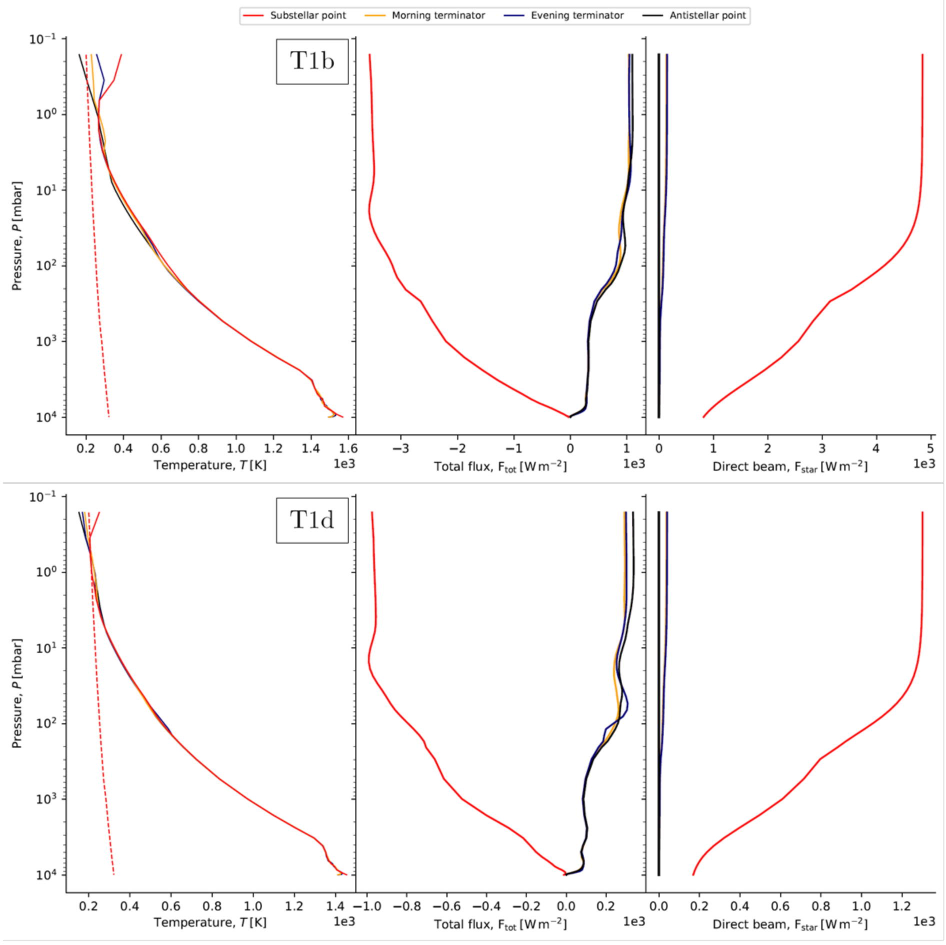

Figure 8.5: Vertical **(Left)** temperature, **(Middle)** total flux, and **(Right)** direct beam profiles of TRAPPIST-1b and TRAPPIST-1d at their substellar and antistellar points, and on the morning and evening terminators, assuming a surface pressure of $p_s = 10$ bar.

ics. The total flux is vertically constant in pure radiative equilibrium and generally increasing with height, given net radiative cooling, in the convecting regions. In the current plot, we can see a region of nearly vertically constant flux above about 30 mb, which indicates pure radiative equilibrium there. Between 30 mb and the ground on the dayside is a region where the total flux is increasing with height, suggesting net radiative cooling, and it is indicative of a convective troposphere.

The negative nightside net flux represents net cooling of the nightside atmosphere to space.

The right plots show the direct beam from the star, penetrating the atmosphere unimpeded by scattering in these simulations. These curves show where stellar heating is deposited and how much reaches the ground. The substellar instellation of both planets is barely attenuated until it reaches around 30 mbar. One might notice that the moist adiabatic adjustment does not seem to make the profiles adjust to the dew point curve of water vapour as it should near the TOA. This is in fact due to the radiative cooling balancing or exceeding the heating from condensation at these levels.

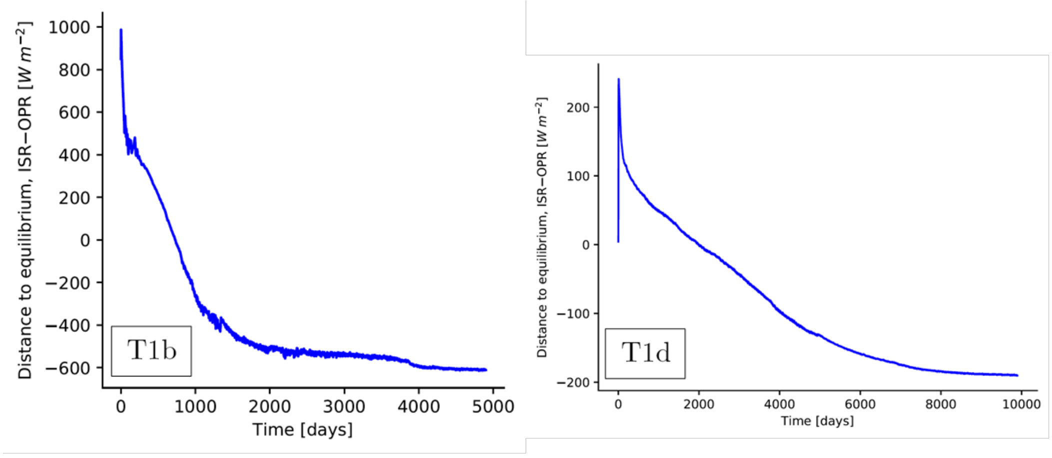

Figure 8.6: Evolution of the distance to equilibrium for **(A)** TRAPPIST-1b and **(B)** TRAPPIST-1d. $\mathrm{p_s} = 10$ bar.

Figure 8.6 shows the evolution of the distance to radiative equilibrium at the TOA, using Equation 8.1. A relative stability seems to be reached after 4000 days and 9000 days for TRAPPIST-1b and d respectively. We also checked the equilibration using temperature tendencies obtained and animations of the temperature profiles over the simulated time, which increased our confidence in the equilibration. The time series of the temperature and net flux is displayed on Figure 8.7. The red, green, and blue curves respectively correspond to the surface, the 5-bar pressure level, and the top of the atmosphere. The surface of TRAPPIST-1b warmed up from 1225 K to 1567 K over the first 2000 days. From day 2000 to 5000, the surface temperature displays variations around 1568 K of at most 3.9 K but there is no clear upward trend from day 2000 onward. After about 1500 days, the total net flux at the surface, defined by the difference between the bolometric upward and downward fluxes, sits at around -36 $\mathrm{W\,m^{-2}}$.

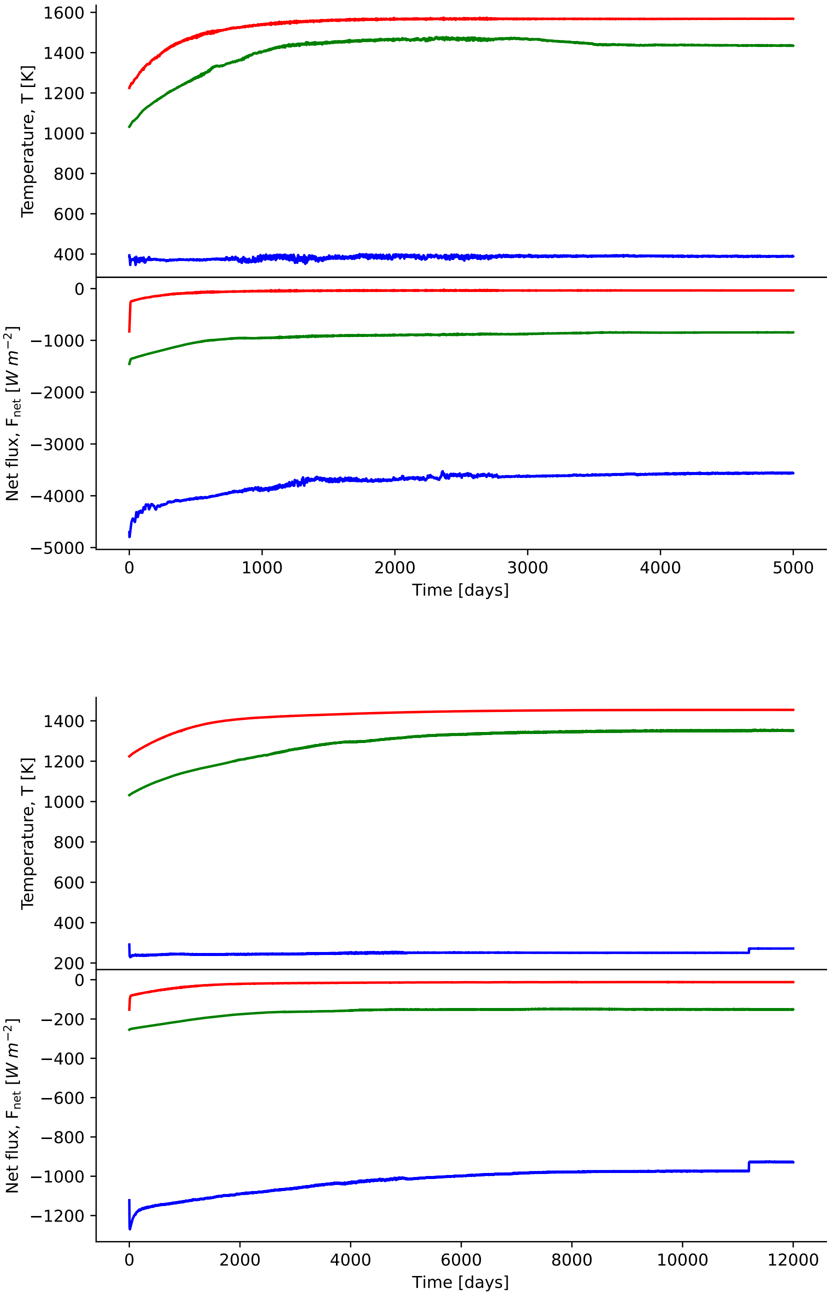

Figure 8.7: Time series of temperature and total flux over simulated time for TRAPPIST-1b **(Top)** and TRAPPIST-1d **(Bottom)**, at the top (blue), middle (5 bar, green), and bottom (red) of the atmosphere. $p_s = 10$ bar.

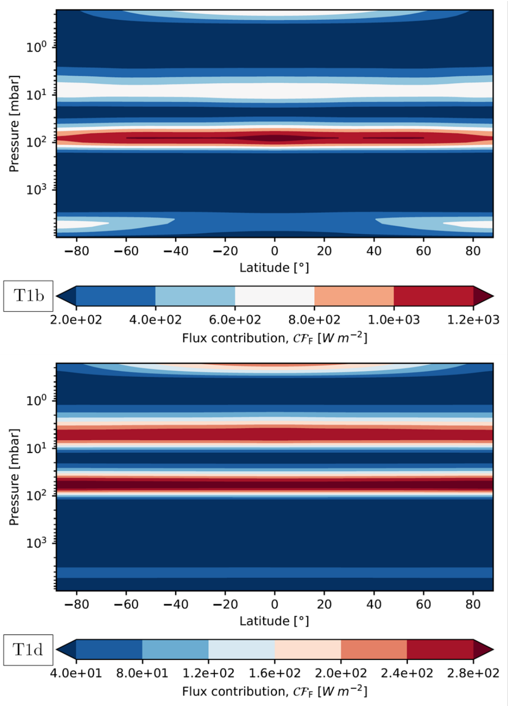

Figure 8.8: Zonal mean contribution function $\mathrm{p_s} = 10$ bar.

The surface of TRAPPIST-1d warmed up from 1225 K to 1454 K. It is still warming up, however the rate of change is decreasing and has dropped below $3.03 \cdot 10^{-4}\,\mathrm{K\,day^{-1}}$ at day 8700.

Figure 8.8 shows the zonal mean contribution function as a function of pressure and latitude. Peaks are present at the TOA of TRAPPIST-1b as well as around 8 and 80 mbar. A smaller one can be seen developing deeper down, around the half surface pressure level, 5 bar, coming from the visible and UV contributions. The peaks of the $\mathcal{CF}_\mathrm{F}$ are higher up in the atmosphere of TRAPPIST-1d. The TOA is still one of the main contributors to the OPR, as expected, while the other peaks are located around the 5 mbar and 60 mbar levels. There is also a contribution from the half surface pressure level, though it is weaker than the one present on TRAPPIST-1b. Both the higher peaks and the weaker half surface pressure contribution can be explained at least partly by the smaller surface gravity of TRAPPIST-1d, which makes the atmosphere more optically thick through the relation $\kappa \approx \frac{p_s}{g}$. The one-dimensional $\mathcal{CF}_\mathrm{F}$ profiles showed on figure 5.6 for instance, looks similar to Figure 8.8, in terms of the locations of the peaks of the $\mathcal{CF}_\mathrm{F}$ in each band.

Figure 8.9 shows the global temperature map at four selected pressure levels for both planets. These levels were chosen because they correspond to the locations of the peaks of the flux contribution function as seen on Figure 8.8. The quiver fields of the zonal wind at the same pressure levels is also overlaid. Figure 8.10 shows the deviation of the temperature field around the zonal mean, smoothed over 100 days to remove some of the noise, and overlaid with the zonal mean of the zonal wind quiver field. This allows for the detection of lower amplitude waves when the picture is dominated by the pattern of the jet. The first panel of Figure 8.9-T1b at 0.2 mbar shows a slight eastward hot spot shift for TRAPPIST-1b, whereas the first panel of Figure 8.9-T1d at the same level shows a westward shift for TRAPPIST-1d. High amplitude Rossby waves can be seen on TRAPPIST-1b at around 8 and 80 mbar as well as others of smaller amplitudes between about 0.4 and 60 mbar. On TRAPPIST-1d, we can see high amplitude Rossby waves between 0.7 and 54 mbar, and between 80.5 and 172 mbar. We also see smaller amplitudes Rossby waves from the deviations from the zonal mean, between 0.4 and 3 mbar and at 5782 and 8176.8 mbar. Figure 8.11 shows the zonal wind contours and quiver field at the same pressure levels as above.

The temperature contrast of TRAPPIST-1b at the TOA is 210 K, but it drops to 24 K around 8 mbar. Though the surface temperature of TRAPPIST-1d is not a lot cooler than TRAPPIST-1b, the radiating level temperatures, where the planetary energy balance is determined, are a lot colder. The temperature at the 4984.4 mbar level is very nearly uniform for TRAPPIST-1d. The slight cold spot seen at 5 bar around the substellar point of TRAPPIST-1d extends to the 9 bar level, where the substellar point turns into a hot spot again. Given the small amplitude of the fluctuations, it is possible that it is just a transient effect and not a converged feature.

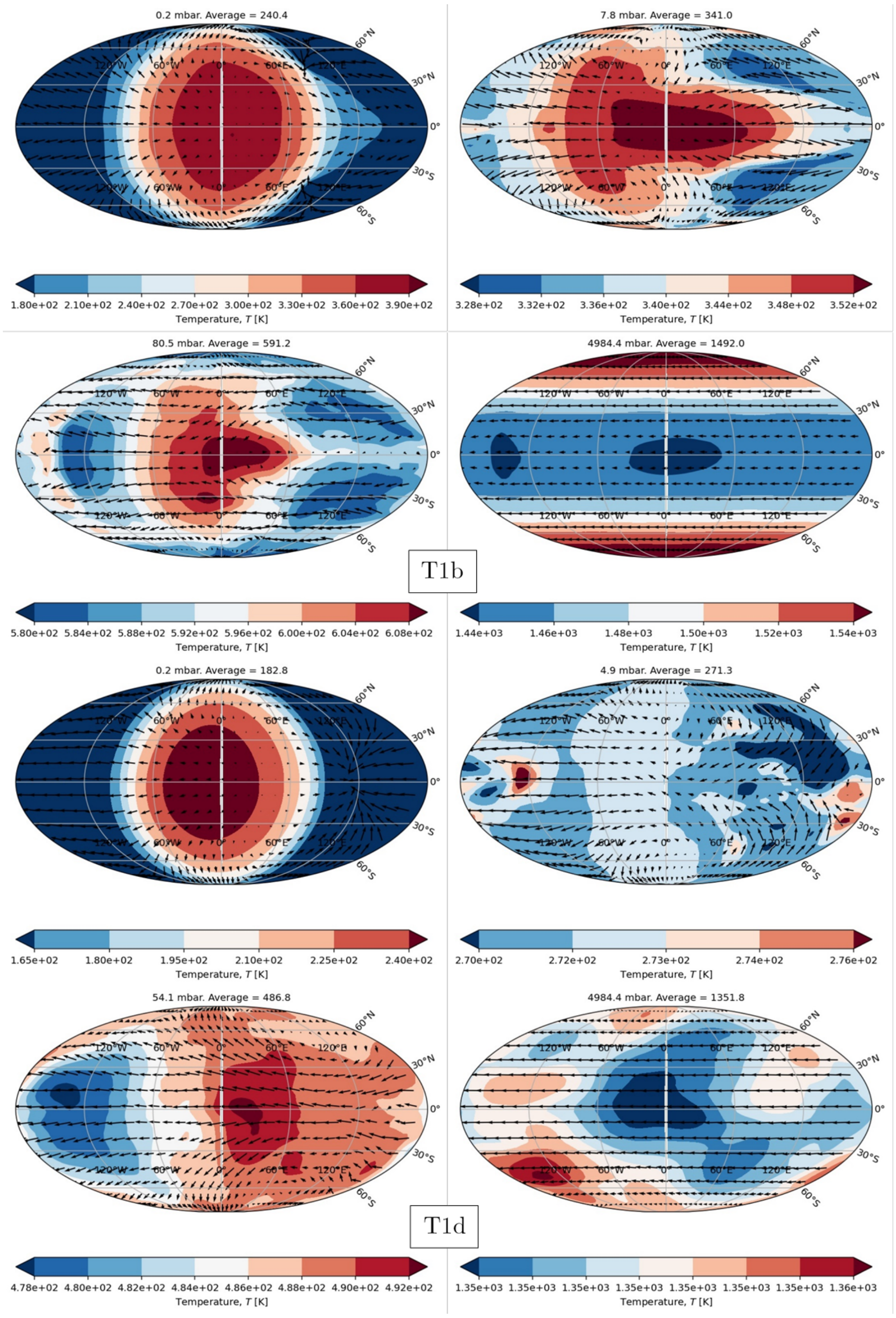

Figure 8.9: Global temperature maps at four selected altitudes. $p_s = 10$ bar.

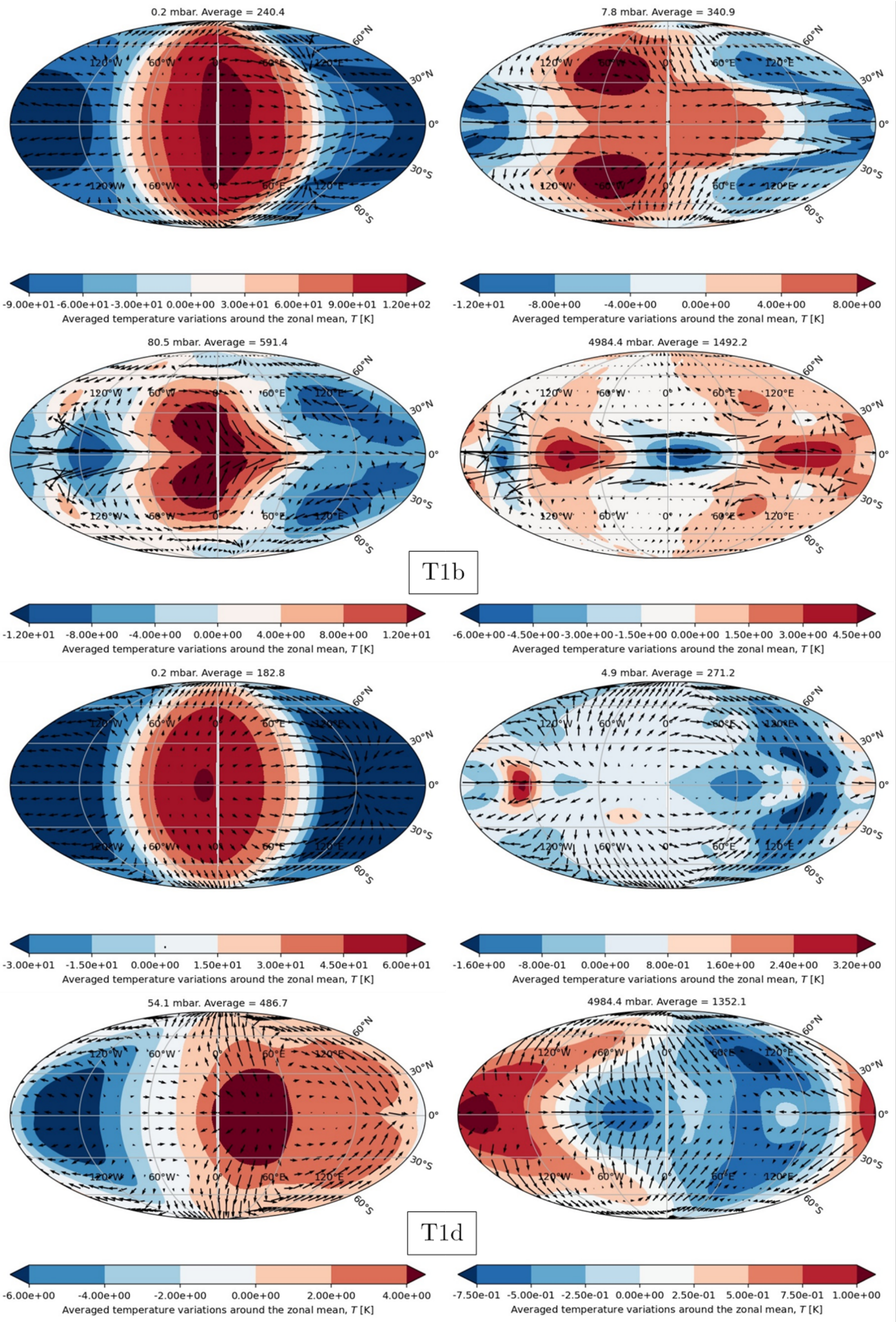

Figure 8.10: Deviation from the zonal mean. $\mathrm{p_s} = 10$ bar.

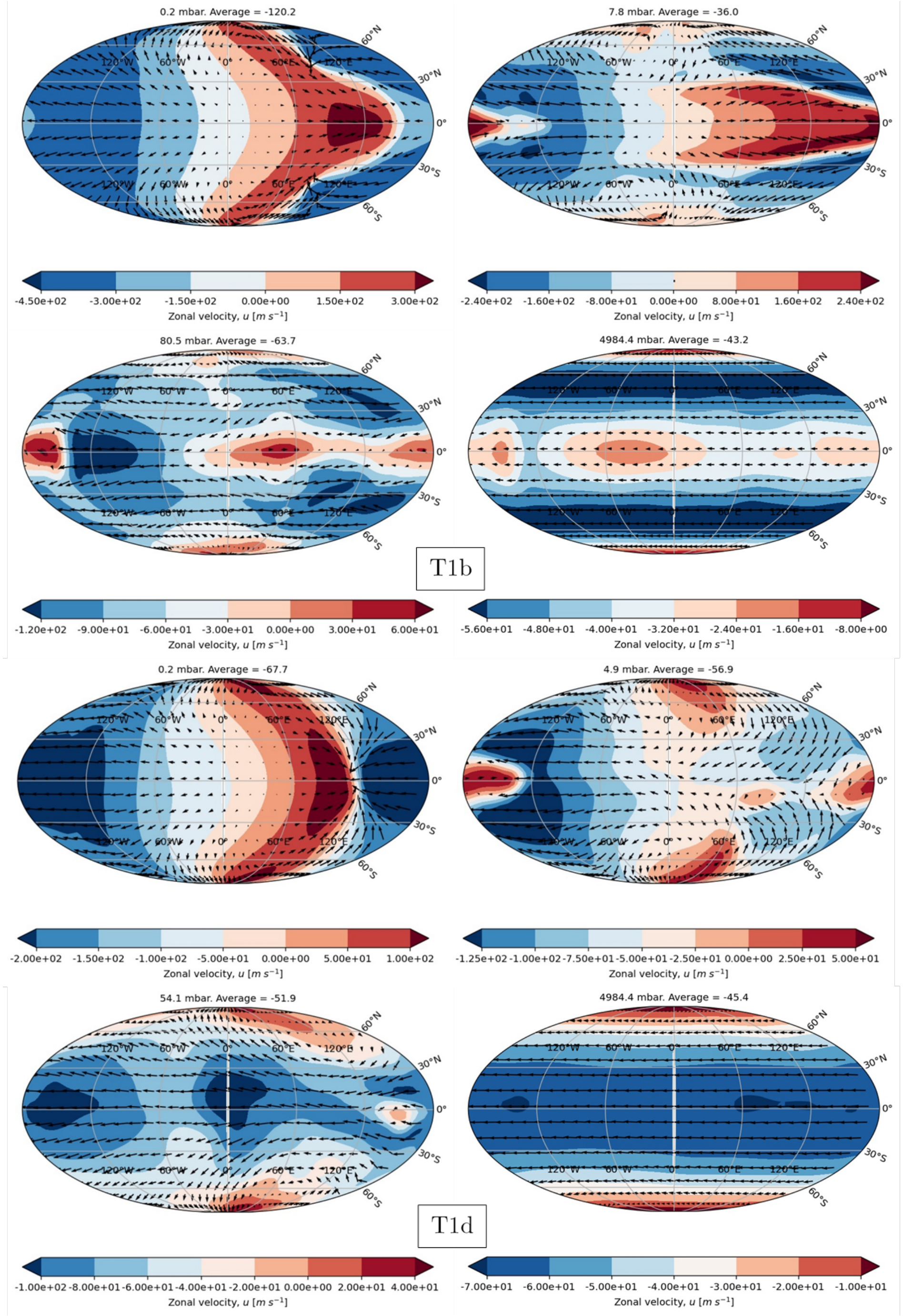

Figure 8.11: Zonal wind maps at four selected altitudes. $p_s = 10$ bar.

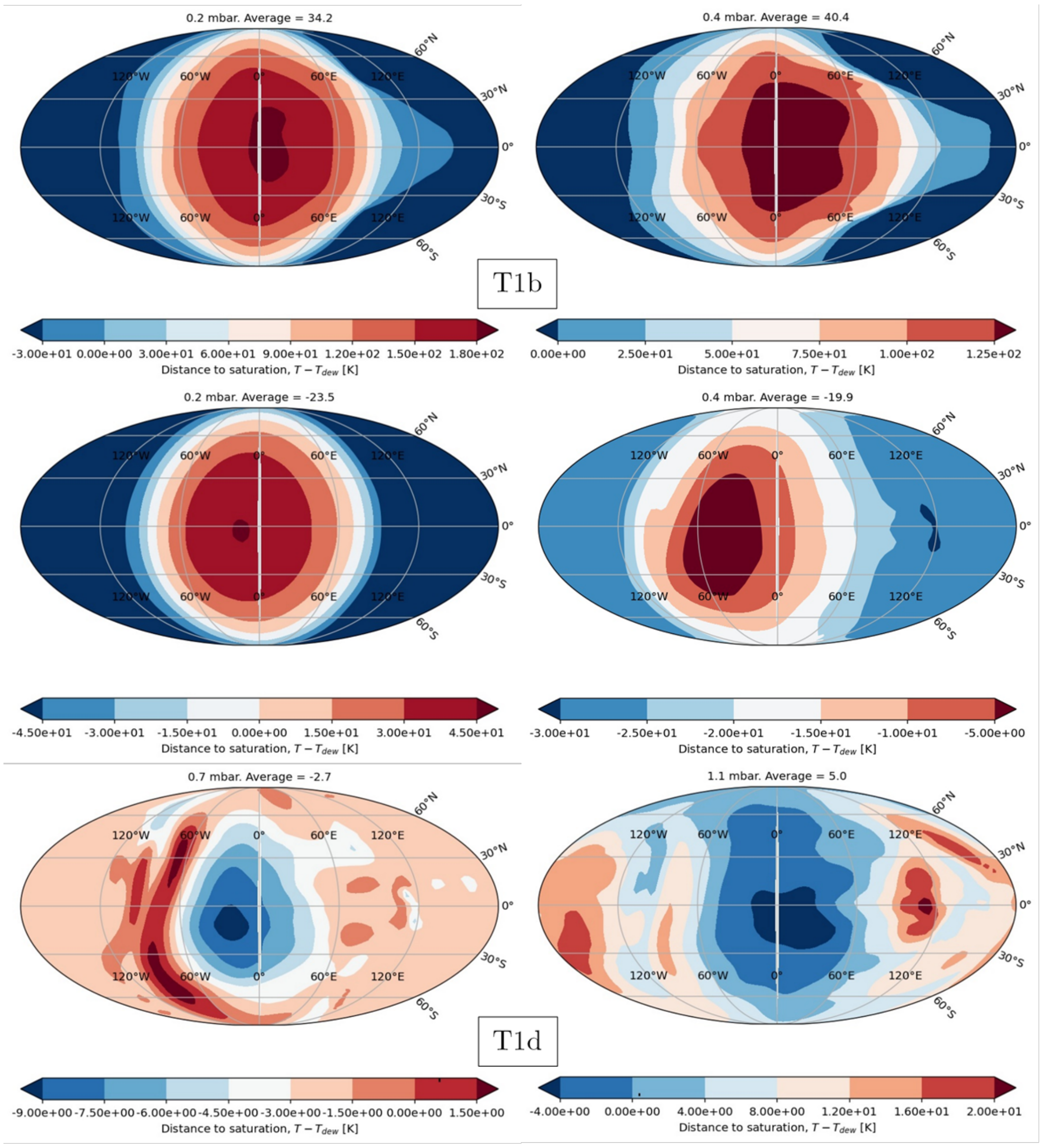

Figure 8.12: Global saturation maps at selected altitudes. $\mathrm{p_s} = 10$ bar.

Figure 8.12 shows global maps of the distance to saturation, which is the distance between the local temperature and the dew point temperature of water vapour at the local pressure. The pressure levels chosen here span the range where supersaturation is observed. Supersaturation and potential cloud formation regions exist on the nightside of TRAPPIST-1b, but are restricted to pressures lower than about 0.4 mbar. On TRAPPIST-1d, we can see deeper supersaturated regions, down to about 1.1 mbar. As explained in Section 7.1, supersaturation is possible here when the radiative cooling rate is very large, because the moist adjustment is done as a temperature increment added to the other temperature tendencies. If the supersaturation occurs in a layer where the contribution function is small, it will not strongly affect the energy budget. Preliminary tests in one dimension were performed, where the supersaturated profiles obtained for these 3D simulations were input into the 1D model and the OPR was computed and compared with a case where the same profile was instantaneously adjusted to the dew point. I then repeated this calculation except that I supersaturated the profiles down to about 4 mbar, which is deeper than the condensing regions obtained in any of the 3D simulations presented here. The first case makes the OPR vary by less than 1 $\mathrm{W\,m^{-2}}$, whereas the second case changed it by about 11.7 $\mathrm{W\,m^{-2}}$. This suggests that the supersaturation seen here does not affect the OPR significantly, however this analysis will be continued in future work.

Figure 8.13 shows the global map of the OPR on the left and the difference between the ISR and OPR on the right. The OPR of TRAPPIST-1b is relatively close to the value expected from the 1D simulations at radiative equilibrium. At a surface temperature of $\sim$1500 K, the OPR was found at about 2000 $\mathrm{W\,m^{-2}}$. The 3D simulation has reached about 2064 $\mathrm{W\,m^{-2}}$. This amplitude suggests that the planet has reached the post-runaway stage and is able to radiate through the water vapour windows and in the shorter waves from the deeper layers. TRAPPIST-1d reached 532 $\mathrm{W\,m^{-2}}$, which also indicates that the transition to the post-runaway regime has been reached.

We make use of the ability of the band-grey model to output quantities separately for each spectral band. Figures 8.14 and 8.15 show the global maps of the OPR

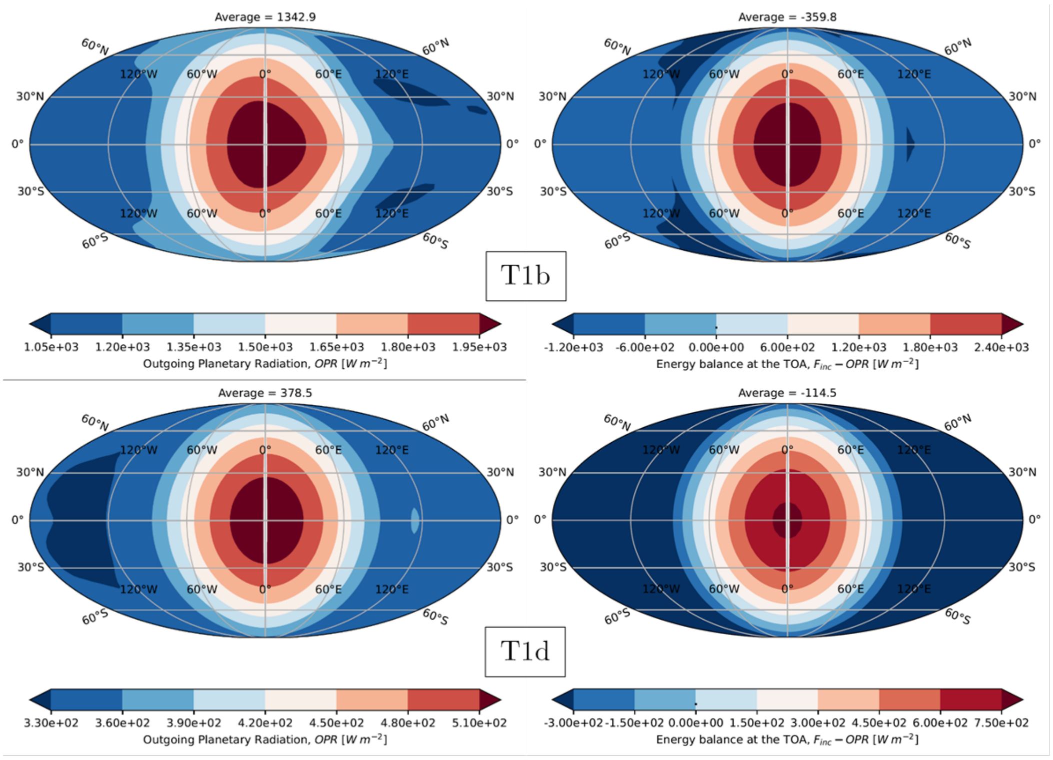

Figure 8.13: Global bolometric TOA budget maps. $\mathrm{p_s} = 10$ bar.

in each of the six spectral bands used, for each planet respectively. The pattern seen in each band corresponds to some radiating layer from which the radiation comes from. The IR contribution comes mostly from the TOA, whereas the UV one comes from the boundary layer just above the surface. The weak contribution of band VIS1, which spans the range [18750, 25000] cm^{-1} = [400, 533.33] nm, can be found around 1.6 bar. VIS2 corresponds to the range [12500, 18750] cm^{-1} = [533.33, 800] nm, and its outgoing radiation comes mainly from around half the surface pressure. The outgoing radiation from window W1 between [2200, 2900] cm^{-1} = [3448.28, 4545.45] nm comes from between about 40 to 90 mbar, which corresponds to the CFF peak centred around 80 mbar.

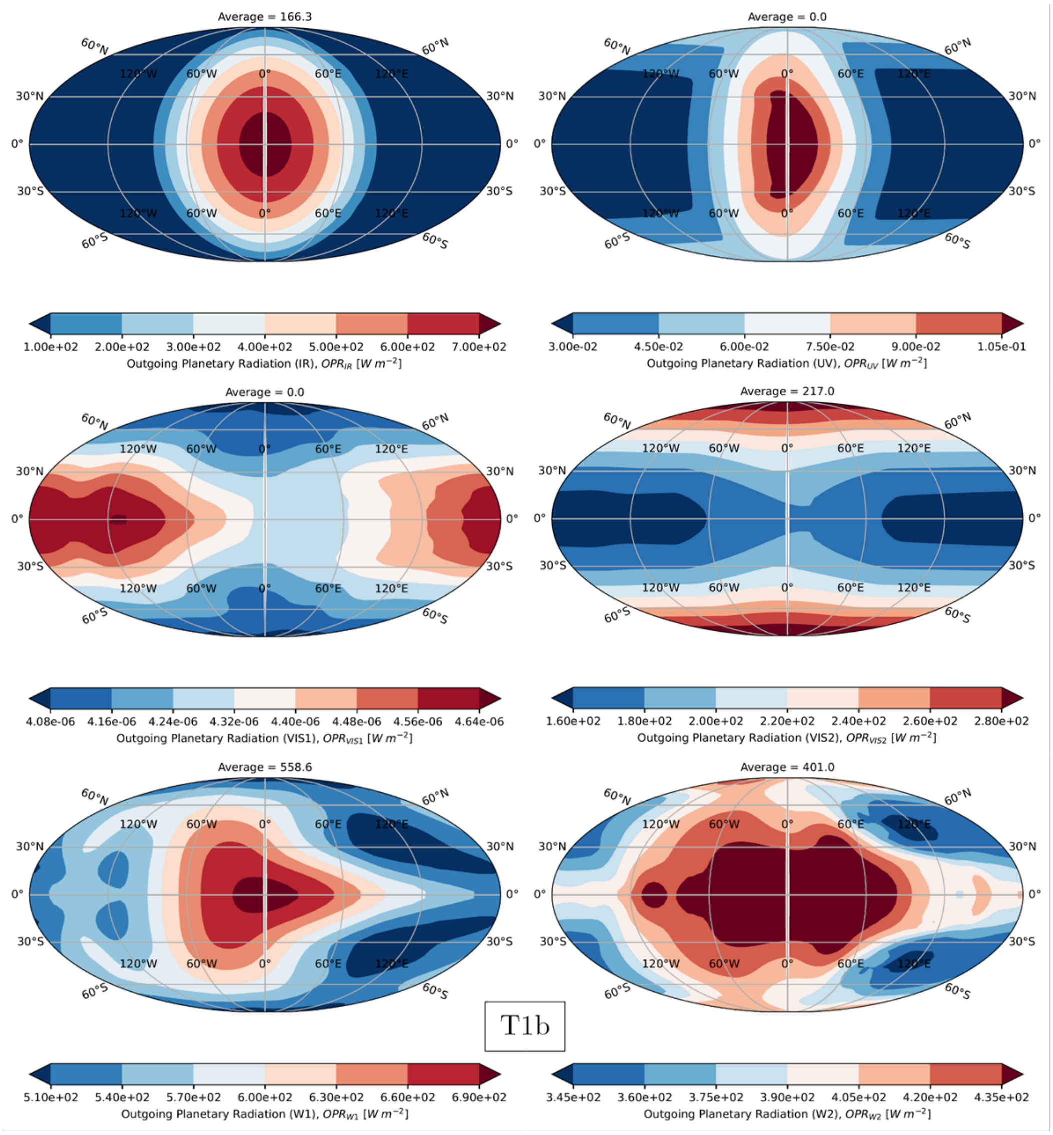

Figure 8.14: Global bandwise OPR maps for TRAPPIST-1b. $p_s = 10$ bar.

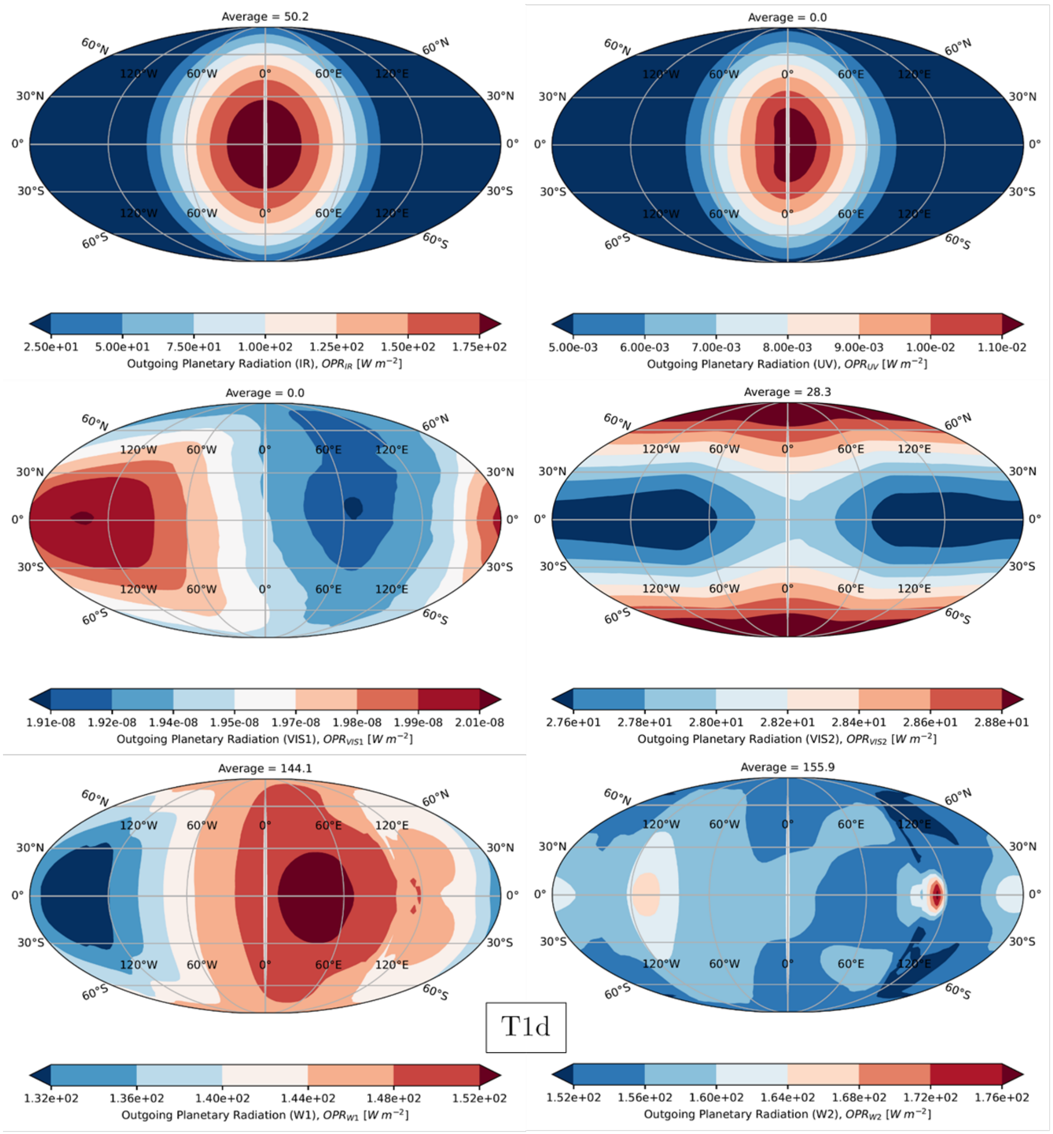

Figure 8.15: Global bandwise OPR maps for TRAPPIST-1d. $\mathrm{p_s} = 10$ bar.

The second window W2 in the range [500, 1300] cm^{-1} = [7692.31, 20000] nm contributes its outgoing radiation mainly from layers around the 8 mbar level. From this we can deduce that on panel T1b of Figure 8.8, from top to bottom, the peaks correspond to the IR band, the W2 window, the W1 window, and the bottom peak combines the VIS1, VIS2, and UV bands. Similarly for TRAPPIST-1d, the IR and

UV contributions come from the TOA and the bottom layer respectively. The VIS1 contribution is weak enough that its pattern does not have as much significance, but the layers around 2.4 bar have temperature maps with the most amount of similarity relative to the outgoing radiation. The radiation in VIS2 comes from around the half surface pressure level. The windows W1 and W2 come from 60 mbar and 5 mbar respectively. Therefore, on panel T1d of Figure 8.8, the peaks correspond from the top to the bottom to IR, W2, W1, and the weak half surface pressure peak is a combination of bands VIS1, VIS2, and UV.

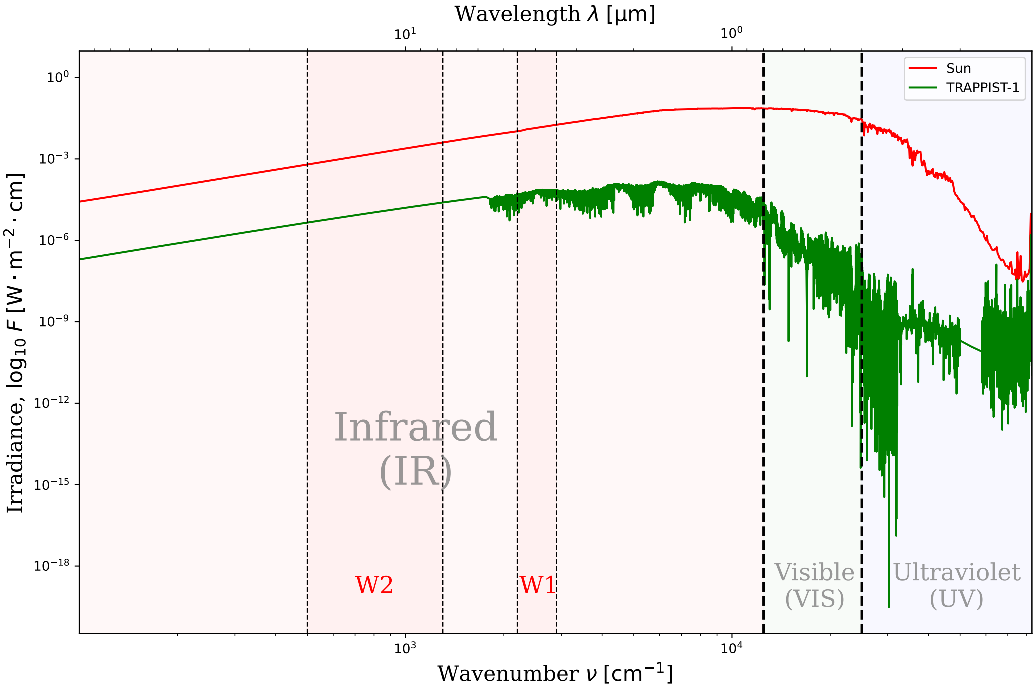

Figure 8.16: Irradiance of the Sun and TRAPPIST-1, based on Lean and DeLand (2012) and Lincowski et al. (2018) respectively.

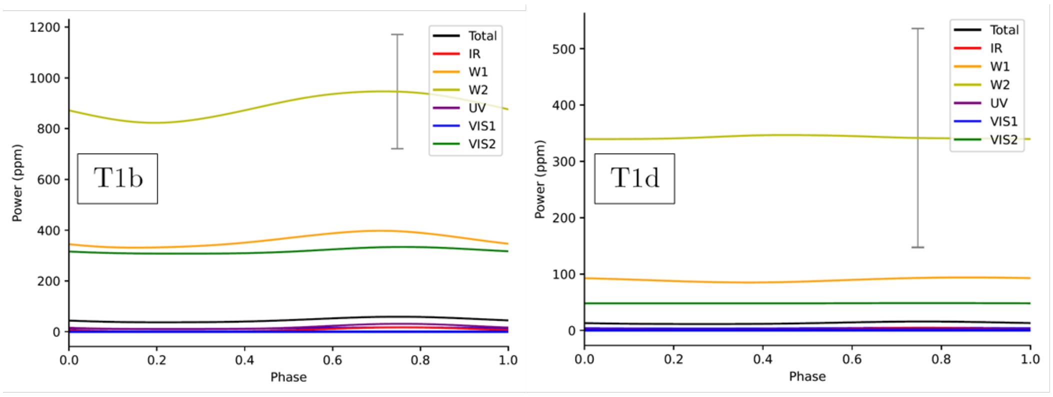

Figure 8.17: Phase curves for **(A)** TRAPPIST-1b and **(B)** TRAPPIST-1d. $\mathrm{p_s} = 10$ bar.

Figure 8.17 shows the phase curves of the two planets, including the contributions of the six spectral bands. TRAPPIST-1b transits at a phase of 0.20, and TRAPPIST-1d at 0.042. In all cases studied here, the W2 band which is the water vapour window between 7.7 and 20 microns, dominates all other regions, due to the planetary flux being large and the stellar flux of TRAPPIST-1 being comparatively weak in this region (see Figure 8.16). The W2 band would therefore be the best one to probe out of all the others to detect the signal of a secondary eclipse. These wavelengths are also included in the spectral range of the MIRI instrument of JWST, which is $[4.9, 28.3]\ \mu\mathrm{m}$. The peaks of the W2 contribution in (phase, amplitude [ppm]) coordinates are (0.72, 946.7) for TRAPPIST-1b and (0.45, 346.8) for TRAPPIST-1d. The minimum amplitudes are (0.20, 822.96) and (0.042, 339.56) respectively.

When observing the W2 band, one would therefore see an eastward hot spot shift on both planets, even though the temperature map of TRAPPIST-1d as well as its outgoing radiation map in the IR band indicate a westward shift. The error binned over the MIRI/LRS range provided by PANDEXO (5 to 14 microns), for 5 eclipses, is about 224.98 $\approx$ 225 ppm for TRAPPIST-1b and about 194.28 $\approx$ 194 ppm for

TRAPPIST-1d. From the maximum amplitudes indicated above, and assuming that they can be compared to the above errors, we would expect at most a 4.2σ detection of the eclipse signal when observing 5 eclipses of TRAPPIST-1b, and a 1.8σ detection for TRAPPIST-1d. Characterization based on the phase curves would likely not be possible, since the noise would dominate the shape of the phase curves.

8.3 1 bar surface pressure

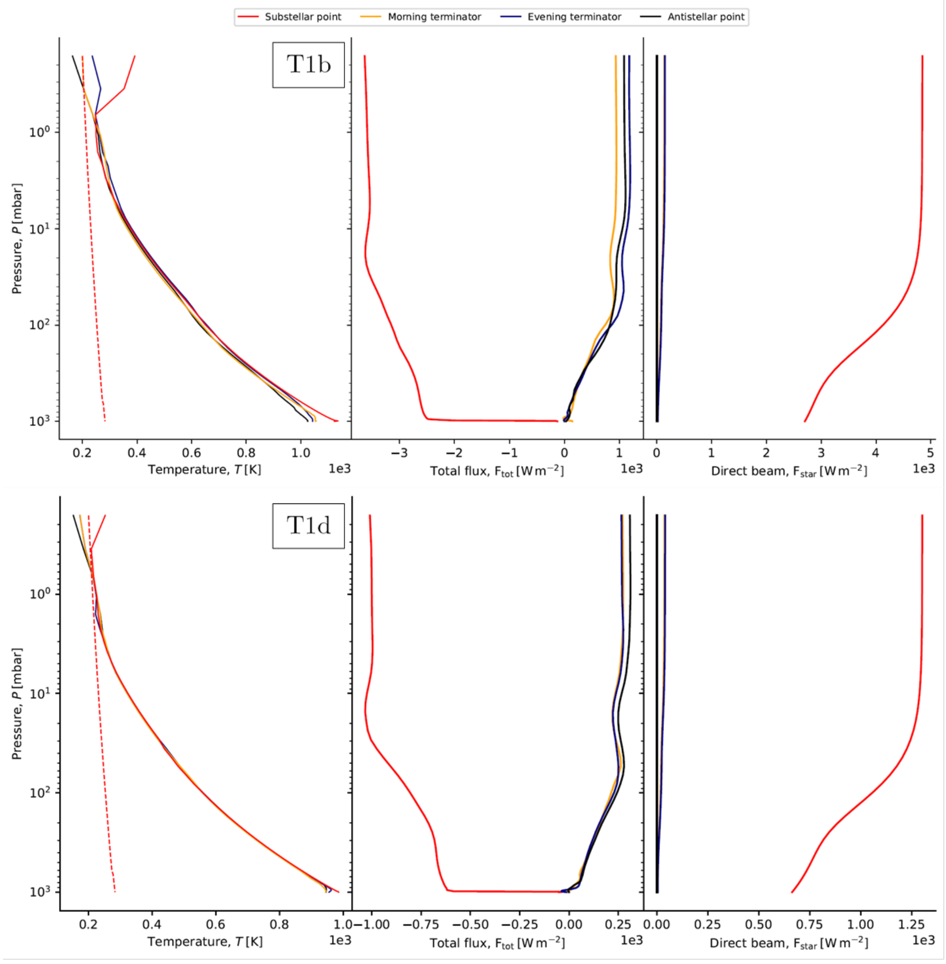

Figure 8.18: Vertical **(Left)** temperature, **(Middle)** total flux, and **(Right)** direct beam profiles of TRAPPIST-1b and TRAPPIST-1d at their substellar and antistellar points, and on the morning and evening terminators, assuming a surface pressure of $p_s = 1$ bar.

In the second case, we reduced the surface pressure to 1 bar, which represents the scenario of a planet with about 4% of Earth's outgassed water inventory.

Figure 8.18 is analogous to Figure 8.5. The surfaces of TRAPPIST-1b and TRAPPIST-

1d reached 1110 K and 983 K respectively. The profiles indicate supersaturation above about 3.5 mbar on TRAPPIST-1b and 6 mbar on TRAPPIST-1d, which is about an order of magnitude deeper than in the 10-bar case. This time there is no inversion in the deeper layers, and we see a greater difference between the temperatures of the different points indicated on Figure 8.1. These profiles also indicate a relatively small difference between the surface temperatures of both planets, as was the case in the 10-bar case. The total flux in the 1-bar case has a sharp gradient near the ground, probably due to the fact that a lot of stellar flux is able to reach the ground, as we can see on the plots to the right of Figure 8.18.

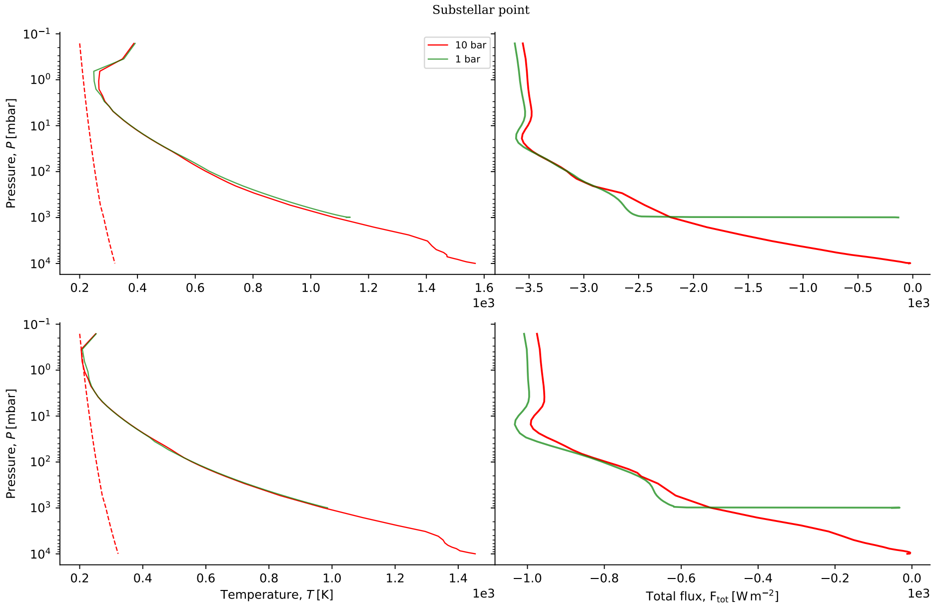

Figure 8.19: Vertical **(Left)** temperature and **(Right)** total flux profiles of TRAPPIST-1b **(Top)** and TRAPPIST-1d **(Bottom)** at their substellar point, for surface pressures of 1 **(Green)** and 10 **(Red)** bar.

Since the radiating temperature stays the same in both cases, the main effect of decreasing the surface pressure from 10 bar to 1 bar is to increase the pressure range over which we are extrapolating the profile along the adiabat by a factor of 10. This should increase temperatures by a factor of $10^{\frac{R}{c_p}}$, or about 1.77. This is close to what

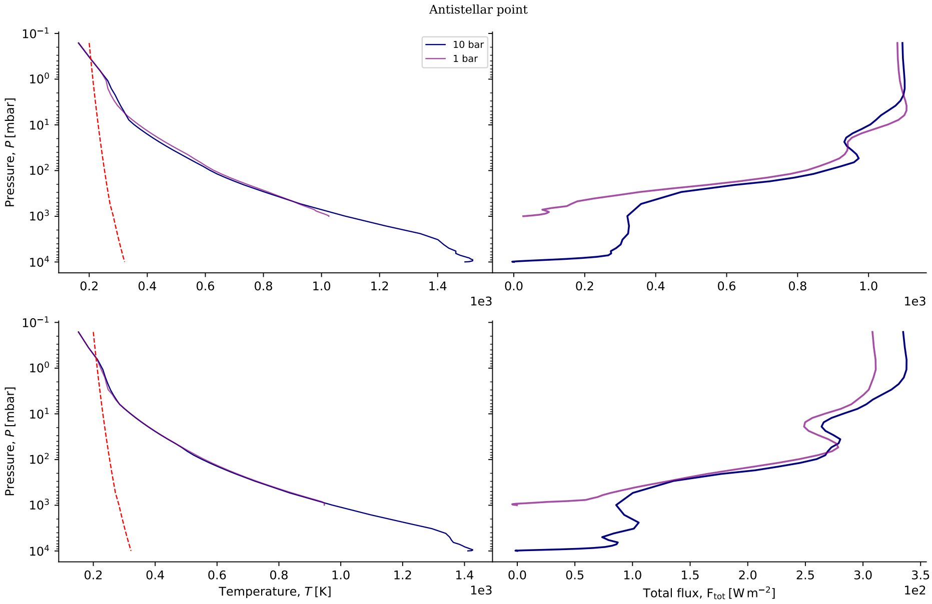

Figure 8.20: Vertical **(Left)** temperature and **(Right)** total flux profiles of TRAPPIST-1b **(Top)** and TRAPPIST-1d **(Bottom)** at their antistellar point, for surface pressures of 1 **(Purple)** and 10 **(Blue)** bar.

the results show, but the 10-bar case has the additional feature that there appears to be a non-convective region near the surface, which somewhat reduces the warming relative to the expected value. A comparison between the 1 bar and 10 bar cases is displayed on Figures 8.19 and 8.20.

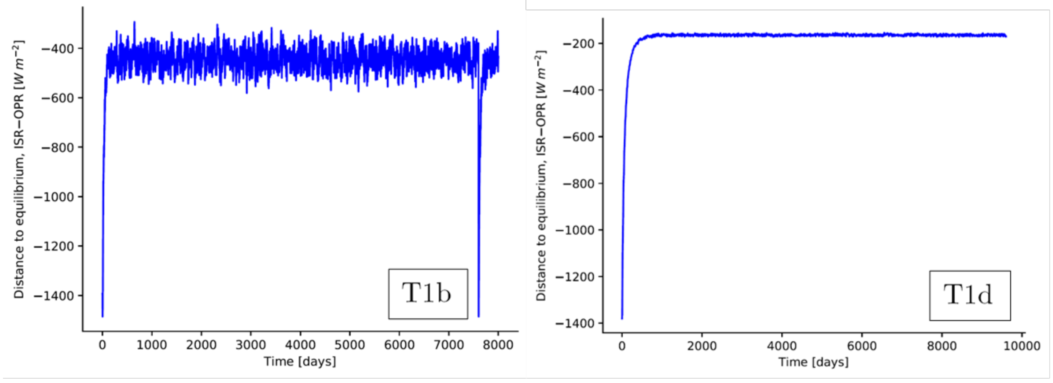

Figure 8.21: Evolution of the distance to equilibrium for **(A)** TRAPPIST-1b and **(B)** TRAPPIST-1d. $p_s = 1$ bar.

Figure 8.21 shows the evolution of the distance to radiative equilibrium at the TOA, by the same method as before. A relative equilibrium is reached after about 1000 days for both planets. Similarly, no clear upward or downward trend is shown by the time series of the temperature and net flux displayed on Figure 8.22.

Given the similar features with the 10-bar case, some figures have been moved to the appendices. Here we will only explore the main differences observed between the two surface pressure cases. The contribution function peaks seen on Figure A.1 are at the same pressure levels as in the 10-bar case, though lower down in height coordinates because nine bars of water vapour have been removed from the bottom layers. There is no half surface pressure peak this time, as these layers have not reached a high enough temperature to radiate through the windows of water vapour or through the visible and UV regions.

Figures 8.23 and 8.24 compare the global temperature maps at 500 mbar and 1 bar for both planets. Across the vertical extent of the atmosphere, TRAPPIST-1b shows vertically extended high amplitude Rossby waves from 1.1 to 877 mbar. Others of smaller amplitude can be seen between 0.4 and 200 mbar as well. On TRAPPIST-1d, we can see high amplitude Rossby waves between about 0.4 and 4.9 mbar, from 19 to 66 mbar, and from 98 to 905 mbar. We also see smaller amplitudes Rossby waves from 0.7 to about 808 mbar. At the 500 mbar level, the pattern of the temperature maps is different at $\mathrm{p_s = 1\,bar}$ from $\mathrm{p_s = 10\,bar}$. At $\mathrm{p_s = 10\,bar}$ and at the 500 mbar level, TRAPPIST-1b shows a shifted but well-defined hot spot around 60° west of the substellar point, while the temperature map of TRAPPIST-1d is almost uniform. Both planets show winds that seem mostly dominated by the pattern of the jet at all latitudes. At the same level but at $\mathrm{p_s = 1\,bar}$, the temperature maps of both planets exhibit a larger contrast.

In addition, the pattern of the winds is not dominated by the jet but by the smaller-

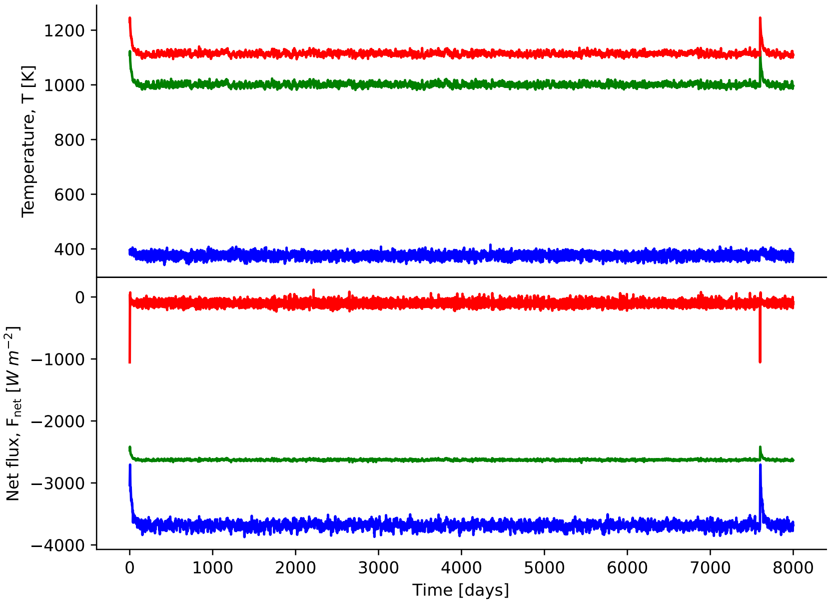

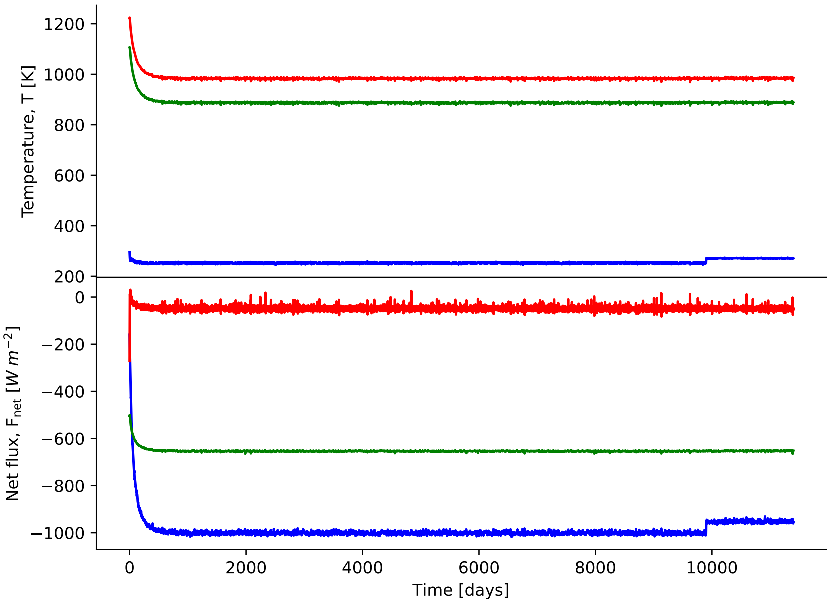

Figure 8.22: Time series of temperature and total flux over simulated time for TRAPPIST-1b **(Top)** and TRAPPIST-1d **(Bottom)**, at the top (blue), middle (0.5 bar, green), and bottom (red) of the atmosphere. $p_s = 1$ bar.

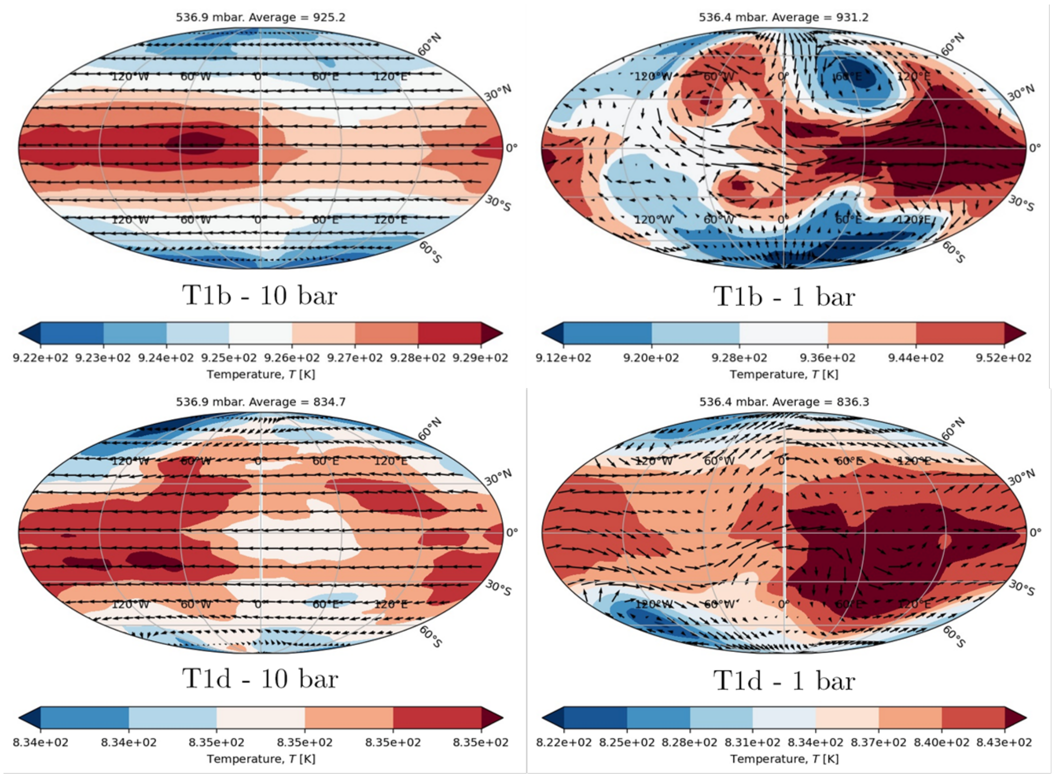

Figure 8.23: Global temperature maps at 500 mbar for both planets, also averaged over one Earth day.

scale Rossby circulation. At the 1 bar pressure level, the temperature and wind patterns show a similar picture to the one described above, except that in the $\mathrm{p_s} = 1\mathrm{bar}$ case, this level is close to the surface and the pattern shows a hot spot mostly centred on the substellar point, along with Rossby waves that are not present in the $\mathrm{p_s} = 10\,\mathrm{bar}$ case. The 536 mb TRAPPIST-1b case at $\mathrm{p_s} = 1\mathrm{bar}$ in particular looks like a snapshot of a case with significant time evolution, though it is a time-average over one Earth day like the other maps. This high variability between the different cases, including near the top of the atmosphere for the 10-bar case, might affect observational strategies.

Figure 8.25 shows global maps of the distance to saturation, indicating condensing

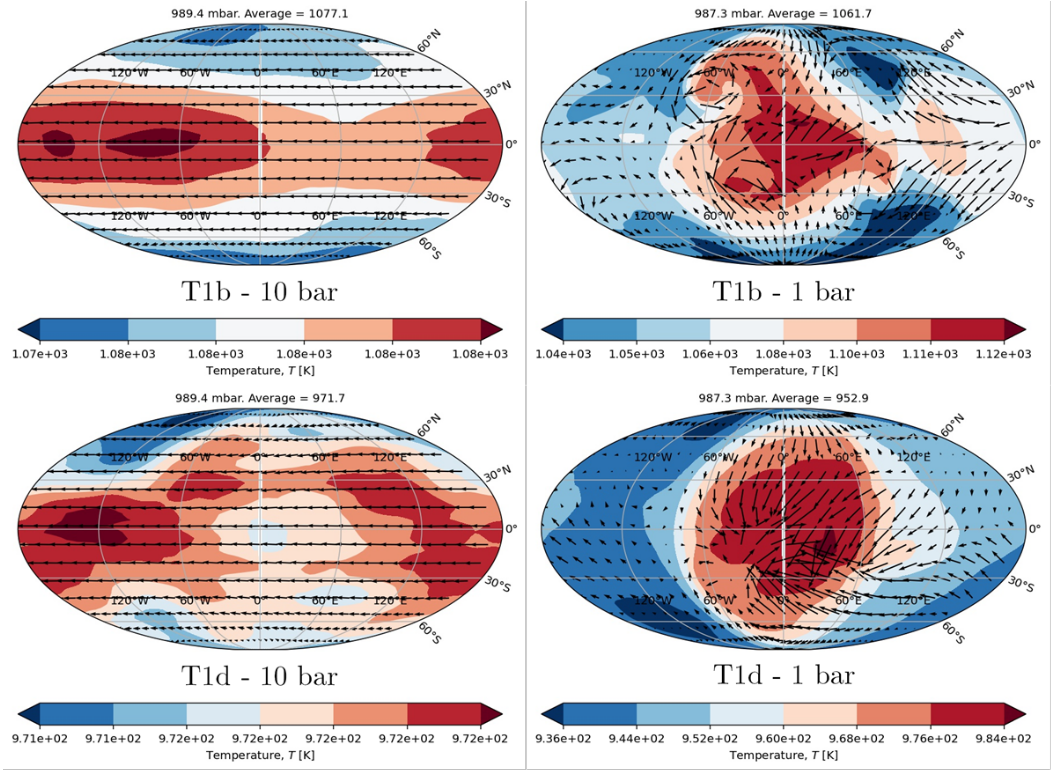

Figure 8.24: Global temperature maps at 1 bar for both planets.

regions. The 1D profiles on Figure 8.18 suggested an deepening of the saturated regions relative to the 10-bar case. On TRAPPIST-1b, condensation is restricted to layers above about 0.4 mbar, only on the nightside. On TRAPPIST-1d they can be seen on the nightside at the first two top layers, and below that their distribution is spread to both the nightside and the dayside, down to about 1.6 mbar.

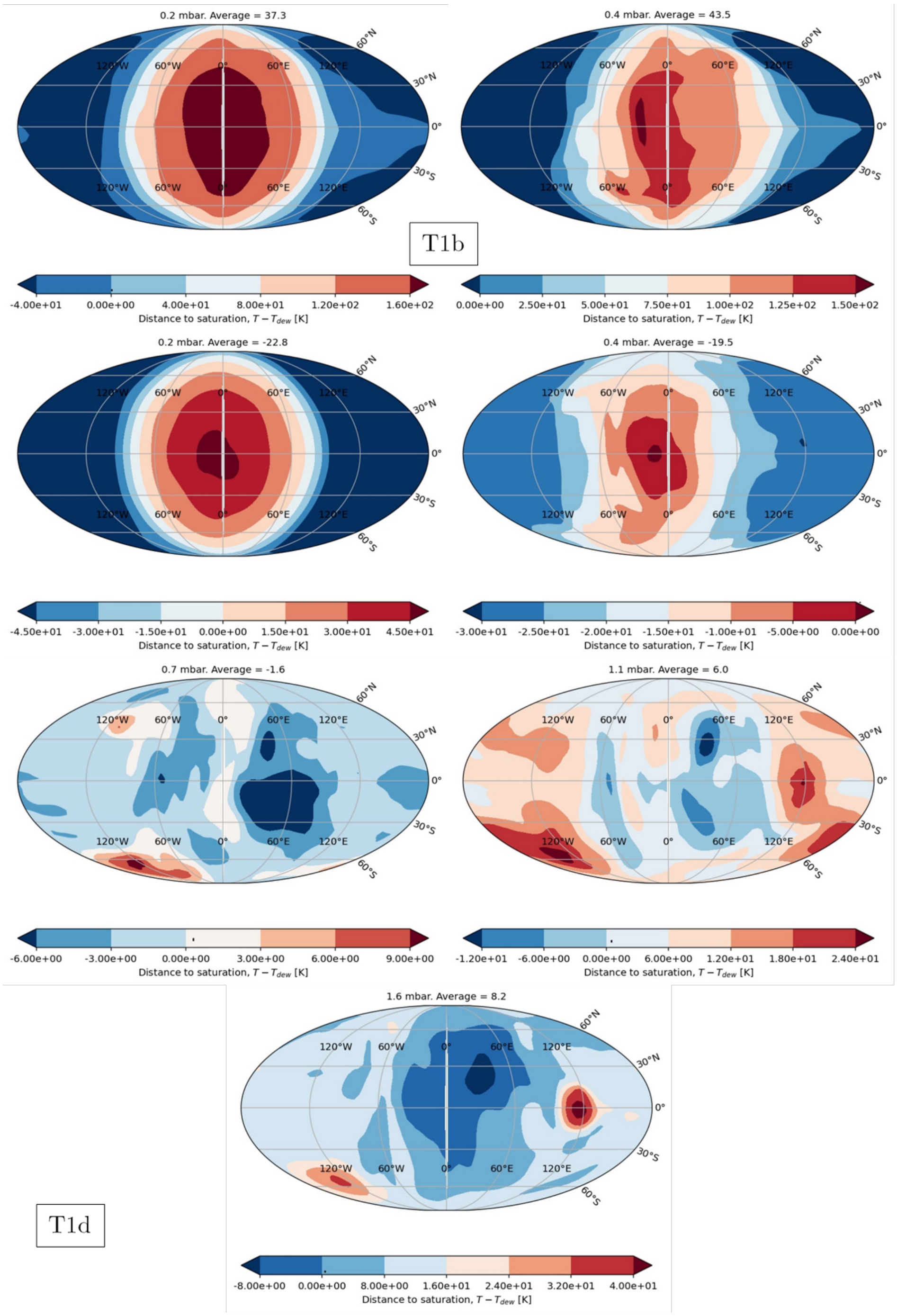

Figure 8.25: Global saturation maps at selected altitudes. $p_s = 1$ bar.

Figure 8.26 shows a substellar OPR of 1800 $\mathrm{W\,m^{-2}}$ on TRAPPIST-1b and an eastward hot spot shift. TRAPPIST-1d also has an eastward shift but mostly around the poles, with a substellar OPR of 480 $\mathrm{W\,m^{-2}}$. Figures A.5 and A.6 isolate the OPR in each band. On TRAPPIST-1b, the IR contribution coming from the TOA seems centred on the substellar point. The UV and visible fluxes are weak given the lower surface pressure, and their contributions near the boundary layer reflect this. The radiation in the window W2 seems to come from around 80 mbar, whereas W1 seems to be radiating from both the 8 mbar and the 80 mbar peaks of the contribution function.

We can also see that the eastward hot spot shift is mainly caused by radiation coming from the windows of water vapour and not from the IR band. The same observations can be made for TRAPPIST-1d, except that the CFF peaks are centred around 4.5 and 55 mbar.

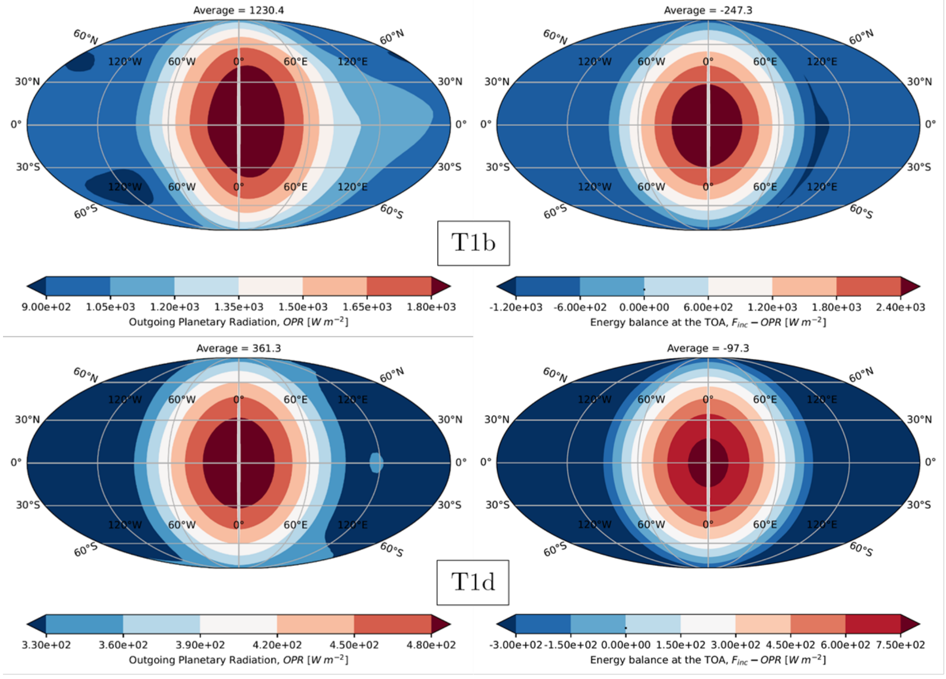

Figure 8.26: Global bolometric TOA budget maps. $\mathrm{p_s} = 1$ bar.

The phase curves seen on Figure 8.27 have amplitudes that are somewhat larger than in the 10-bar case because of the smaller opacity and the larger amount of radiation able to escape to space. The W2 window region again dominates the other bands. Both planets transit at a phase of 0.358. The peaks of the W2 contribution in (phase, amplitude [ppm]) coordinates are (0.905, 1015.95) for TRAPPIST-1b and (0.0632, 348.54) for TRAPPIST-1d. The minimum amplitudes are (0.358, 847.01) and (0.358, 344.94) respectively. When observing the W2 band, one would therefore see an eastward hot spot shift on TRAPPIST-1b and an westward one on TRAPPIST-1d, where the shift is caused by radiation coming from the polar regions. This slightly larger signal yield better confidence levels than in the 10-bar case. The MIRI errors for TRAPPIST-1b and d yield a 4.5σ and 1.8σ detection respectively. Despite the higher confidence in detection, characterization would still be dominated by the noise.

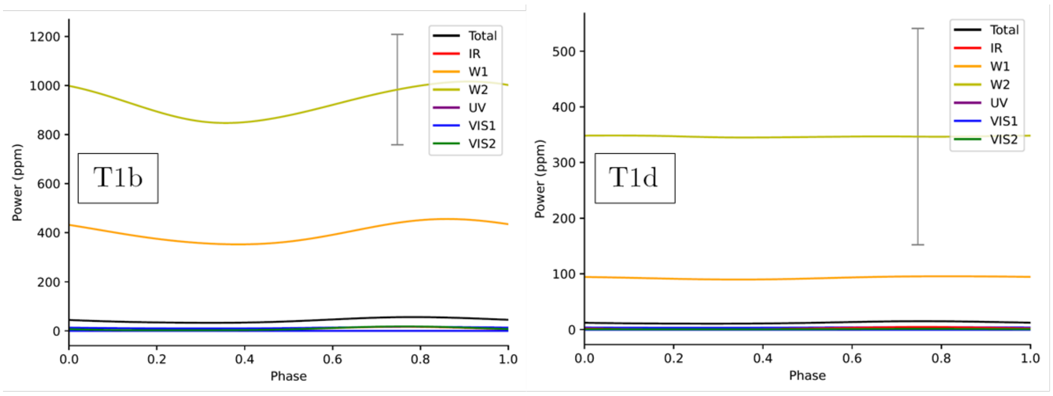

Figure 8.27: Phase curves for **(A)** TRAPPIST-1b and **(B)** TRAPPIST-1d. $p_s = 1$ bar.

8.4 260 bar surface pressure

In the third case, we increased the surface pressure to 260 bar in order to explore the scenario of an Earth-like initial surface water reservoir on each planet.

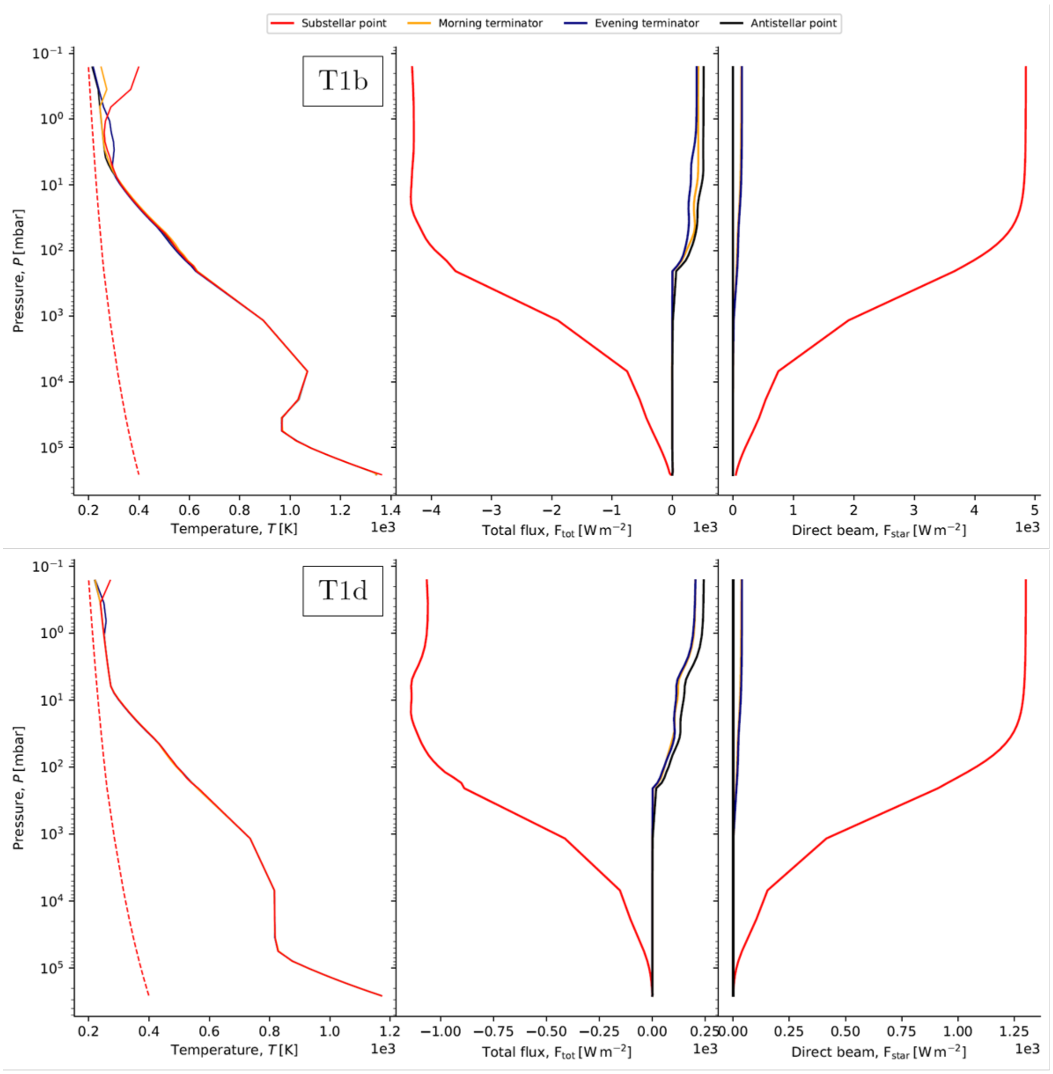

Figure 8.28: Vertical **(Left)** temperature, **(Middle)** total flux, and **(Right)** direct beam profiles of TRAPPIST-1b and TRAPPIST-1d at their substellar and antistellar points, and on the morning and evening terminators, assuming a surface pressure of $p_s = 260$ bar.

Figure 8.28 shows that the surfaces of TRAPPIST-1b and TRAPPIST-1d reached 1364 K and 1171 K respectively, but these are not converged values. At this surface pressure though, the profiles do not intersect the condensation curve at any level, even on the nightside. However, we cannot yet rule out the possibility that this may be due to the profiles not being converged solutions. TRAPPIST-1b features three inversions, one due to stellar heating at the TOA, on the dayside, and two around 7 and 40 bar, indicating that the atmosphere has an extended non-convective region between about 6 and 30 bar. TRAPPIST-1d has a weaker inversion at the TOA, mostly around the substellar point. The profile becomes near-isothermal from 30 to 7 bar, indicating a potential inversion and a non-convective region forming. The lower layers below the inversion follow the dry adiabatic lapse rate. Though these simulations are not fully converged, it is significant that the low levels have cooled to sub-adiabatic conditions and exhibit the beginnings of radiative or even inversion layers in the deep atmosphere. The zeroed deep atmosphere net flux might make it look like this is a converged solution, but in fact the very optically thick atmosphere means that the flux gradients will be very small, leading to small radiative cooling or heating and very long equilibration times. In addition, both planets have been initialised with the same profile as the other cases, which is also adding to the equilibration time.

Figure 8.29 shows a much slower convergence toward an equilibrium compared to the previous two cases. As explained in Section 8.1, an atmosphere with 260 bar of water vapour is expected to equilibrate after a much longer simulation time than this work has had time to use. Turbet et al. (2019) estimated that the number of simulation days required is likely on the order of 10^6 days (Martin Turbet, personal communication). The TOA balance could come into balance fairly quickly however, since it is just determined in the upper atmosphere. The relaxation time of the

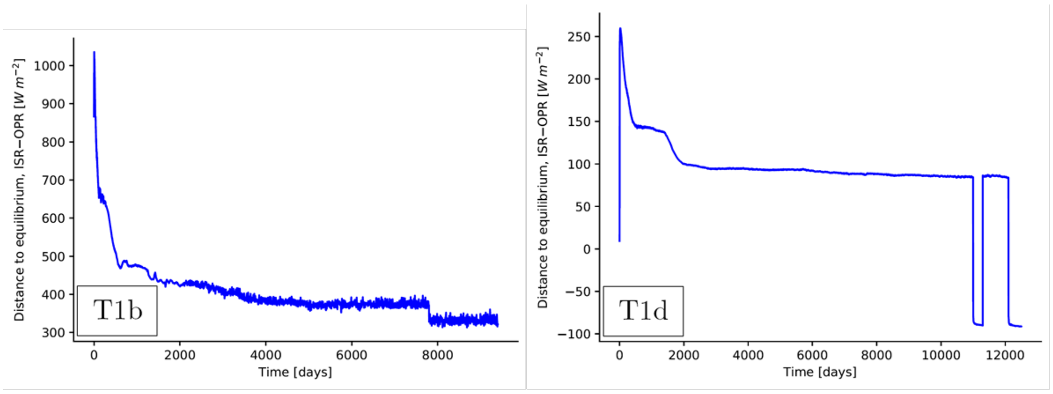

Figure 8.29: Evolution of the distance to equilibrium for **(A)** TRAPPIST-1b and **(B)** TRAPPIST-1d. $p_s = 260$ bar.

deep atmosphere, if it is not convective, is very long, so one expects the deep atmosphere to keep evolving for a long time even after the TOA balance settles down. Longer simulations will therefore be required to investigate the potential effect of the contribution of the deep layers to the TOA energy budget in high-temperature regimes.

The jump seen from day 7899 to 7900 is due to a decrease in OPR from a sudden heating at the top of the atmosphere. Figures 8.30 and 8.31 show the temperature profiles of TRAPPIST-1b at days 7899 and 7900. Similarly, Figures 8.32 to 8.37 show the temperature profiles of TRAPPIST-1d at each of the jumps seen on Figure 8.29T1d. They show a jump in top-of-atmosphere temperature that translates into the sudden increase in OPR. This sudden heating seems to be the main cause for the profile not intersecting with the dew point curve at this surface pressure. This looks like a numerical instability, oscillating in the case of TRAPPIST-1d, and it will be thoroughly investigated in the next steps of this work.

The time series plots shown on Figure 8.38 confirm that TRAPPIST-1b has not finished warming up, and TRAPPIST-1d has not finished cooling down. The total flux at the surface of the inner planet is still increasing with a rate of $1.2 \cdot$

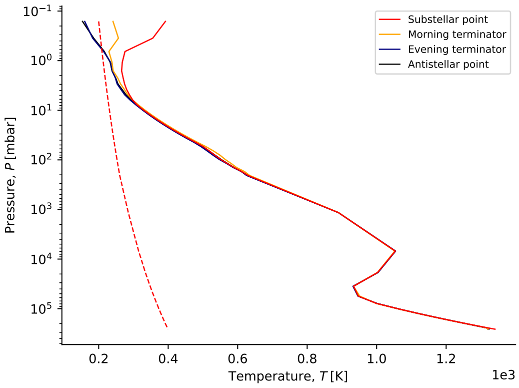

Figure 8.30: TRAPPIST-1b - Day 7899

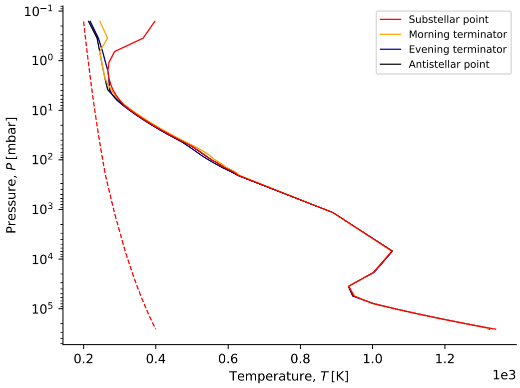

Figure 8.31: TRAPPIST-1b - Day 7900

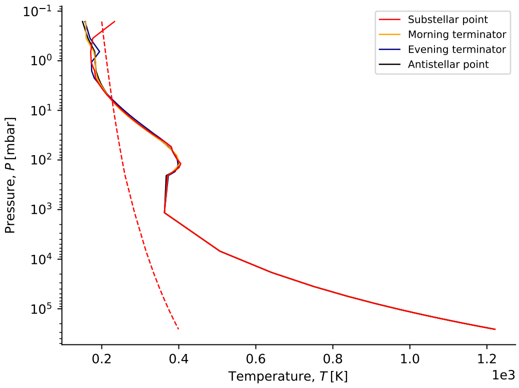

Figure 8.32: TRAPPIST-1d - Day 10999

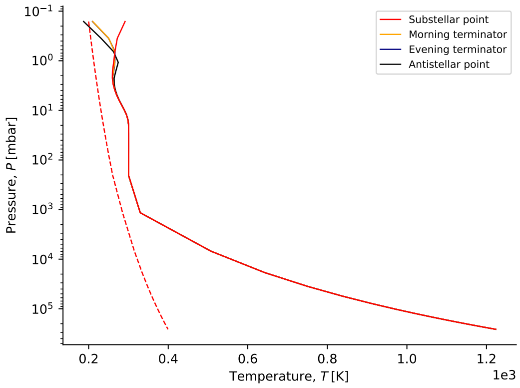

Figure 8.33: TRAPPIST-1d - Day 11000

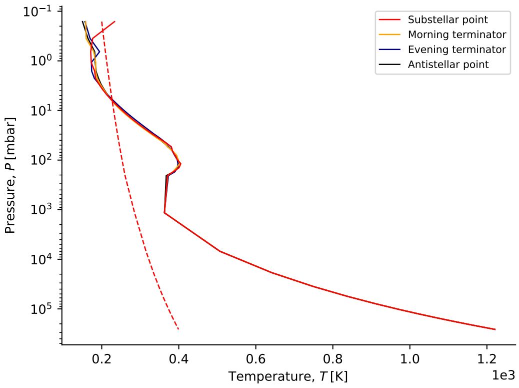

Figure 8.34: TRAPPIST-1d - Day 11299

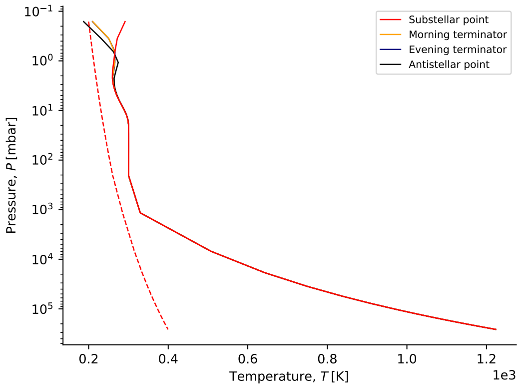

Figure 8.35: TRAPPIST-1d - Day 11300

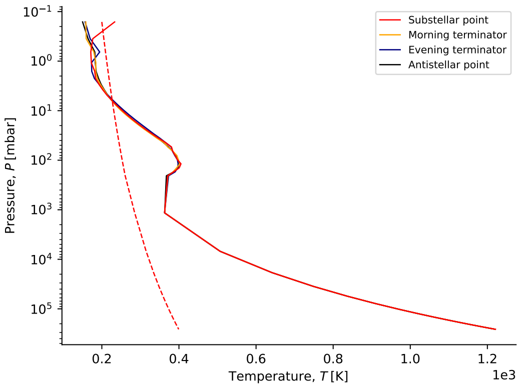

Figure 8.36: TRAPPIST-1d - Day 12099

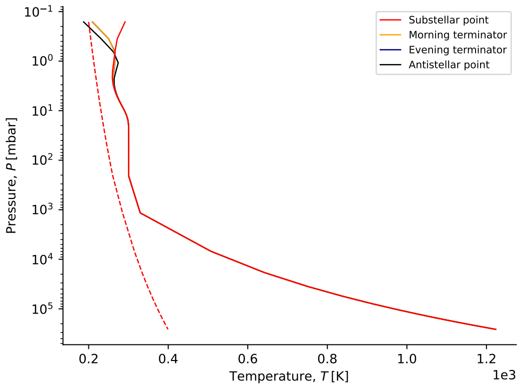

Figure 8.37: TRAPPIST-1d - Day 12100

$10^{-3}\,\mathrm{W\,m^{-2}\,day^{-1}}$. The flux of TRAPPIST-1d at the surface is decreasing with a rate of about $0.28\,\mathrm{W\,m^{-2}\,day^{-1}}$ after day 1000. As above though, the initial conditions for both planets were set to the same adiabatic solution as in the other surface pressure cases, using a surface temperature of 1225 K. This is a colder temperature than the one expected for the 260 bar case, which in one dimension was closer to 1800 K.

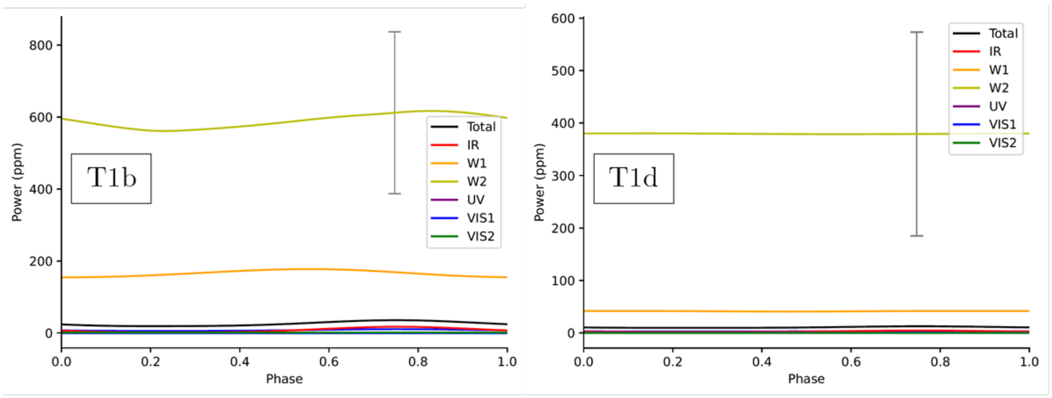

Figure 8.39: Phase curves for **(A)** TRAPPIST-1b and **(B)** TRAPPIST-1d. $\mathrm{p_s} = 260$ bar.

The phase curve of TRAPPIST-1b seen on panel T1b of Figure 8.39 shows a smaller amplitude that in previous cases, while the one corresponding to TRAPPIST-1d

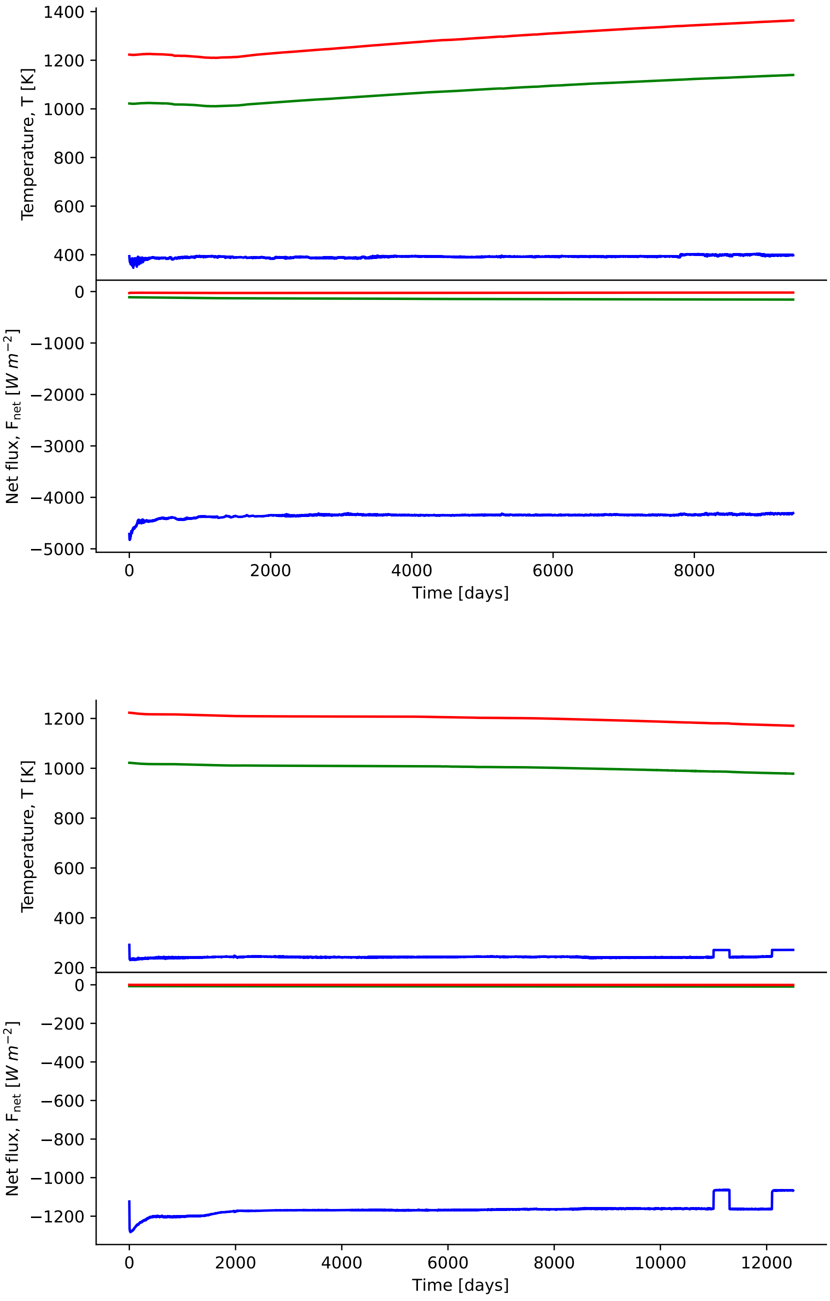

Figure 8.38: Time series of temperature and total flux over simulated time for TRAPPIST-1b **(Top)** and TRAPPIST-1d **(Bottom)**, at the top (blue), middle (130 bar, green), and bottom (red) of the atmosphere. $p_s = 260$ bar.

slightly increased in amplitude, which might be explained by the fact that the outer planet hasn't yet converged and is still cooling. The variations of the phase curve decreased to under 2 ppm however. TRAPPIST-1b transit at a phase of 0.232 and TRAPPIST-1d at 0.579. The peaks of the W2 contribution in (phase, amplitude [ppm]) coordinates are (0.832, 616.84) for TRAPPIST-1b and (0.137, 380.35) for TRAPPIST-1d. The minimum amplitudes are (0.232, 561.06) and (0.579, 380.35) respectively. The W2 band would show an eastward hot spot shift on TRAPPIST-1b, barely any shift on TRAPPIST-1d. The SNR resulting from the MIRI errors for TRAPPIST-1b and d yield a 2.7σ and 2σ detection respectively. In both cases, and especially for TRAPPIST-1d, the noise would dominate the amplitude variation of the phase curves.

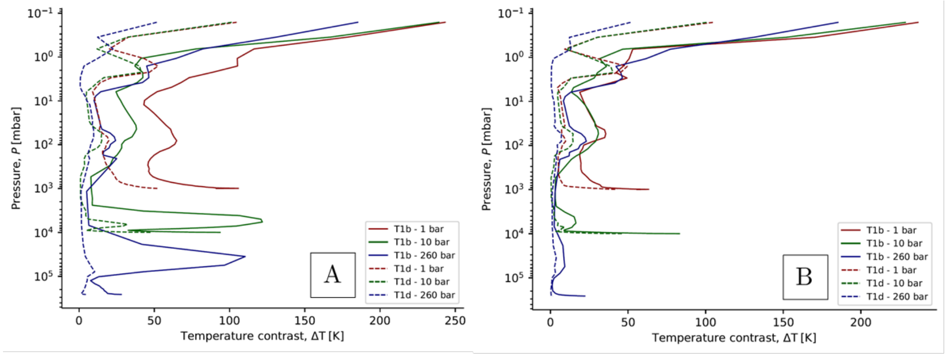

Figure 8.40: **(A)** Global and **(B)** equatorial temperature contrast for all cases.

Figures 8.40 show the temperature contrast between the day side and the night side of each planet and in each of the three surface pressures explored here. Panel A shows the difference between the maximum and minimum temperature across all latitudes, and Panel B shows the difference restricted to the equator. Assuming a surface pressure of 1 bar, the global surface temperature difference is about 91 and 52 K on TRAPPIST-1b and d respectively. When restricted to the equator, the values become 56 and 43 K. The inner planet's temperature contrast does not go below 43 K globally and 19 K on the equator, at any level. The outer planet's does get down to about 9 K globally and 5 K on the equator. When we increase the surface pressure to 10 bar, the global surface temperature contrast changes by less than 4 K, but the equatorial contrasts increase to 83 K and 47 K for both planets. The global minima across the column are much smaller, sitting at 8 K and 0.9 K. The equatorial minima also decrease to 3 K and 0.4 K. The global and equatorial surface temperature contrasts decrease dramatically when we increase the surface pressure to 260 bar. Though this simulation was not converged, we see contrasts of 28 K and 5 K respectively. At the equator, they reach 22 K and 1.5 K. The global minima decreased again from the 10-bar case to reach 5 K and 0.7 K. So did the equatorial minima. They reached 1.2 K and 0.36 K.

A few trends can be seen appearing here. TRAPPIST-1b always achieves a higher temperature contrast than TRAPPIST-1d given the same surface pressure. This is mainly due to the smaller instellation received by TRAPPIST-1d, though the lower gravity could also play a role by increasing the opacity. Additionally, the more massive the atmosphere is on a given planet, the smaller the contrast will be. This is mainly due to the larger thermal inertia of more massive atmospheres.

Figure 7.3 shows by the rotation criterion that both planets should be in the WTG regime given the atmospheres postulated in this work, and that the outer planet should be deeper in the WTG regime than the inner one. The cases studied here confirm that WTG conditions apply on both planets. The cases that are the closest to the WTG regime are TRAPPIST-1d at 10 and 260 bar, which is consistent with our previous hypothesis. In all cases however, the equator is closer to the WTG regime than the higher latitudes, which is also consistent with the results obtained by Pierrehumbert and Ding (2016).

8.5 Discussion

In this section, we will discuss the main results obtained with the 3D simulations.

The limitation of condensation to the top of the atmosphere in the post-runaway case is exactly what is expected from the 1D results, in that the only way the planet can equilibrate is by making the condensation region thin enough. In these simulations we get the additional effect that dayside shortwave heating suppresses condensation; the shortwave stellar heating was not discussed in Boukrouche et al. (2021). These calculations indicate that although TRAPPIST-1d is close to the edge of the habitable zone, a "hot start" with a steam atmosphere keeps the planet hot and does not result in the condensation of a liquid ocean. This calculation does not include clouds, but there is some indication that upper level dayside clouds could form, unlike in the case of TRAPPIST-1b. This could potentially shield the planet from a runaway greenhouse effect, but the cloud forming layer is very limited on the dayside, whereas nightside upper clouds which have a warming effect should be prevalent.

In the case of both planets explored in this work, there is little horizontal temperature variation, except near the top of the model. This raises the question of what we can learn from three-dimensional simulations that we do not learn from one-dimensional ones. One answer is that the radiation balance is determined at the top of the model, and there are significant dayside-nightside variations there. These affect cloud formation, phase curves and the energy balance. Changing the surface pressure does not significantly affect what is happening at the top of the atmosphere, as the temperature profiles seem to imply. This is corroborated by Figure 8.20, which illustrates how the upper atmosphere is not very sensitive to just how deep the atmosphere is. This suggests that dynamic models with an artificially low surface pressure can nonetheless provide insight as to higher pressure atmospheres. An important feature of the higher pressures is the formation of non-convective layers near the bottom. The apparent radiative layers near the ground in the 10-bar case reduce the surface temperature below what would be expected for an atmosphere that is convective all the way to the ground. These non-convective layers can probably be captured by 1D models since the dayside-nightside contrast in the features is not great for thick atmospheres. Further work is needed to investigate this problem. If the low level profile is driven to some extent by stellar heating reaching the ground, there could be a dayside-nightside contrast, though dynamical transports might decrease it somewhat.

Another feature of note that the 3D simulations suggested is the relatively small difference in surface temperature between the inner and outer planets, though the radiating level temperatures of TRAPPIST-1d are consistently much colder than those of TRAPPIST-1b. This deserves a more thorough exploration, notably with longer simulations to fully converge high-surface-pressure simulations. However, the same result was found in the 1-bar case, which equilibrates much faster. This suggests that the surface temperature of post-runaway atmospheres is only weakly sensitive to the instellation level. From Figure 8 of Boukrouche et al. (2021), we expect the difference in equilibrium surface temperatures that we would obtain between the instellation levels of each planet to be about 361 K at $\mathrm{p_s} = 10$ bar and 326 K at $\mathrm{p_s} = 260$ bar. The difference obtained with the 3D simulations at 10 bar is 114 K, which is about three times smaller than the corresponding above value. However, it's worth noting that in these calculations, TRAPPIST-1d is in a runaway state, at least given a hot start. Cloud effects or a cold start could conceivably push the planet into a non-runaway state.

The preliminary study on the detectability of the modelled atmospheres found that spectroscopic observations of five secondary eclipses of TRAPPIST-1b could yield at most a 4.5σ confidence of a detection among the cases studied which, despite the approximations described in Section 7.4, suggests that TRAPPIST-1b is a suitable target for thermal emission observations. The maximum confidence level obtained for TRAPPIST-1d is 2σ, suggesting that it is not an appropriate target for this method. The detection prospects predicted by Lustig-Yaeger, Meadows, and Lincowski (2019) included the case of a 1 bar H_2O clear-sky atmosphere for both planets. The detection criterion used in this study was an SNR of 5, which exceeds the highest confidence levels obtained in this work. They found that achieving an SNR of 5 can be done with at least 50 to 60 eclipses, while TRAPPIST-1d would require more than a thousand eclipses. With a Venus-like atmospheric composition and a 1-bar surface pressure, Morley, Kreidberg, Rustamkulov, Robinson, and Fortney (2017) finds that 2-3 eclipses are sufficient to get a detection of TRAPPIST-1b, though at least 9 eclipses would be needed to reach the required 25σ confidence level required to resolve spectral features. TRAPPIST-1c and the outer planets all require a higher number of eclipses than would be reasonable to expect over the lifetime of JWST.

One limitation of this work is the assumption that in a pure steam scenario, only water would be present across the column. However, it is conceivable that other species would form by water dissociation and could be present in the steam atmosphere in chemical equilibrium. Figure 8.41 shows the absorption spectra of O2, O3, and H2, species that could form in the deeper layers of the atmosphere. While O2 and H2 are shown for a relatively high pressure and temperature to fit this context, O3 was only available at standard conditions or around the pressure level of the ozone layer on Earth, 50 mbar. Nevertheless, this graph suggests that while the infrared atmospheric windows of water vapour would likely remain optically thin, the optical and UV regions could become significantly more opaque due to the efficient absorption of ozone and O2. Dissociation of water and the formation of significant amounts of O2 and O3 in the atmosphere could drastically reduce the amount of shortwave radiation contributing to the outgoing planetary radiation.

Figures 5.6 and 8.8 both suggest that the infrared contribution to the OPR is cut at the uppermost pressure level, 0.1 mbar, and that a smaller pressure boundary at the TOA is needed to capture the part that is missed. Estimating the amount of $\mathrm{W\,m^{-2}}$ that is neglected with this upper bound will require new simulation runs using a pressure grid that encompasses the contribution function. Figure 7.5 shows that above about 250 mbar, which is below the peak contributions of the infrared region and the windows, the linear behaviour would likely make this amount relatively small compared to the amount captured by the pressure grid.

Some of the cases explored in this work resulted in high enough surface temperatures to melt silicate surfaces. The case of TRAPPIST-1b at $\mathrm{p_s} = 1$ bar case yielded surface temperatures below 1200 K, which is below the solidus estimated between about 1250 K and 1550 K by panels E and F of Figure 3 of Lichtenberg, Schaefer, Nakajima, and Fischer (2022). However, the $\mathrm{p_s} = 10$ bar case yielded 1568 K and 1454 K for the inner and outer planet respectively, which is enough to melt some forms of basalt, though not enough to reach the liquidus, visible in Figure 1 of Katz, Spiegelman, and Langmuir (2003). If a magma is formed, it may therefore be some mixture of solid and melt. The 260-bar case for TRAPPIST-1b is probably hot enough to form a magma ocean. The low levels are clearly not converged, but the fact that they are heating up suggests that they might reach magma ocean temperatures. Dorn and Lichtenberg (2021) found that the densities of TRAPPIST-1b and TRAPPIST-1d retrieved by Gillon et al. (2017) and refined by Agol et al. (2021) are consistent with at most $0.01\mathrm{wt}\%$ $\mathrm{H_2O}$ for the inner planet, though more likely less

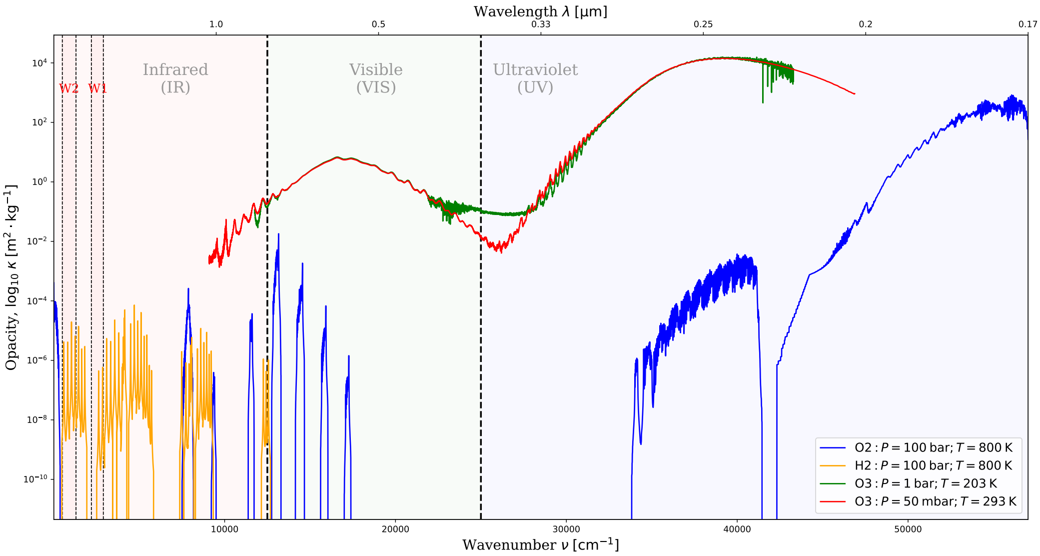

Figure 8.41: Absorption spectrum of O2, O3, and H2 in the regions provided by their respective sources. O2 and H2 were obtained from Gordon et al. (2017), O2 between 10^{-5} and 57027.59 cm^{-1}, and H2 between 15 and 27185 cm^{-1}. Both were chosen at $P = 100$ bar and $T = 800$ K. Serdyuchenko et al. (2014) provided O3 between 9090.91 and 46948.36 cm^{-1} at $P = 50$ mbar and $T = 293$ K. Delahaye et al. (2021) provided O3 between 11752.0950 43292.2170 cm^{-1} at $P = 50$ mbar and $T = 293$ K.

than that, and less than $0.001\mathrm{wt}\%$ $\mathrm{H_2O}$ for the outer planet. They suggested that if the water mass fraction is $x_{\mathrm{H_2O}} \geq 0.01\mathrm{wt}\%$, there is enough water to melt the mantle and dissolve water in it, thereby decreasing the transit radius, which would shift the density of the planet downward on a graph showing the radius as a function of mass. However, if $x_{\mathrm{H_2O}} < 0.01\mathrm{wt}\%$, there is little enough water that the mantle is not molten, and the water will preferentially reside in the atmosphere in the form of water vapour, which would inflate the atmosphere (Turbet et al., 2019) if they are indeed in a runaway greenhouse state and shift the planet's density upward on the same graph.

Even if TRAPPIST-1b has the maximum amount of water allowed by the density estimate, $0.01 \mathrm{wt}\%$, it likely does not have enough water to feature a magma ocean and a molten mantle that would store water and decrease the planet's transit radius (Tim Lichtenberg, personal communication). Given this, if we do not observe an inflated atmosphere, it could be a sign that the planet is not undergoing a runaway greenhouse effect. It may have been born dry or lost all its water in the early stages of planetary evolution when the star may have been much more active, or it could have already reached a post-runaway climate state. This is also likely true for TRAPPIST-1d, as it is only consistent with less than $0.001 \mathrm{wt}\%$ water. Therefore, the surface water inventory of these inner planets may be limited, and the scenarios included in this work with surface pressures of 1 and 10 bar seem more likely than those with 260 bar of water. The simulations performed in this work could also represent an earlier stage of evolution when these planets could have started off with little enough water to avoid melting their mantles, but enough to enter a transient runaway greenhouse state. Then by losing this water to space, they would yield the densities that we observe today. Given the age of the system, estimated at 7.6 ± 2.2 Gyr by Burgasser and Mamajek (2017), they could have had enough time to undergo this climate transition.

9 | Synthesis

The one-dimensional work presented in this thesis shed light on key aspects of runaway greenhouse theory and expectations from observations of planets in a runaway greenhouse or hothouse climate state. Namely, planets undergoing a runaway greenhouse effect will warm up uncontrollably until one of three events occur. The first of these events is the dry adiabatic region eating into the radiating layers so that the latter regain their dependency on the surface temperature, warm up as the surface continues heating up, and increase their contributions to the outgoing radiation to space. Not only does this allow the planet to cool down again, it also implies that the runaway greenhouse effect necessarily ends with a thin, if at all present, condensing region located at the uppermost layers of the atmosphere. The second event is the surface and the relatively deeper layers of the atmospheres becoming hot enough to shift the peak of their emission to the near-IR, where important atmospheric windows of water vapour are located - two of them designated as W1 and W2 in this work. Then radiation coming from these layers can pass through the atmosphere without being completely absorbed and escape to space, increasing the outgoing longwave radiation. When the deeper layers and the surface reach about 2000 K, they begin to have non-negligible amounts of emission in the optical and ultraviolet regions of the spectrum. This is the third event, and because water vapour is relatively optically thin in these regions, the outgoing shortwave radiation can increase. When the third event is triggered, the equilibrium surface temperature of the planet can slightly decrease compared to the effect of the increase in outgoing infrared radiation alone.

The three-dimensional work introduced the effect of dynamics on the 1D results, which allowed a more thorough exploration of condensation, Rossby circulation, and observational prospects for the two planets chosen for the modelling, TRAPPIST-1b and TRAPPIST-1d. A water-rich atmosphere with a surface pressure of 1 or 10 bar would likely prevent dayside condensation on TRAPPIST-1b, which would be in line with the conclusions of Turbet et al. (2021), but it would allow for both nightside and dayside condensation on TRAPPIST-1d, though restricted to layers above about 1.6 mbar. Increasing the surface pressure to 260 bar would likely result in a cloud-free atmosphere on both planets. Condensation is restricted to the uppermost layers of the atmosphere in all cases studied here, which is consistent with the arguments made based on the one-dimensional simulations which showed that equilibration after a runaway greenhouse effect requires the condensing region to be a thin enough layer near the TOA. Near the ground, non-convective regions are observed to form with surface pressures higher than 10 bar. They might contribute to the small difference in surface temperatures observed between TRAPPIST-1b and TRAPPIST-1d, which might be an indication that the surface temperatures of post-runaway atmospheres have a relatively weak dependence on instellation. This however warrants further investigation. Rossby waves are present on both planets for all surface pressures explored, however their extent and amplitude decrease significantly as the surface pressure increases. TRAPPIST-1b achieves a higher temperature contrast overall than TRAPPIST-1d given the same surface pressure, due to the smaller instellation received by the outer planet, though its smaller surface gravity could also play a role by increasing the opacity of the atmosphere. The WTG regime (Pierrehumbert & Ding, 2016) is approached the closest by TRAPPIST-1d with a surface pressure of 260 bar.

Given current observational constraints and theoretical models of water partitioning scenarios between the interior and the atmosphere of rocky planets, we do not expect TRAPPIST-1b and TRAPPIST-1d to have important outgassed water inventories. If they started out with significant water inventories, either they did not have enough water to melt their surfaces, which would mean an inflated atmosphere if the runaway greenhouse threshold is passed, or they did, and they already underwent a runaway greenhouse effect that decreased their outgassed water inventories enough to reach a post-runaway climate state with a limited remaining reservoir of water consistent with the current masses and radii measured. This means that the scenarios with surface pressures of 1 and 10 bar are more likely than the case with 260 bars of water vapour.

Additional observations of this system are planned, notably by JWST, which should greatly increase the amount and quality of the data that we have on these planets. If JWST/MIRI obtains more than a 4.5σ detection on TRAPPIST-1b by combining 5 secondary eclipse observations, the planet likely has something less opaque than a 1-bar pure steam atmosphere. The maximum confidence level reachable in the cases explored for TRAPPIST-1d is 2σ.

Many avenues are open for future investigations. Further modelling in both 1D and 3D using profiles that are not fully convective could be used to check the presence of non-convective layers near the ground for surface pressures higher than 10 bar. Notably, given that the 3D simulations presented here were initialised using the same surface temperature, future simulations would be initialised to a hot-start on the adiabat to see if the low levels cool down to a sub-adiabatic condition. Adding longwave and shortwave scattering to the model is a natural next step for this work, and estimating its impact around an M star like TRAPPIST-1 would be useful to assess the validity of the present results. More extensive explorations of instellation ranges with longer 3D simulations would help to check the apparent result that the equilibrium surface temperature of post-runaway atmospheres is only weakly dependent on instellation. TRAPPIST-1d can conceivably escape a runaway greenhouse effect due to potential cloud effects and a cold start, although the result that clouds are preferentially forming on the nightside makes the possibility of this eventuality unclear. Future simulations initialised with a cold start at 1 and 10 bar could explore whether the climate of the planet still tends toward a runaway greenhouse effect. The investigation of the effects of clouds around different types of stars is still at its early stages, and adding increasingly more realistic clouds to 3D simulations will be a useful step toward exploring the effects of their location, height, and opacity on the evolution of a planet's habitability and observational prospects. Beyond that, coupling 3D simulations of the atmosphere with a model of the interior of a planet would for example allow the introduction of volatile cycling between the atmosphere and the interior and time-varying solidification and melting depending on the orbital phase, which would help estimate the ability of the magma ocean to redistribute heat from the dayside to the nightside or even have a thermohaline-like circulation.

Bibliography

Agol, E., Dorn, C., Grimm, S. L., Turbet, M., Ducrot, E., Delrez, L., … others (2021). Refining the transit-timing and photometric analysis of trappist-1: masses, radii, densities, dynamics, and ephemerides. *The planetary science journal*, *2*(1), 1.

Amundsen, D. S., Tremblin, P., Manners, J., Baraffe, I., & Mayne, N. J. (2017). Treatment of overlapping gaseous absorption with the correlated-k method in hot jupiter and brown dwarf atmosphere models. *Astronomy & Astrophysics*, *598*, A97.

Artigau, É., Kouach, D., Donati, J.-F., Doyon, R., Delfosse, X., Baratchart, S., … others (2014). Spirou: the near-infrared spectropolarimeter/high-precision velocimeter for the canada-france-hawaii telescope. In *Ground-based and airborne instrumentation for astronomy v* (Vol. 9147, pp. 423–435).

Batalha, N. E., Mandell, A., Pontoppidan, K., Stevenson, K. B., Lewis, N. K., Kalirai, J., … Nielsen, L. D. (2017). Pandexo: a community tool for transiting exoplanet science with jwst & hst. *Publications of the Astronomical Society of the Pacific*, *129*(976), 064501.

Beichman, C., Barrado, D., Belikov, R., Biller, B., Boccaletti, A., Burrows, A., … others (2019). Direct imaging and spectroscopy of exoplanets with the james webb space telescope. *Bulletin of the American Astronomical Society*, *51*(3), 58.

Bonati, I., Lichtenberg, T., Bower, D. J., Timpe, M. L., & Quanz, S. P. (2019). Direct imaging of molten protoplanets in nearby young stellar associations. *Astronomy & Astrophysics*, *621*, A125.

Boukrouche, R., Hammond, M., & Innes, H. (in prep.). Exofms manual.

Boukrouche, R., Lichtenberg, T., & Pierrehumbert, R. T. (2021). Beyond runaway:

initiation of the post-runaway greenhouse state on rocky exoplanets. *The Astrophysical Journal*, *919*(2), 130.

Bower, D. J., Kitzmann, D., Wolf, A. S., Sanan, P., Dorn, C., & Oza, A. V. (2019). Linking the evolution of terrestrial interiors and an early outgassed atmosphere to astrophysical observations. *Astronomy & Astrophysics*, *631*, A103.

Bower, D. J., Sanan, P., & Wolf, A. S. (2018). Numerical solution of a nonlinear conservation law applicable to the interior dynamics of partially molten planets. *Physics of the earth and planetary interiors*, *274*, 49–62.

Brandeker, A., Alibert, Y., Bourrier, V., Delrez, L., Demory, B.-O., Ehrenreich, D., … others (2021). Is it raining lava in the evening on 55 cancri e? *JWST Proposal. Cycle 1*, 2084.

Burgasser, A. J., & Mamajek, E. E. (2017). On the age of the trappist-1 system. *The Astrophysical Journal*, *845*(2), 110.

Cengel, Y. A., Boles, M. A., & Kanoğlu, M. (2011). *Thermodynamics: an engineering approach* (Vol. 5). McGraw-hill New York.

Chase Jr, M. W. (1998). Nist-janaf themochemical tables, fourth edition. *J. Phys. Chem. Ref. Data, Monograph*, *9*, 1-1951.

Chouqar, J., Benkhaldoun, Z., Jabiri, A., Lustig-Yaeger, J., Soubkiou, A., & Szentgyorgyi, A. (2020). Properties of sub-neptune atmospheres: Toi-270 system. *Monthly Notices of the Royal Astronomical Society*, *495*(1), 962–970.

Cowan, N. B., & Agol, E. (2008). Inverting phase functions to map exoplanets. *The Astrophysical Journal*, *678*(2), L129.

Cox, J., Wagman, D., & Medvedev, V. (1984). Codata key values for thermodynamics. *Hemisphere Publishing Corp., New York*.

Delahaye, T., Armante, R., Scott, N., Jacquinet-Husson, N., Chédin, A., Crépeau, L., … others (2021). The 2020 edition of the geisa spectroscopic database. *Journal of Molecular Spectroscopy*, *380*, 111510.

Ding, F., & Pierrehumbert, R. T. (2016, apr). CONVECTION IN CONDENSIBLE-RICH ATMOSPHERES. *The Astrophysical Journal*, *822*(1), 24. Retrieved from https://doi.org/10.3847/0004-637x/822/1/24 doi: 10.3847/0004-637x/822/1/24

Ding, F., & Pierrehumbert, R. T. (2018, oct). Global or local pure condensible atmospheres: Importance of horizontal latent heat transport. *The Astrophysical Journal*, *867*(1), 54. Retrieved from https://doi.org/10.3847/1538-4357/aae38c doi: 10.3847/1538-4357/aae38c

Ding, F., & Pierrehumbert, R. T. (2020, oct). The phase-curve signature of condensible water-rich atmospheres on slowly rotating tidally locked exoplanets. *The Astrophysical Journal*, *901*(2), L33. Retrieved from https://doi.org/10.3847/2041-8213/abb941 doi: 10.3847/2041-8213/abb941

Dorn, C., & Lichtenberg, T. (2021). Hidden water in magma ocean exoplanets. *The Astrophysical Journal Letters*, *922*(1), L4.

Drummond, B., Mayne, N. J., Manners, J., Baraffe, I., Goyal, J., Tremblin, P., … Kohary, K. (2018). The 3d thermal, dynamical, and chemical structure of the atmosphere of hd 189733b: Implications of wind-driven chemistry for the emission phase curve. *The Astrophysical Journal*, *869*(1), 28.

Ducrot, E., Gillon, M., Delrez, L., Agol, E., Rimmer, P., Turbet, M., … others (2020). Trappist-1: Global results of the spitzer exploration science program red worlds. *Astronomy & Astrophysics*, *640*, A112.

Edwards, J. M., & Slingo, A. (1996, Apr). Studies with a flexible new radiation code. I: Choosing a configuration for a large-scale model. *Q. J. R. Meteorol. Soc.*, *122*(531), 689-719. doi: 10.1002/qj.49712253107

Engineering ToolBox. (2005). Water vapor - specific heat vs. temperature [online]. , Accessed 11 Aug 2022. Retrieved from https://www.engineeringtoolbox.com/water-vapor-d_979.html

Engineering ToolBox. (2018). Water - properties at gas-liquid equilibrium conditions [online]. , Accessed 9 Aug 2022. Retrieved from `https://www.engineeringtoolbox.com/water-properties-temperature-equilibrium-pressure-d_2099.html`

Gillon, M., Triaud, A. H., Demory, B.-O., Jehin, E., Agol, E., Deck, K. M., … others (2017). Seven temperate terrestrial planets around the nearby ultracool dwarf star trappist-1. *Nature*, *542*(7642), 456–460.

Goldblatt, C., Robinson, T. D., Zahnle, K. J., & Crisp, D. (2013). Low simulated radiation limit for runaway greenhouse climates. *Nature Geoscience*, *6*(8), 661–667.

Goody, R., West, R., Chen, L., & Crisp, D. (1989). The correlated-k method for radiation calculations in nonhomogeneous atmospheres. *Journal of Quantitative Spectroscopy and Radiative Transfer*, *42*(6), 539–550.

Gordon, I. E., Rothman, L. S., Hill, C., Kochanov, R. V., Tan, Y., Bernath, P. F., … others (2017). The hitran2016 molecular spectroscopic database. *Journal of Quantitative Spectroscopy and Radiative Transfer*, *203*, 3–69.

Graham, R. J., Lichtenberg, T., Boukrouche, R., & Pierrehumbert, R. T. (2021, oct). A multispecies pseudoadiabat for simulating condensable-rich exoplanet atmospheres. *The Planetary Science Journal*, *2*(5), 207. Retrieved from `https://doi.org/10.3847/psj/ac214c` doi: 10.3847/psj/ac214c

Greene, T. P., Lagage, P.-O., Rieke, M. J., & Schlawin, E. (2017). Miri observations of transiting exoplanets. *JWST Proposal. Cycle 1*, 1177.

Grimm, S. L., & Heng, K. (2015). Helios-k: An ultrafast, open-source opacity calculator for radiative transfer. *The Astrophysical Journal*, *808*(2), 182.

Hamano, K., Abe, Y., & Genda, H. (2013). Emergence of two types of terrestrial planet on solidification of magma ocean. *Nature*, *497*(7451), 607–610.

Hamano, K., Kawahara, H., Abe, Y., Onishi, M., & Hashimoto, G. L. (2015). Lifetime and spectral evolution of a magma ocean with a steam atmosphere: its detectability by future direct imaging. *The Astrophysical Journal*, *806*(2), 216.

Ingersoll, A. P. (1969). The runaway greenhouse a history of water on venus. , *26*.

Jontof-Hutter, D. (2019). The compositional diversity of low-mass exoplanets. *Annual Review of Earth and Planetary Sciences*, *47*, 141–171.

Kasting, J. F. (1988). Runaway and moist greenhouse atmospheres and the evolution of earth and venus. *Icarus*, *74*(3), 472–494.

Kasting, J. F. (1991). Co2 condensation and the climate of early mars. *Icarus*, *94*(1), 1-13. Retrieved from `https://www.sciencedirect.com/science/article/pii/001910359190137I` doi: https://doi.org/10.1016/0019-1035(91)90137-I

Kasting, J. F., Whitmire, D. P., & Reynolds, R. T. (1993). Habitable zones around main sequence stars. *Icarus*, *101*(1), 108–128.

Katyal, N., Ortenzi, G., Grenfell, J. L., Noack, L., Sohl, F., Godolt, M., . . . Rauer, H. (2020). Effect of mantle oxidation state and escape upon the evolution of earths magma ocean atmosphere. *Astronomy & Astrophysics*, *643*, A81.

Katz, R. F., Spiegelman, M., & Langmuir, C. H. (2003). A new parameterization of hydrous mantle melting. *Geochemistry, Geophysics, Geosystems*, *4*(9).

Kendrew, S., Scheithauer, S., Bouchet, P., Amiaux, J., Azzollini, R., Bouwman, J., . . . others (2015). The mid-infrared instrument for the james webb space telescope, iv: The low-resolution spectrometer. *Publications of the Astronomical Society of the Pacific*, *127*(953), 623.

Kitzmann, D., Heng, K., Oreshenko, M., Grimm, S. L., Apai, D., Bowler, B. P., . . . Marley, M. S. (2020). Helios-r2: a new bayesian, open-source retrieval model for brown dwarfs and exoplanet atmospheres. *The Astrophysical Journal*, *890*(2), 174.

Kopparapu, R. K., Ramirez, R., Kasting, J. F., Eymet, V., Robinson, T. D., Mahadevan, S., … Deshpande, R. (2013). Habitable zones around main-sequence stars: new estimates. *The Astrophysical Journal*, *765*(2), 131.

Kreidberg, L., Hu, R., Kite, E. S., Koll, D., Malik, M., Morley, C., … Whittaker, E. (2021). A search for signatures of volcanism and geodynamics on the hot rocky exoplanet lhs 3844b. *JWST Proposal. Cycle 1*, 1846.

Lean, J. L., & DeLand, M. T. (2012). How does the suns spectrum vary? *Journal of Climate*, *25*(7), 2555–2560.

Leconte, J., Forget, F., Charnay, B., Wordsworth, R., & Pottier, A. (2013). Increased insolation threshold for runaway greenhouse processes on earth-like planets. *Nature*, *504*(7479), 268–271.

Leconte, J., Selsis, F., Hersant, F., & Guillot, T. (2017). Condensation-inhibited convection in hydrogen-rich atmospheres-stability against double-diffusive processes and thermal profiles for jupiter, saturn, uranus, and neptune. *Astronomy & Astrophysics*, *598*, A98.

Lee, E. K., Parmentier, V., Hammond, M., Grimm, S. L., Kitzmann, D., Tan, X., … Pierrehumbert, R. T. (2021). Simulating gas giant exoplanet atmospheres with exo-fms: comparing semigrey, picket fence, and correlated-k radiative-transfer schemes. *Monthly Notices of the Royal Astronomical Society*, *506*(2), 2695–2711.

Li, C., Ingersoll, A. P., & Oyafuso, F. (2018, April). Moist Adiabats with Multiple Condensing Species: A New Theory with Application to Giant-Planet Atmospheres. *Journal of Atmospheric Sciences*, *75*(4), 1063-1072. doi: 10.1175/JAS-D-17-0257.1

Lichtenberg, T., Bower, D. J., Hammond, M., Boukrouche, R., Sanan, P., Tsai, S.-M., & Pierrehumbert, R. T. (2021). Vertically resolved magma ocean–

protoatmosphere evolution: H2, h2o, co2, ch4, co, o2, and n2 as primary absorbers. *Journal of Geophysical Research: Planets*, *126*(2), e2020JE006711.

Lichtenberg, T., Schaefer, L. K., Nakajima, M., & Fischer, R. A. (2022). Geophysical evolution during rocky planet formation. *arXiv preprint arXiv:2203.10023*.

Lincowski, A. P., Meadows, V. S., Crisp, D., Robinson, T. D., Luger, R., Lustig-Yaeger, J., & Arney, G. N. (2018). Evolved climates and observational discriminants for the trappist-1 planetary system. *The Astrophysical Journal*, *867*(1), 76.

Luger, R., & Barnes, R. (2015). Extreme water loss and abiotic o2 buildup on planets throughout the habitable zones of m dwarfs. *Astrobiology*, *15*(2), 119–143.

Lupu, R., Zahnle, K., Marley, M. S., Schaefer, L., Fegley, B., Morley, C., … Fortney, J. J. (2014). The atmospheres of earthlike planets after giant impact events. *The Astrophysical Journal*, *784*(1), 27.

Lustig-Yaeger, J., Meadows, V. S., & Lincowski, A. P. (2019). The detectability and characterization of the trappist-1 exoplanet atmospheres with jwst. *The Astronomical Journal*, *158*(1), 27.

Marcq, E., Salvador, A., Massol, H., & Davaille, A. (2017). Thermal radiation of magma ocean planets using a 1-d radiative-convective model of h2o-co2 atmospheres. *Journal of Geophysical Research: Planets*, *122*(7), 1539–1553.

Morley, C. V., Kreidberg, L., Rustamkulov, Z., Robinson, T., & Fortney, J. J. (2017). Observing the atmospheres of known temperate earth-sized planets with jwst. *The Astrophysical Journal*, *850*(2), 121.

Nakajima, S., Hayashi, Y.-Y., & Abe, Y. (1992). A study on the runaway greenhouse effect with a one-dimensional radiative–convective equilibrium model. *Journal of Atmospheric Sciences*, *49*(23), 2256–2266.

Olson, G. L., & Kunasz, P. (1987). Short characteristic solution of the non-lte line transfer problem by operator perturbationi. the one-dimensional planar slab. *Journal of Quantitative Spectroscopy and Radiative Transfer*, *38*(5), 325–336.

Parmentier, V., & Guillot, T. (2014). A non-grey analytical model for irradiated atmospheres-i. derivation. *Astronomy & Astrophysics*, *562*, A133.

Pepe, F., Molaro, P., Cristiani, S., Rebolo, R., Santos, N., Dekker, H., … others (2014). *Espresso: The next european exoplanet hunter* (Vol. 335) (No. 1). Wiley Online Library.

Pierrehumbert, R. T. (2010). *Principles of Planetary Climate, Cambridge University Press.*

Pierrehumbert, R. T., & Ding, F. (2016). Dynamics of atmospheres with a non-dilute condensible component. , *472*(2190). doi: 10.1098/rspa.2016.0107

Pierrehumbert, R. T., & Hammond, M. (2019). Atmospheric circulation of tide-locked exoplanets. *Annual Review of Fluid Mechanics*, *51*, 275–303.

Plato. (360 B.C.E.) *Oxford Classical Texts: Platonis Opera, Vol. 1: Tetralogiae I-II (1995).* Oxford University Press; Oxford Classical Texts. (Edited by E. A. Duke, W. F, Hicken, W. S. M. Nicoll, D. B. Robinson, and J. C. G. Strachan) doi: 10.1093/actrade/9780198145691.book.1

Ptashnik, I. V., McPheat, R. A., Shine, K. P., Smith, K. M., & Williams, R. G. (2011). Water vapor self-continuum absorption in near-infrared windows derived from laboratory measurements. *Journal of Geophysical Research: Atmospheres*, *116*(D16).

Quanz, S. P., Absil, O., Benz, W., Bonfils, X., Berger, J.-P., Defrère, D., … others (2021b). Atmospheric characterization of terrestrial exoplanets in the mid-infrared: biosignatures, habitability, and diversity. *Experimental Astronomy*, 1–25.

Quanz, S. P., Ottiger, M., Fontanet, E., Kammerer, J., Menti, F., Dannert, F., … others (2021a). Large interferometer for exoplanets (life): I. improved exoplanet detection yield estimates for a large mid-infrared space-interferometer mission. *arXiv preprint arXiv:2101.07500*.

Ramirez, R. M., Kopparapu, R. K., Lindner, V., & Kasting, J. F. (2014). Can increased atmospheric co2 levels trigger a runaway greenhouse? *Astrobiology*, *14*(8), 714–731.

Ramsay, S., Amico, P., Bezawada, N., Cirasuolo, M., Derie, F., Egner, S., … others (2020). The eso extremely large telescope instrumentation programme. In *Advances in optical astronomical instrumentation 2019* (Vol. 11203, p. 1120303).

Rathcke, A., Bello-Arufe, A., Buchhave, L. A., Burgasser, A. J., Diamond-Lowe, H., Espinoza, N., … others (2021). Probing the terrestrial planet trappist-1c for the presence of an atmosphere. *JWST Proposal. Cycle 1*, 2420.

Rauer, H., Catala, C., Aerts, C., Appourchaux, T., Benz, W., Brandeker, A., … others (2014). The plato 2.0 mission. *Experimental Astronomy*, *38*(1), 249–330.

Rieke, G., Ressler, M., Morrison, J. E., Bergeron, L., Bouchet, P., García-Marín, M., … Walker, H. (2015). The mid-infrared instrument for the james webb space telescope, vii: The miri detectors. *Publications of the Astronomical Society of the Pacific*, *127*(953), 665.

Schaefer, L., Wordsworth, R. D., Berta-Thompson, Z., & Sasselov, D. (2016). Predictions of the atmospheric composition of gj 1132b. *The Astrophysical Journal*, *829*(2), 63.

Serdyuchenko, A., Gorshelev, V., Weber, M., Chehade, W., & Burrows, J. (2014). High spectral resolution ozone absorption cross-sections–part 2: Temperature dependence. *Atmospheric Measurement Techniques*, *7*(2), 625–636.

Simpson, S. G. C. (1927). Some studies in terrestrial radiation. *Memoirs of the*

Royal Meteorological Society, *2*(16), 69-95.

Team, L., et al. (2019). The luvoir mission concept study final report. *arXiv preprint arXiv:1912.06219*.

Tennyson, J., & Yurchenko, S. N. (2017). Laboratory spectra of hot molecules: Data needs for hot super-earth exoplanets. *Molecular Astrophysics*, *8*, 1–18.

Tennyson, J., Yurchenko, S. N., Al-Refaie, A. F., Clark, V. H., Chubb, K. L., Conway, E. K., … others (2020). The 2020 release of the exomol database: molecular line lists for exoplanet and other hot atmospheres. *Journal of Quantitative Spectroscopy and Radiative Transfer*, *255*, 107228.

Thomas, G. E., & Stamnes, K. (2002). *Radiative Transfer in the Atmosphere and Ocean*.

Tinetti, G., Drossart, P., Eccleston, P., Hartogh, P., Heske, A., Leconte, J., … others (2018). A chemical survey of exoplanets with ariel. *Experimental Astronomy*, *46*(1), 135–209.

Toon, O. B., McKay, C. P., Ackerman, T. P., & Santhanam, K. (1989). Rapid calculation of radiative heating rates and photodissociation rates in inhomogeneous multiple scattering atmospheres. *Journal of Geophysical Research: Atmospheres*, *94*(D13), 16287-16301. Retrieved from `https://agupubs.onlinelibrary.wiley.com/doi/abs/10.1029/JD094iD13p16287` doi: https://doi.org/10.1029/JD094iD13p16287

Turbet, M., Bolmont, E., Chaverot, G., Ehrenreich, D., Leconte, J., & Marcq, E. (2021). Day–night cloud asymmetry prevents early oceans on venus but not on earth. *Nature*, *598*(7880), 276–280.

Turbet, M., Ehrenreich, D., Lovis, C., Bolmont, E., & Fauchez, T. (2019). The runaway greenhouse radius inflation effect.
doi: 10.1051/0004-6361/201935585

Vallis, G. K. (2017). *Atmospheric and oceanic fluid dynamics*. Cambridge University Press.

Way, M. J., & Del Genio, A. D. (2020, May). Venusian Habitable Climate Scenarios: Modeling Venus Through Time and Applications to Slowly Rotating Venus-Like Exoplanets. *J. Geophys. Res. Planets*, *125*(5), e06276. doi: 10.1029/2019JE006276

Wordsworth, R., & Pierrehumbert, R. (2013). Water loss from terrestrial planets with co2-rich atmospheres. *The Astrophysical Journal*, *778*(2), 154.

Yang, J., & Abbot, D. S. (2014). A low-order model of water vapor, clouds, and thermal emission for tidally locked terrestrial planets. *The Astrophysical Journal*, *784*(2), 155.

Youngblood, A., France, K., Loyd, R. P., Brown, A., Mason, J. P., Schneider, P. C., … others (2017). The muscles treasury survey. iv. scaling relations for ultraviolet, ca ii k, and energetic particle fluxes from m dwarfs. *The Astrophysical Journal*, *843*(1), 31.

A | 1 bar surface pressure

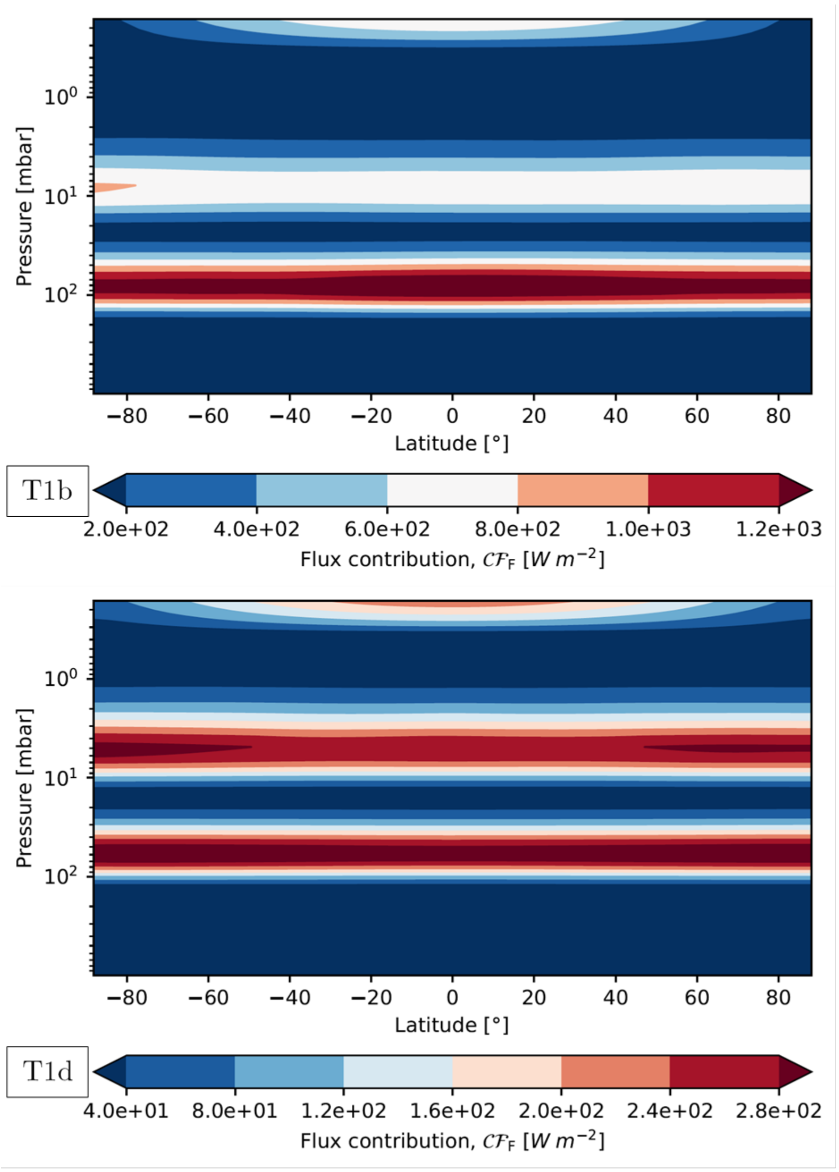

Figure A.1: Zonal mean contribution function $p_s = 1$ bar.

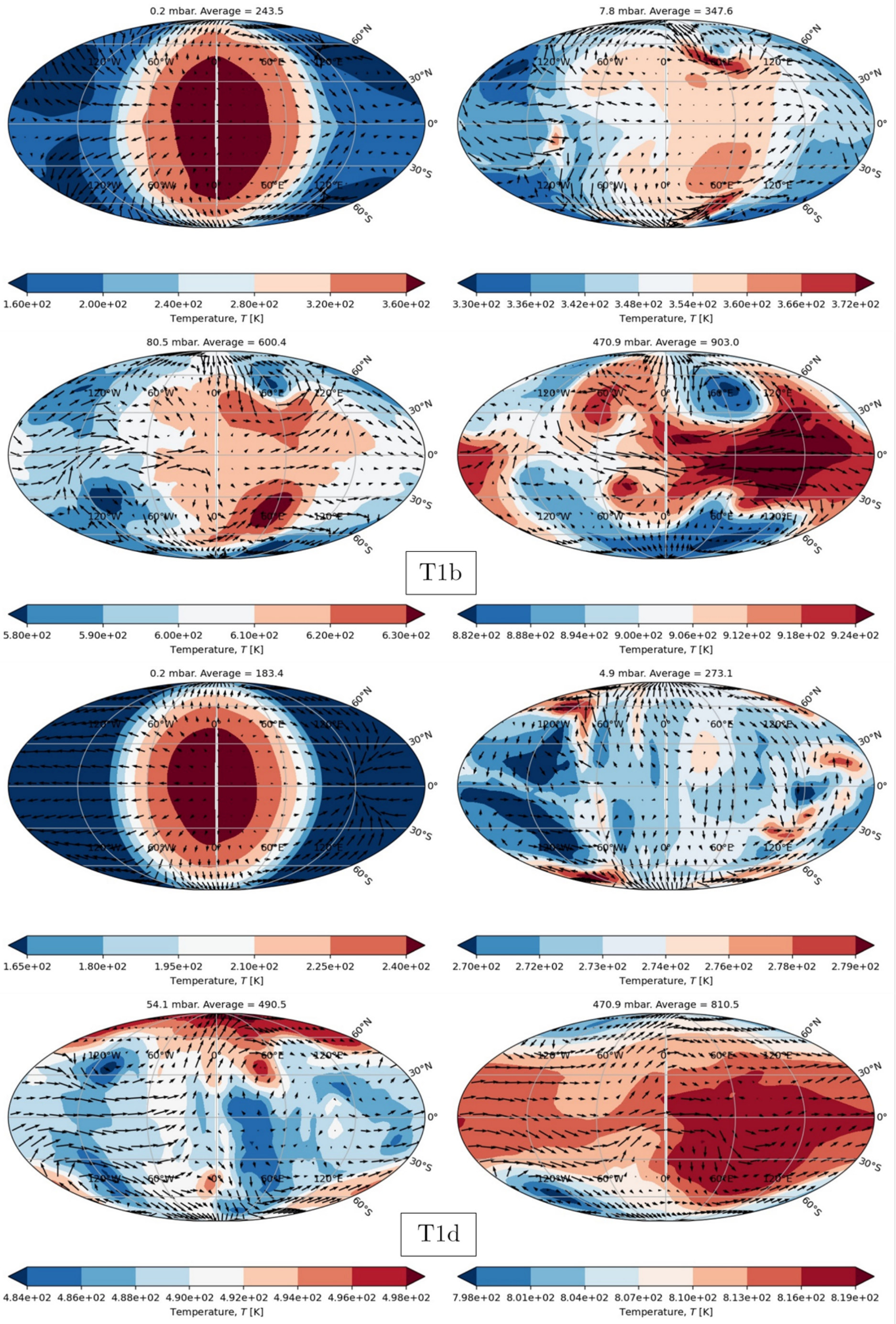

Figure A.2: Global temperature maps at four selected altitudes. $p_s = 1$ bar.

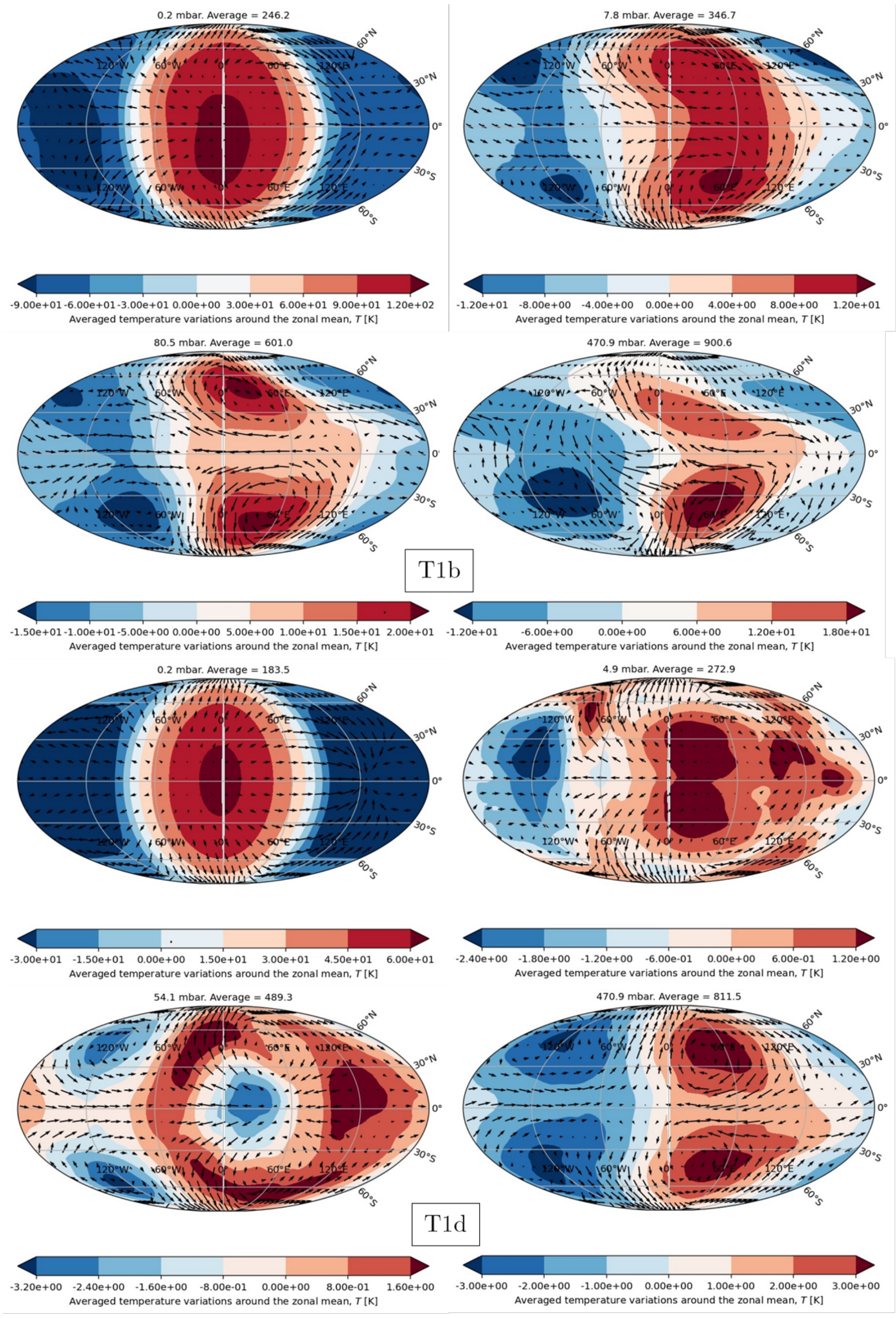

Figure A.3: Deviation from the zonal mean. $p_s = 1$ bar.

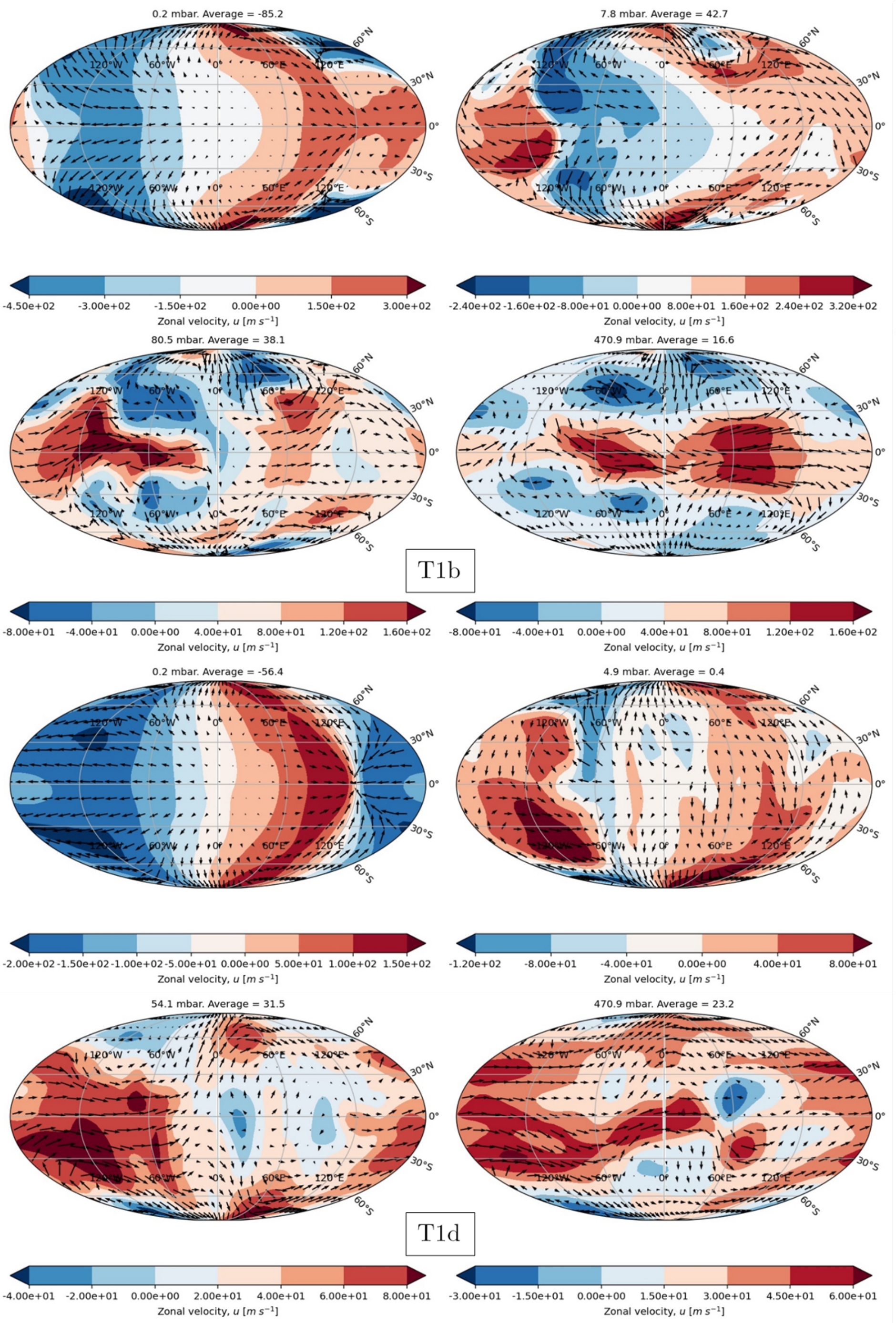

Figure A.4: Zonal wind maps at four selected altitudes. $\mathrm{p_s} = 1$ bar.

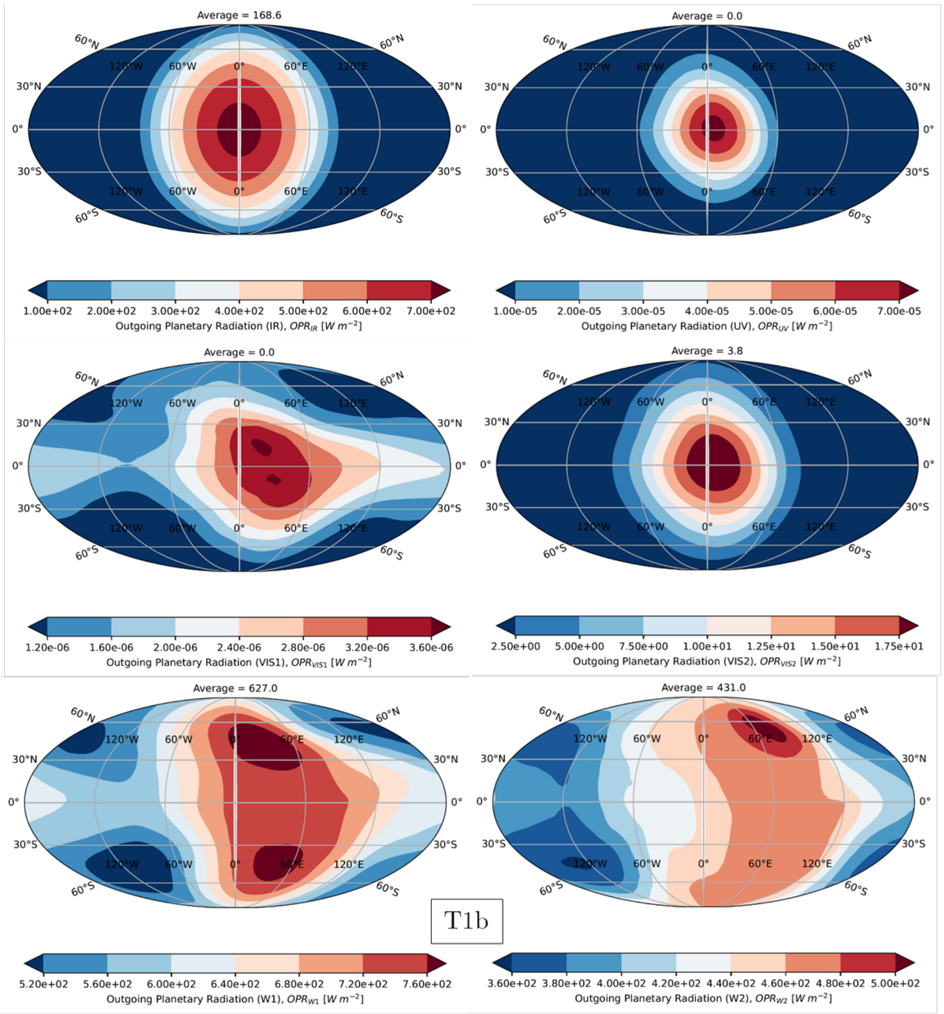

Figure A.5: Global bandwise OPR map for TRAPPIST-1b. $p_s = 1$ bar.

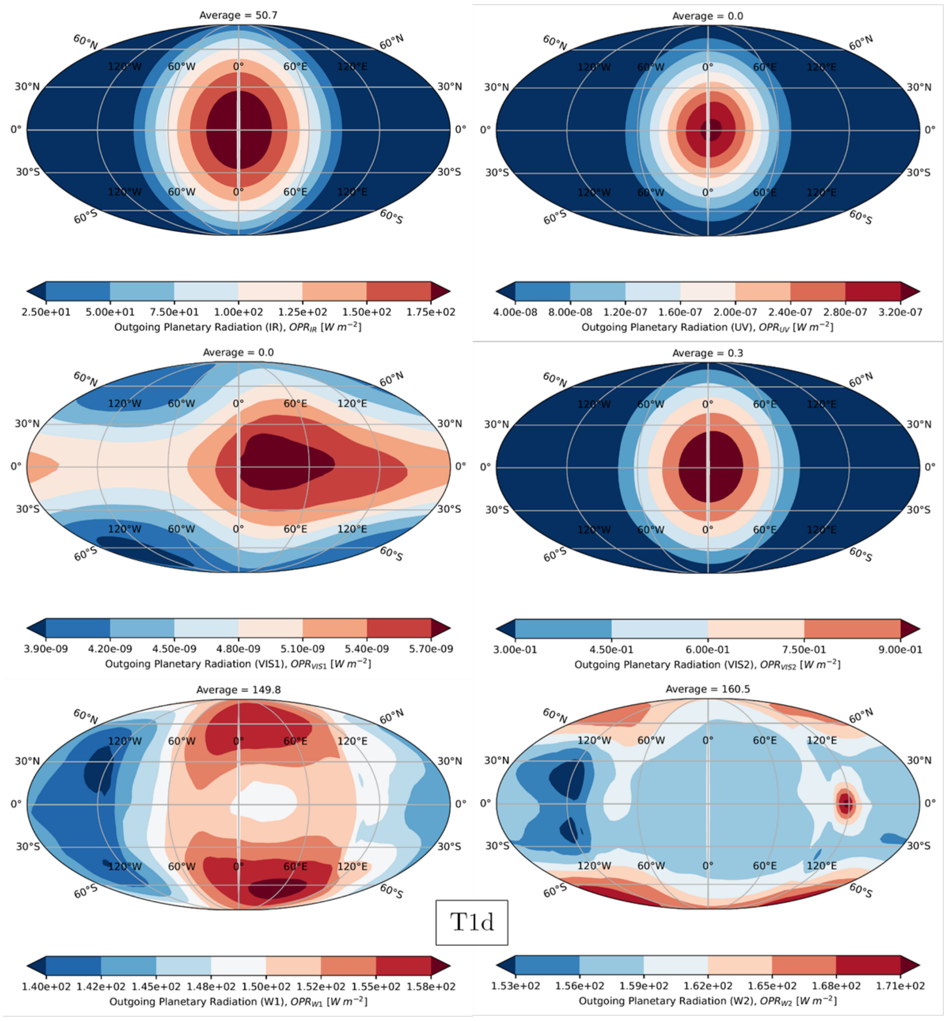

Figure A.6: Global bandwise OPR map for TRAPPIST-1d. $p_s = 1$ bar.

B | 260 bar surface pressure

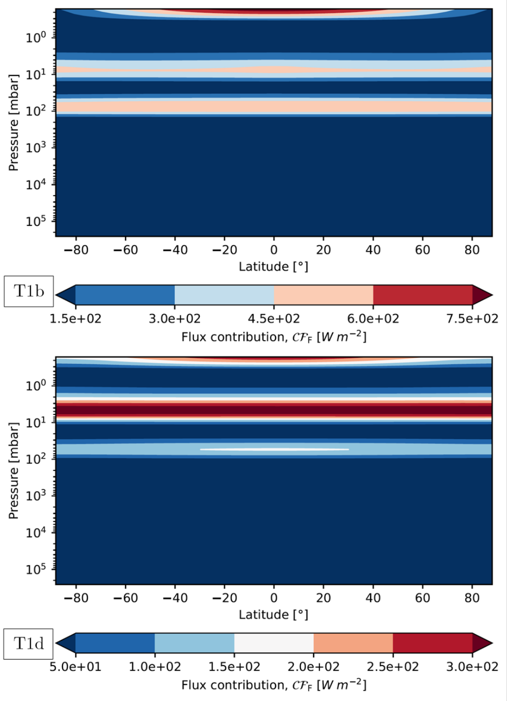

Figure B.1: Zonal mean contribution function $p_s = 260$ bar.

Figure B.1 shows a contribution to the outgoing radiation peaking at the same pressure levels as in previous cases, though the peaks are even higher up in height coordinates given the mass added to the bottom of the atmosphere. The graph also indicates that, as in the 1-bar case, there is no peak lower than the ones corresponding to the water vapour windows around 8 and 80 mbar on TRAPPIST-1b and around 4.5 and 55 mbar for TRAPPIST-1d.

The first panels of Figures B.2-T1b and T1d at 0.2 mbar show a slight hot spot shift, eastward for TRAPPIST-1b and westward for TRAPPIST-1d, like before. TRAPPIST-1b only shows low amplitude Rossby waves from the deviation from the zonal mean plots, around 35282 and 102098 mbar. None are present in the atmosphere of TRAPPIST-1d except a low amplitude one at 251386 mbar.

Figure B.4 shows the zonal wind contours and quiver field at the same pressure levels as above. Figure B.5 confirms the 1D profiles seen on Figure 8.28, suggesting that on both planets, all pressure levels are warmer than the dew point of water vapour, resulting in a cloud-free atmosphere.

Figure B.6 shows a substellar OPR of 1300 $\mathrm{W\,m^{-2}}$ on TRAPPIST-1b and 440

$\mathrm{W\,m^{-2}}$ on TRAPPIST-1d. No clear hot spot shift can be seen except for a westward equatorial extension on the inner planet, which is due to the atmospheric windows, as seen on Figures B.7 and B.8. The IR contribution to the outgoing planetary radiation is near-symmetrical on both planets, centred on the substellar point. The UV and visible fluxes are weak given the temperatures reached in the lower layers. The radiation in the window W2 seems to come from around 3 mbar, whereas W1 seems to be radiating from both the 8 mbar and the 80 mbar peaks of the contribution function. Observing the W2 band would show an eastward hot spot shift. The 5-mbar CFF peak on TRAPPIST-1d comes from outgoing radiation in the W2 band, whereas the 60-mbar one comes from the W1 band.

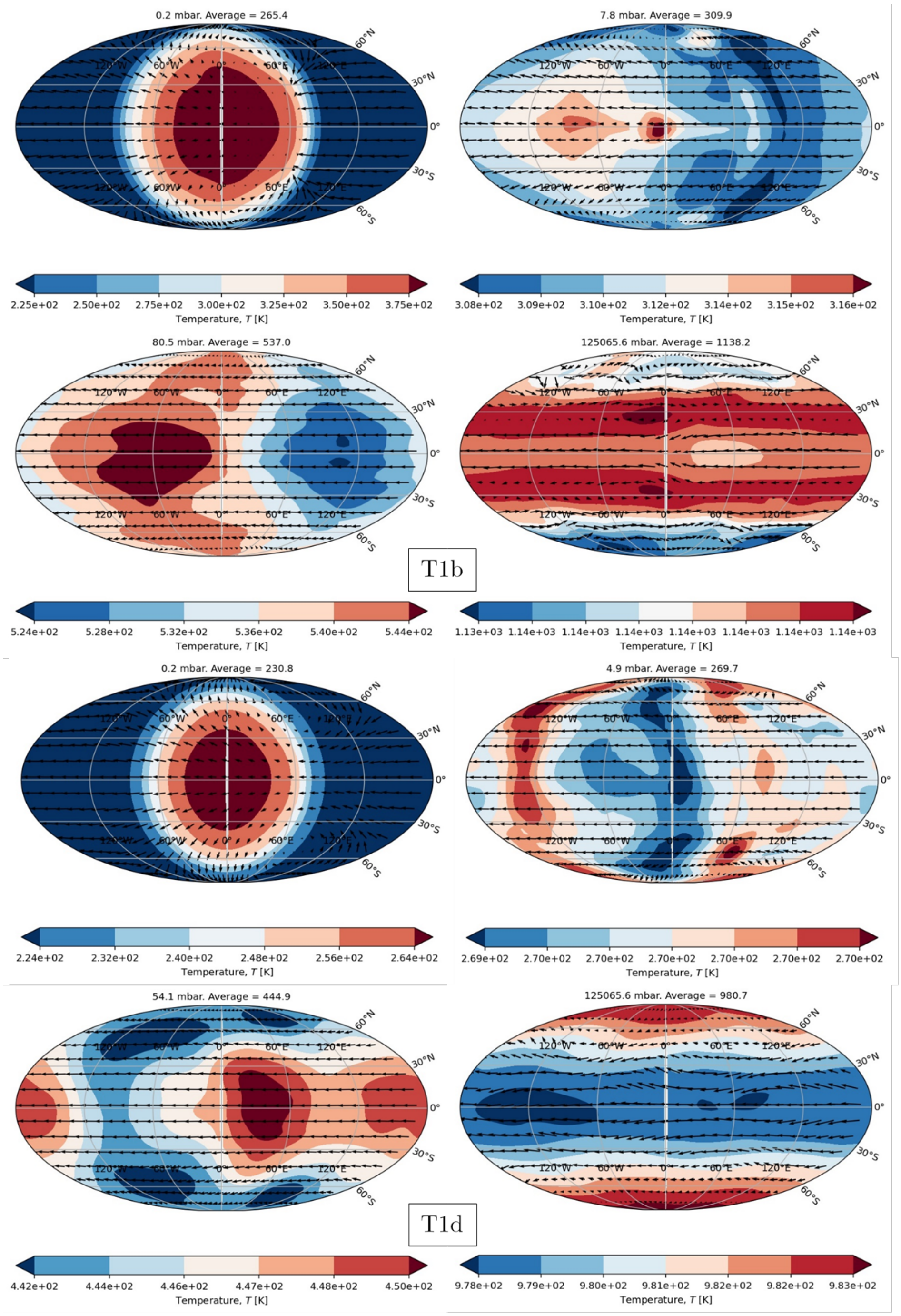

Figure B.2: Global temperature maps at four selected altitudes $p_s = 260$ bar.

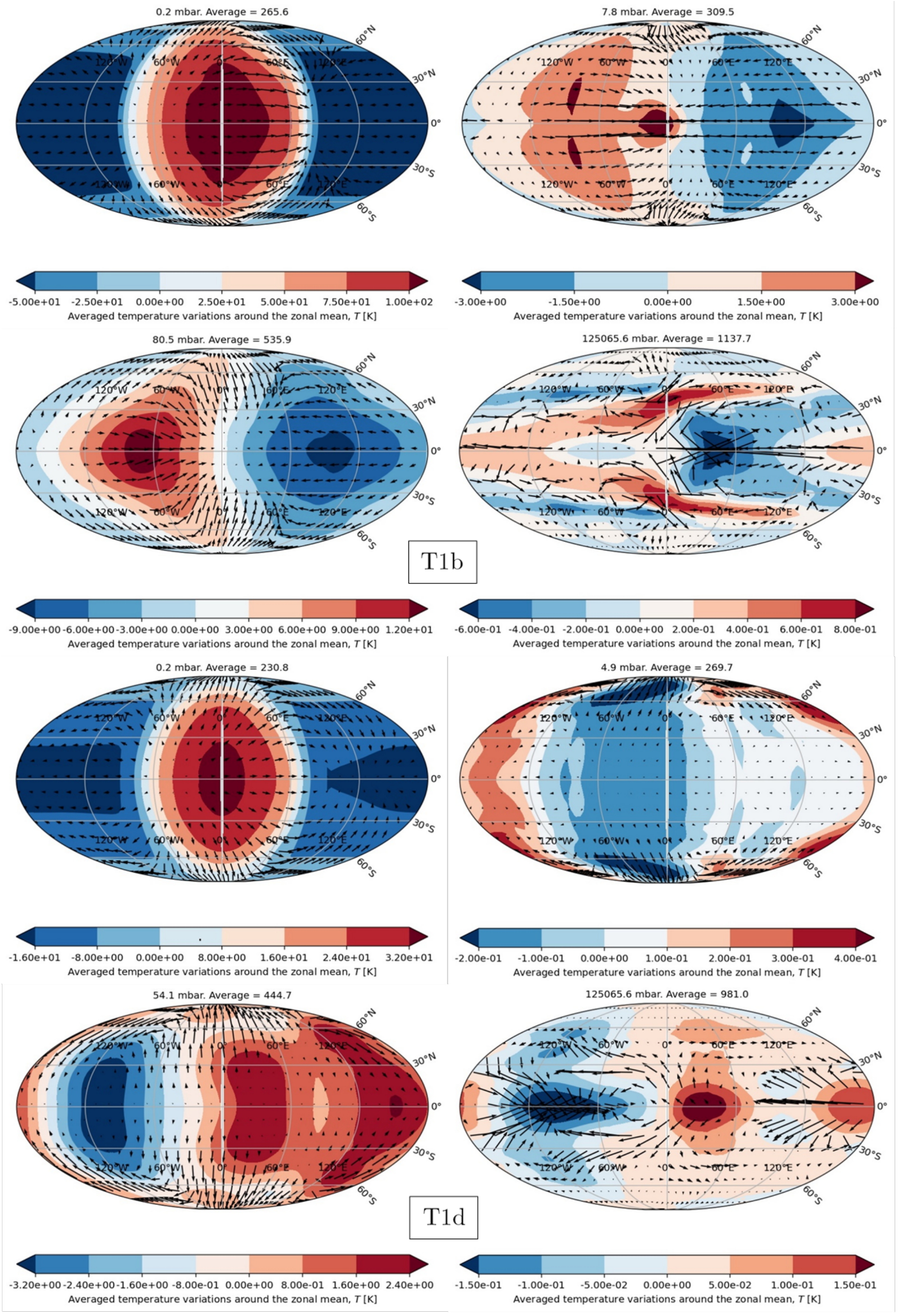

Figure B.3: Deviation from the zonal mean. $p_s = 260$ bar.

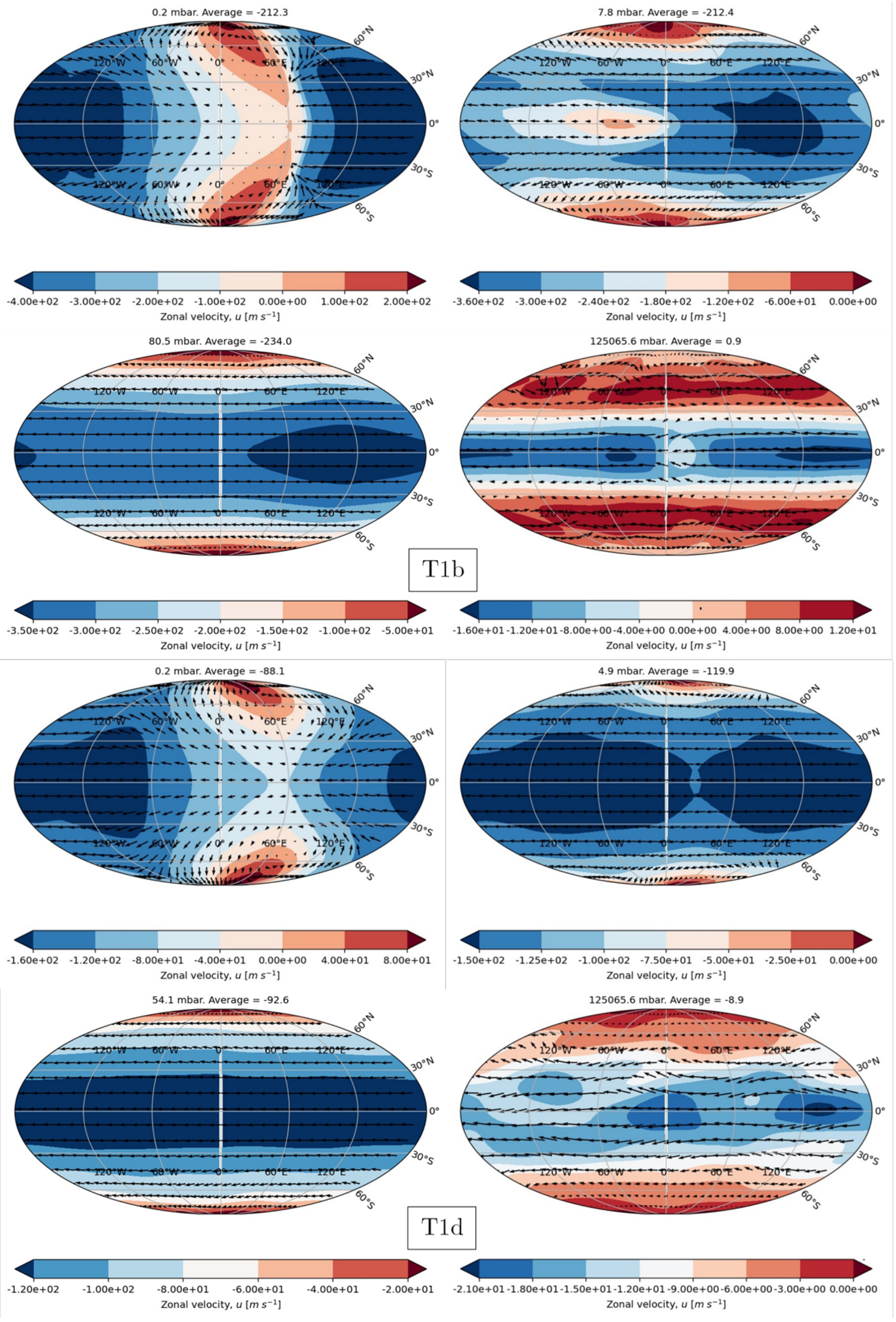

Figure B.4: Zonal wind maps at four selected altitudes. $p_s = 260$ bar.

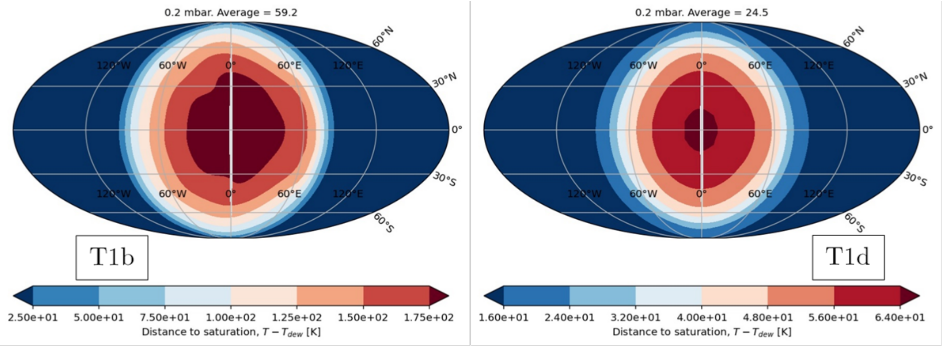

Figure B.5: Global saturation maps at the TOA. $\mathrm{p_s} = 260$ bar.

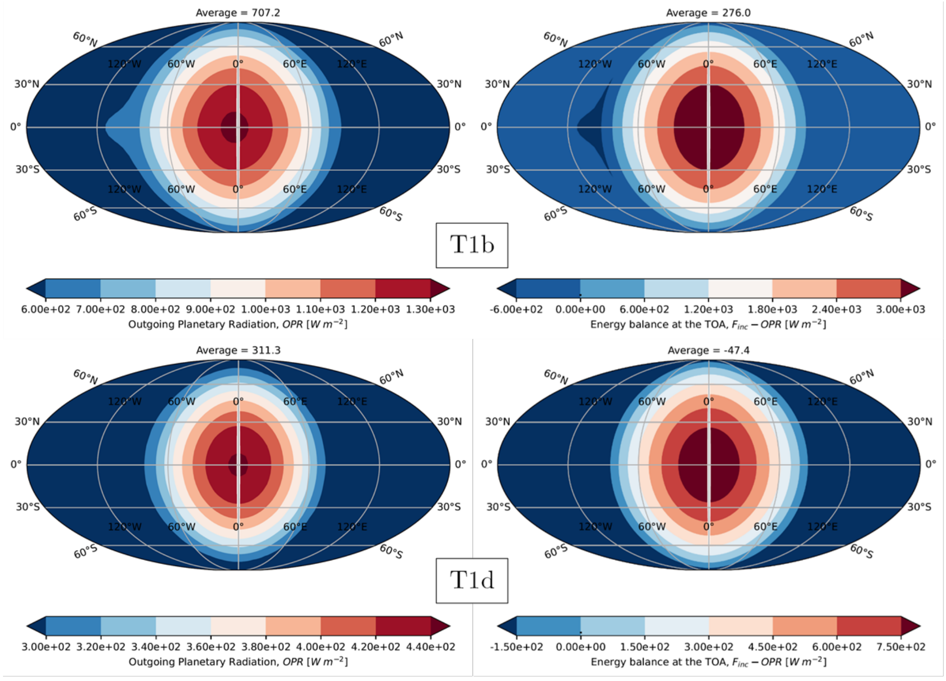

Figure B.6: Global bolometric TOA budget map. $\mathrm{p_s} = 260$ bar.

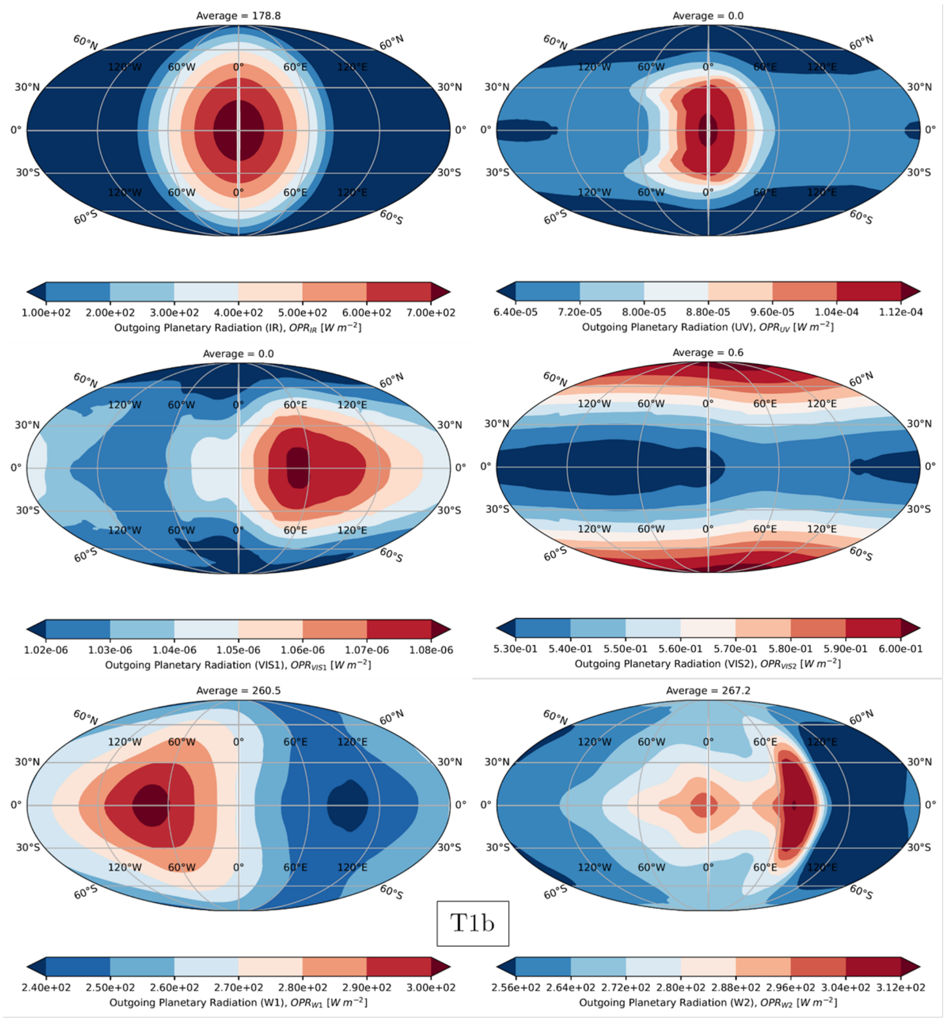

Figure B.7: Global bandwise OPR maps for TRAPPIST-1b. $p_s = 260$ bar.

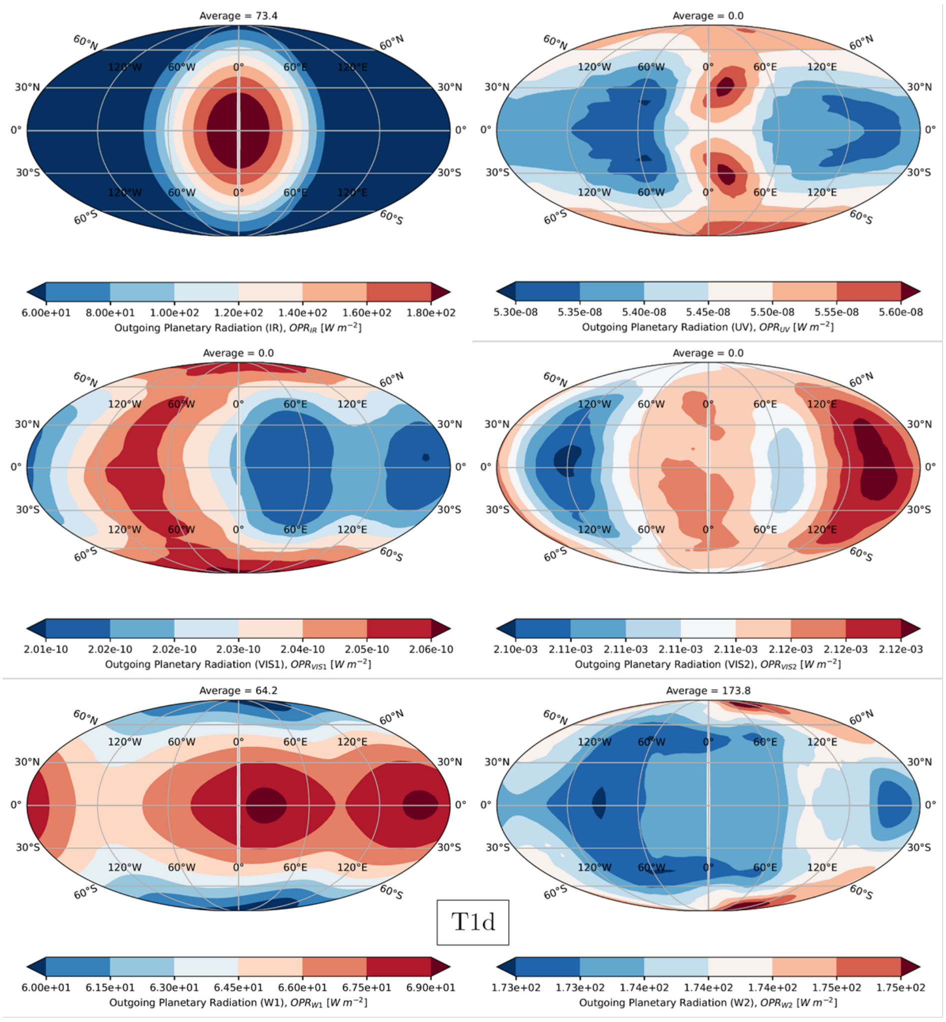

Figure B.8: Global bandwise OPR maps for TRAPPIST-1d. $\mathrm{p_s} = 260$ bar.